Study of photon-associated Higgs production at the ILC and R&D for the ILD-TPC

AOKI Yumi

The Graduate University for Advanced Studies, SOKENDAI

Ph.D thesis submitted to Department of Particle and Nuclear Physics, The Graduate University for Advanced Studies, SOKENDAI

December 10, 2021

Contents

Abstract

The standard model (SM) has been successfully described measurements at past and current collider experiments. There are, however, phenomena that cannot be explained by the SM. The Higgs boson is a powerful discovery tool for physics beyond the standard model (BSM) of particle physics because any deviation patterns of the Higgs couplings to SM particles from SM predictions tells us the nature of the BSM physics. The International Linear Collider (ILC), a linear electron-positron collider, is an ideal machine to precisely measure the absolutely normalised Higgs couplings, thanks to the recoil mass technique usable only at lepton colliders. In order to precisely measure the Higgs couplings at 250 GeV ILC, we need to use the SM effective field theory (SMEFT).

It is desirable in SMEFT-based Higgs coupling analysis to improve the precision of the $h\gamma Z$ coupling. In part 1 of this thesis, we present a world-first full simulation study of the $e^+e^- \to h\gamma$ process using a realistic model of the International Large Detector (ILD) to study the feasibility to constrain the SMEFT $h\gamma Z$ coefficient, ζ_{AZ}, at the ILC.

The full simulation study showed that if there is no BSM contribution the $e^+e^- \to h\gamma$ process is much more difficult to observe than naively expected. We thus put upper limits on the cross section of this process. The expected combined 95% C.L. upper limits for full polarisations: $(P_{e^-}, P_{e^+}) = (-100\%, +100\%)$ and $(+100\%, -100\%)$ are $\frac{\sigma^L_{h\gamma}}{\sigma^L_{SM}} < 5.0$ and $\frac{\sigma^R_{h\gamma}}{\sigma^R_{SM}} < 61.9$, respectively. The corresponding 95% C.L. limit on ζ_{AZ} is $-0.020 < \zeta_{AZ} < 0.003$.

A charged particle tracker with high momentum resolution is essential for precision Higgs measurements, particularly the cross section measurement using the recoil mass technique. The main tracker of the ILD is a Time Projection Chamber (TPC). We describe R&D of the ILD-TPC in the second part of this thesis. Precision momentum measurement requires good spatial resolution in both $r\phi$ (transverse) and z (longitudinal) directions. To achieve the spatial resolution goals, it is essential to prevent positive ions generated by gas amplification in the ILD-TPC's end-plane readout modules from flowing back into its drift volume. To block these positive ions, we have developed a gating device with an optical aperture of 80% in collaboration with FUJIKURA company.

We carried out the world-first beam test of a prototype end-plane readout module with this gating device and evaluated its performance in terms of spatial resolution. We found that the spatial resolution requirements, better than 100 μm in the $r\phi$ and 0.4-1.4 mm in z directions, are achievable with magnetic field of 3.5 T over the full drift length of 2.2 m with our gating device. In the course of this study, we tried various methods of coordinate estimation and calibrations, details of which are also described.

1 Overview

This thesis consists of two parts. The first part deals with the simulation study of the $e^+e^- \to h\gamma$ process at the International Linear Collider (ILC), while the second part treats the R&D of a Time Projection Chamber (TPC) for the ILC experiment. Both parts are important for the Higgs coupling measurement.

Part 1 The precise measurement of the Higgs boson is a powerful tool for discovering physics beyond the Standard Model (SM). The ILC is an ideal machine to perform the precise measurement of the Higgs boson, taking advantage of its clean environment, well-defined initial state, and powerful beam polarisation. The primary motivation of this study is clarifying the potential to probe new physics via $h\gamma\gamma$ and $h\gamma Z$ couplings using the $e^+e^- \to h\gamma$ process at the ILC. In the SM, these couplings are only loop-induced, thus may receive relatively large modifications from Beyond the SM (BSM) contributions, thereby suggesting potentially high sensitivity to BSM physics [1].

In this study, we perform simulation of this process using the full detector simulation framework based on Geant4 [2] of the International Large Detector (ILD). We will then estimate the expected upper limit of the cross section of the $e^+e^- \to h\gamma$ process at the ILC. The upper limit will be interpreted using model-independent Effective Field Theory (EFT) coefficients, and the electron Yukawa coupling.

Part 2 In order to use the recoil mass technique to obtain Higgs couplings, the Time Projection Chamber (TPC) for the ILD is required to provide a momentum resolution of $\frac{\sigma_{P_T}}{P_T^2} = 1 \times 10^{-4}$ GeV$^{-1} \cdot$ c. The key to achieve this requirement is the spatial resolution of measurement points along the trajectory. This spatial resolution required to achieve the momentum resolution is better than 100 μm in the $r\phi$ direction and 0.4-1.4 mm in the z direction (over zero to full drift length). An obstacle to achieve this performance has been the ion back-flow problem, in which ions generated by ionisation in the amplification region flow back into the drift region and distort the electric field, causing a deterioration of the spatial resolution. To solve this problem, we have developed a gating device in collaboration with the FUJIKURA company. We are now verifying that an end-plane readout module equipped with this gating device can achieve the required performance.

For the spatial resolution in the $r\phi$ direction, there is an analytic formula that can describe beam test results without the gating device at all drift lengths [3]. The formula clarified the parameters such as the effective number of seed electrons N_{eff}, the transverse diffusion constant C_{dT}, the width of the pad response function σ_{PRF}, and the pad pitch w. It also allowed us to extrapolate the prototype results to the full-size ILD-TPC. We report the result of a performance evaluation of the end-plane readout module equipped with the gating device. This is the world first beam test result with a gating device. We discuss the validity of the analytic formula for $r\phi$ resolution and the extrapolation of the $r\phi$ and z resolution result to the real-size ILD-TPC.

We also analyse the beam test data to characterise the behaviour of the z resolution. In the course of the analysis, we tried various methods to estimate the z coordinate using signal pulses recorded by the readout module. To understand the result, we developed a simulator to reproduce the beam test result. Comparing the simulation and the beam test result, we discuss potential missing or inappropriately implemented factors to fill the gap between the simulation result and the teat beam result at short drift length.

2 Introduction

2.1 Physics

Previous studies at colliders such as TRISTAN, LEP, SLC, Tevatron, and LHC have established the Standard Model (SM), which is a theory of electroweak and strong interactions based on the $SU(3)_c \times SU(2)_L \times U(1)_Y$ gauge symmetry. The SM Lagrangian can be expressed as follows

$$\begin{aligned}
\mathcal{L}_{\mathrm{SM}} = & -\frac{1}{4}G_{\mu\nu}G^{\mu\nu} - \frac{1}{4}W_{\mu\nu}W^{\mu\nu} - \frac{1}{4}B_{\mu\nu}B^{\mu\nu} \\
& + \bar{Q}i\gamma^{\mu}D_{\mu}Q + \bar{L}i\gamma^{\mu}D_{\mu}L \\
& + \overline{u_R}i\gamma^{\mu}D_{\mu}u_R + \overline{d_R}i\gamma^{\mu}D_{\mu}d_R + e_R i\gamma^{\mu}D_{\mu}e_R \\
& + \left(D^{\mu}\Phi\right)^{\dagger}\left(D_{\mu}\Phi\right) - \lambda\left(\Phi^{\dagger}\Phi - \frac{1}{2}v^2\right)^2 \\
& + \left\{+Y_u\bar{Q}\tilde{\Phi}u_R + Y_d\bar{Q}\Phi d_R + Y_e\bar{L}\Phi e_R + \text{ h.c. }\right\}.
\end{aligned} \tag{1}$$

This equation represents a picture in which the universe as we know it consists of three types of particles: matter particles (matter fermions), force particles (gauge bosons), and the Higgs boson as shown in Figure 1.

Although gauge symmetry does not allow gauge bosons' mass at the Lagrangian level, the W and Z bosons become massive through the Higgs mechanism. With the discovery of the Higgs boson in 2012 [5] [6], the SM is complete. There are, however, phenomena that cannot be explained by the SM, for instance, dark matter, dark energy, baryon anti-baryon asymmetry, neutrino mass and mixing, and so on. Especially, the central question "Why did the Higgs field fill the universe and why at the electroweak scale ?" cannot be addressed by the SM. Since the Higgs boson is at the core of the electroweak symmetry breaking, a detailed examination of the Higgs boson is the key to understanding physics beyond the SM (BSM). An effective way to investigate BSM physics is to precisely measure the couplings of the Higgs boson to various particles. The measurements of the Higgs couplings fingerprint their deviation patterns from the SM with possible models of BSM physics. Figure 2 shows the deviation patterns for three typical cases: supersymmetry, minimal composite Higgs model, and just SM. To distinguish these different patterns, we need to measure the absolutely normalised Higgs couplings to a precision of $\sim 1\%$ or better.

2.2 International Linear Collider

The International Linear Collider (ILC) is an ideal machine to measure the Higgs couplings. The ILC is a future linear electron-positron collider, and will start its operation at the centre-of-mass energy ($\sqrt{s}$) of 250 GeV as a Higgs factory (ILC250), at which the $e^+e^- \to Zh$ cross

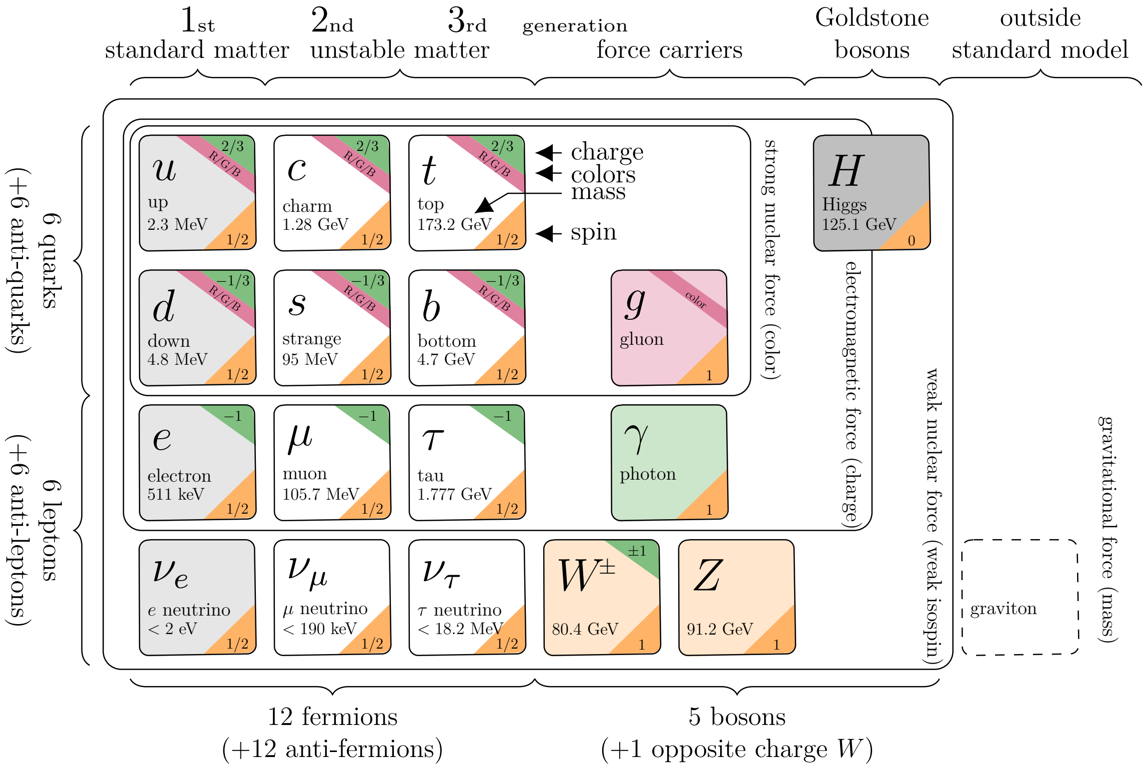

Figure 1: Particles in the SM (this image is created based on [4]).

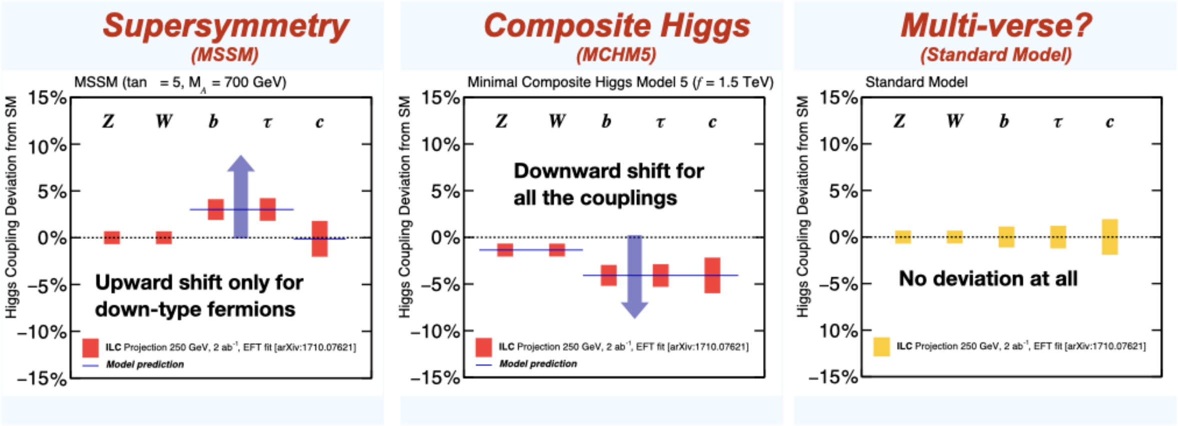

Figure 2: Deviation patterns of the couplings of the Higgs boson to various particles of the SM with possible models of BSM physics [7].

section attains its maximum as shown in Figure 3. With an integrated luminosity of 2 ab^{-1}, we can produce half a million Higgs bosons.

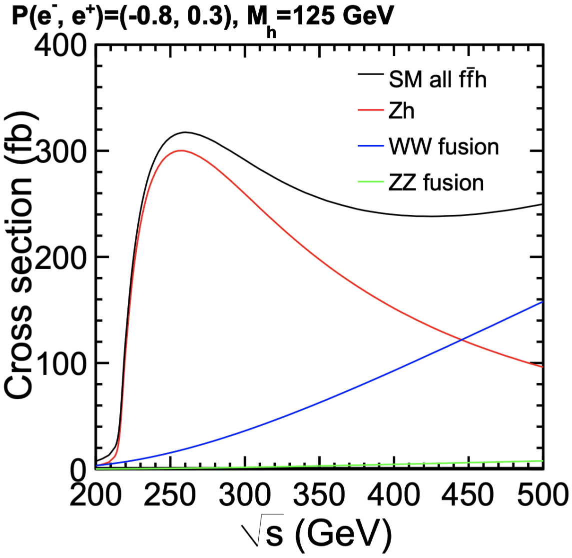

Figure 3: Higgs production cross section for the $e^+e^- \to Zh$, WW fusion, and ZZ fusion processes and their sum as a function of the $\sqrt{s}$ for m_h =125 GeV [8].

In the SM, the left- and right-handed fermions have different gauge charges. The left- and right-handed electrons are, hence, different particles with different interactions. The ILC has the advantage of polarising the positron beam by 30% and the electron beam by 80%, which can select reactions and disentangle contributions from left- and right-handed electrons. The polarisation P is defined as follows:

$$P \equiv \frac{N_R - N_L}{N_R + N_L}, \tag{2}$$

where $N_L(N_R)$ is the number of left- (right-) handed particles in a beam. In the rest of this chapter, we will give an overview of the physics, the accelerators, and the detectors of the ILC.

2.2.1 Higgs Physics at the ILC

The strength of the ILC is its ability to determine the absolutely normalised coupling constants, thanks to the so-called recoil mass technique usable only at lepton colliders. The recoil mass technique uses four-momentum conservation of the $e^+e^- \to Zh$ process to calculate the Higgs boson four-momentum by just measuring the Z boson decay products, taking advantage of the well-defined initial state with known four-momentum. We can then calculate the invariant mass of the system (the Higgs boson) recoiling against the Z boson without looking at the system at all. Figure 4 is the expected recoil mass distribution at the ILC. We can see a clear Higgs mass peak over the background. This technique allows us to measure the Higgs production cross section independently of the Higgs decay mode.

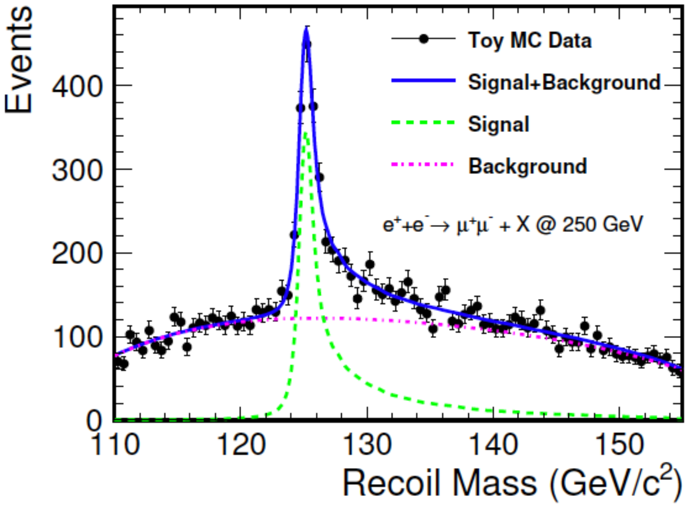

Figure 4: Recoil mass distribution for Z decay to $\mu^+\mu^-$ at ILC250 [9].

In order to extract coupling constants from branching ratios, we need to know the total width since the coupling constant squared is proportional to the partial width, which is equal to the branching ratio times the total width:

$$g_{hAA}^2 \propto \Gamma(h \to AA) = \Gamma_h \cdot BR(h \to AA), \tag{3}$$

where g_{hAA} is the Higgs coupling to particle A, $\Gamma(h \to AA)$ the partial width, Γ_h the total width, and $BR(h \to AA)$ the branching ratio. In order to determine the total width, we thus need at least one set of branching ratios and partial width measurements for some particle A. The traditional method is to use the W boson for A. This method, however, requires the cross section measurement of the W-fusion process: $e^+e^- \to \nu\bar{\nu}h$. It is difficult to measure this W-fusion process with sufficient precision at 250 GeV, because the cross section of W-fusion at $\sqrt{s} = 250$ GeV is too small as shown in Figure 3. The traditional method hence requires operating the machine at an energy > 350 GeV. A new method to avoid this higher energy running is to use the effective field theory (EFT). In the EFT framework, which is the parameter expansion of the BSM effect in terms of dimension-6 operators assuming that the new physics scale M is significantly larger than the centre-of-mass energy, the hZZ

and hWW couplings are related to each other through the $SU(2) \times U(1)$ symmetry. This allows us to determine the total width Γ_h at the $\sqrt{s} = 250$ GeV Higgs factory without using the W-fusion process at higher centre-of-mass energies. The EFT Lagrangian before the electroweak symmetry breaking can be expressed as the SM Lagrangian with the addition of the $SU(2) \times U(1)$ invariant dimension-6 operators. The additional terms relevant to the Higgs production processes are as follows [10]:

$$\begin{aligned}
\Delta\mathcal{L}_h =& \frac{c_H}{2v^2}\partial^\mu\left(\Phi^\dagger\Phi\right)\partial_\mu\left(\Phi^\dagger\Phi\right) + \frac{c_T}{2v^2}\left(\Phi^\dagger\overleftrightarrow{D}^\mu\Phi\right)\left(\Phi^\dagger\overleftrightarrow{D}_\mu\Phi\right) - \frac{c_6\lambda}{v^2}\left(\Phi^\dagger\Phi\right)^3 \\
&+ \frac{g^2 c_{WW}}{m_W^2}\Phi^\dagger\Phi W^a_{\mu\nu}W^{a\mu\nu} + | \frac{4gg' c_{WB}}{m_W^2}\Phi^\dagger t^a\Phi W^a_{\mu\nu}B^{\mu\nu} \\
&+ \frac{g'^2 c_{BB}}{m_W^2}\Phi^\dagger\Phi B_{\mu\nu}B^{\mu\nu} + \frac{g^3 c_{3W}}{m_W^2}\epsilon_{abc}W^a_{\mu\nu}W^{b\nu}{}_\rho W^{c\rho\mu} \\
&+ i\frac{c_{HL}}{v^2}\left(\Phi^\dagger\overleftrightarrow{D}^\mu\Phi\right)\left(\bar{L}\gamma_\mu L\right) + 4i\frac{c'_{HL}}{v^2}\left(\Phi^\dagger t^a\overleftrightarrow{D}^\mu\Phi\right)\left(\bar{L}\gamma_\mu t^a L\right) \\
&+ i\frac{c_{HE}}{v^2}\left(\Phi^\dagger\overleftrightarrow{D}^\mu\Phi\right)\left(\bar{e}\gamma_\mu e\right),
\end{aligned} \tag{4}$$

which contain 10 coefficients: c_H, c_T, c_6, c_{WW}, c_{WB}, c_{BB}, c_{3W}, c_{HL}, c'_{HL}, and c_{HE}. After electroweak symmetry breaking, this becomes

$$\begin{aligned}
\Delta\mathcal{L}_h = -\eta_h\lambda_0 v_0 h^3 + \tfrac{\theta_h}{v_0}h\partial_\mu h\partial^\mu h + \eta_Z\tfrac{m_Z^2}{v_0}Z_\mu Z^\mu h + \tfrac{1}{2}\eta_{2Z}\tfrac{m_Z^2}{v_0^2}Z_\mu Z^\mu h^2 \\
+\eta_W\tfrac{2m_W^2}{v_0}W^+_\mu W^{-\mu}h + \eta_{2W}\tfrac{m_W^2}{v_0^2}W^+_\mu W^{-\mu}h^2 \\
+\tfrac{1}{2}\left(\zeta_Z\tfrac{h}{v_0} + \tfrac{1}{2}\zeta_{2Z}\tfrac{h^2}{v_0^2}\right)\hat{Z}_{\mu\nu}\hat{Z}^{\mu\nu} + \left(\zeta_W\tfrac{h}{v_0} + \tfrac{1}{2}\zeta_{2W}\tfrac{h^2}{v_0^2}\right)\hat{W}^+_{\mu\nu}\hat{W}^{-\mu\nu} \\
+\tfrac{1}{2}\left(\zeta_A\tfrac{h}{v_0} + \tfrac{1}{2}\zeta_{2A}\tfrac{h^2}{v_0^2}\right)\hat{A}_{\mu\nu}\hat{A}^{\mu\nu} + \left(\zeta_{AZ}\tfrac{h}{v_0} + \zeta_{2AZ}\tfrac{h^2}{v_0^2}\right)\hat{A}_{\mu\nu}\hat{Z}^{\mu\nu}.
\end{aligned} \tag{5}$$

At the ILC, we can independently determine these unknown coefficients, taking advantage of beam polarisations that double the number of independent observables.

2.2.2 Accelerator of the ILC

The major components of the ILC machine are

1. electron source,
2. positron source,
3. damping ring,
4. main linear accelerators,
5. final focusing system, and

6. detectors at the interaction point.

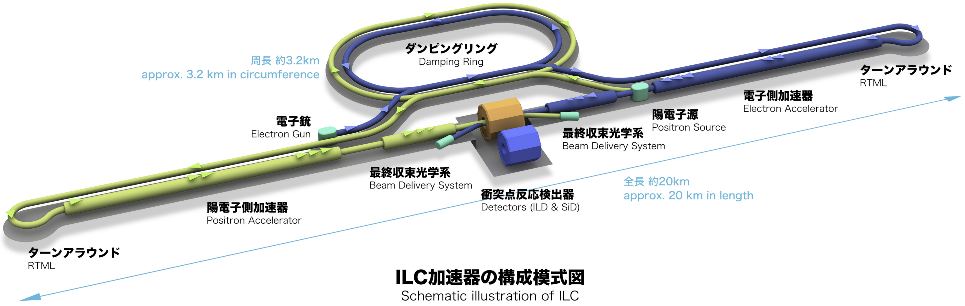

Figure 5: Image of the ILC [11]©Rei.Hori/KEK.

Figure 5 shows the schematic image of the ILC. First, electrons are produced by applying a laser beam to the material and utilising the photoelectric effect. In the ILC, ±80% polarised electrons beams can be generated using a circularly polarised laser beam on a gallium arsenide photocathode. Second, positrons are produced by using the generated electrons. There are currently two options considered for generating positrons, the undulator method and the conventional electron-driven method. In the case of the undulator method, it is possible to produce positrons with a polarisation of ±30%. Then the generated electrons and positrons are bunched together and go to the damping ring. The damping ring serves to reduce emittance by aligning the particles in the same direction. As the not aligned electrons circulate in the damping ring, they lose momentum by synchrotron radiation both perpendicular and parallel to the accelerating field. Thus, their direction is aligned by recovering momentum only in the parallel direction.

The ILC beam is a collection (trains) of 1300 bunches. Trains are produced every 200 ms as shown in Figure 6. We must treat huge size data taken in a short time. Many other high energy accelerators have a trigger to select the event of interest. However, at the ILC, we plan to read out data in the interval between trains. Data can thus be accumulated without

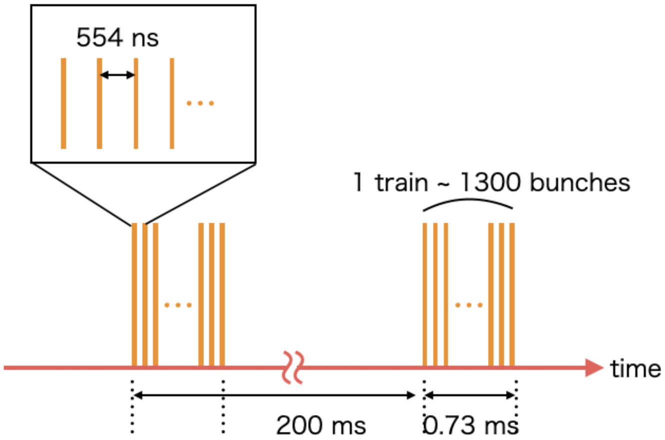

Figure 6: Bunch structure of the ILC.

the trigger. In addition, we will supply power to front-end electronics only during bunch collision, which is so-called power pulsing, to reduce power consumption and the cooling system burden.

In the main linac, the beam is accelerated in nine-cell superconducting cavities made of niobium, operating at gradient about 31.5 MV/m. The particles in the cell are constantly accelerated by radiofrequency (RF) electromagnetic waves adapted to the size of the cell. Finally, the beam enters the final focus system, which consists of many magnets to focus the beams and achieve high luminosity. The following equation can express the luminosity $\mathcal{L}$:

$$\mathcal{L} = \frac{fN^2}{4\pi\sigma_x\sigma_y}, \tag{6}$$

where f is repetition rate of the accelerator, N is the number of particles in each beam bunch, $\sigma_x(\sigma_y)$ is beam size in the horizontal (vertical) direction. The $\sigma_x(\sigma_y)$ is preferred to be as small as possible to increase the luminosity. In the vicinity of the collision of the beams, a phenomenon called the beamstrahlung occurs. It is the bremsstrahlung from beam particles bent by the electromagnetic field produced by the oncoming beam. The beamstrahlung causes beam energy loss, which widens the beam energy distribution and reduces the luminosity at the highest energy. This effect can be suppressed by increasing the beam circumference $(\sigma_x + \sigma_y)$. Therefore, a flat beam, 7.7 nm thick, 516 nm wide, is selected to suppress the beamstrahlung. For the ILC at $\sqrt{s} = 250$ GeV, a luminosity of 1.35×10^{34} cm^{-2}s^{-1} is expected to be achieved.

The ILC is designed to have two different detectors which use a single collision point alternately in so-called push-pull system. The two proposed detectors are the International

Large Detector (ILD) and the Silicon Detector (SiD). The Japanese group is mainly involved in the development of the ILD.

2.2.3 International Large Detector

Figure 7 shows a cross-sectional view of the ILD detector. It has a radius of about 8 m and a total length of about 14 m. A superconducting solenoid with an inner radius of about 3.5 m and a length of about 4 m produces a magnetic field of 3.5 T.

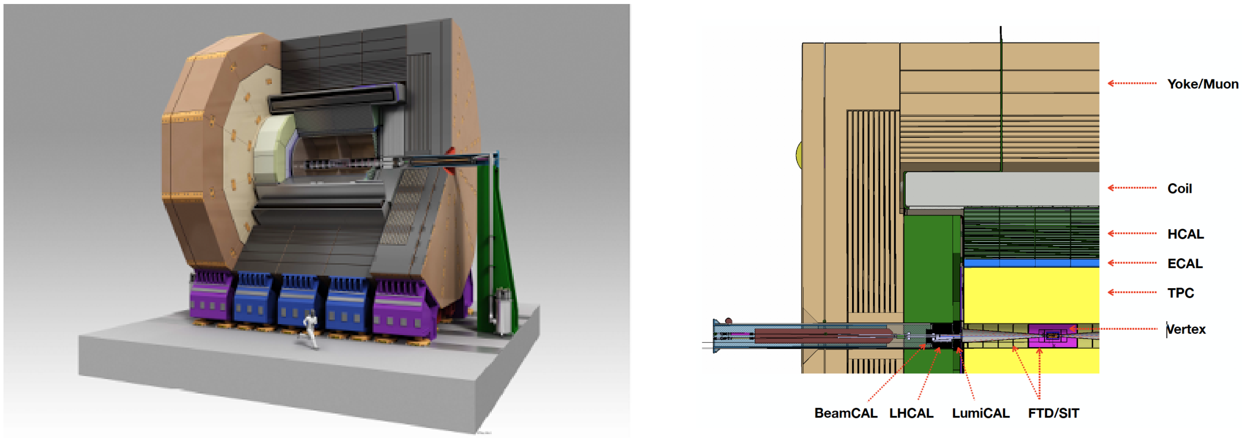

Figure 7: Overview of the ILD (left) [11] and the cross-sectional view of the ILD detector (right) [12].

The ILD consists of layers of sub-detectors: the VerTeX detector (VTX), the central tracker (Time Projection Chamber: TPC), Electromagnetic CALorimeter (ECAL), Hadron CALorimeter (HCAL), and the muon detector surrounding the collision point. In addition, silicon-based detectors such as the Silicon Internal Tracker (SIT), which surrounds the vertex detector, the Silicon External Tracker (SET), which is placed outside the TPC, contribute to the tracking system. the Forward Tracking Disks (FTD) cover the forward region. Table 1 is the summary table of function and geometry of each sub-detector (Barrel region).

For the Higgs precision measurement, the ILD is required to have momentum resolution high enough that detector errors can be neglected for beam energy fluctuations. The key measurement for precision Higgs studies at the ILC is that of the $e^+e^- \rightarrow Zh$ process followed by $Z \rightarrow \mu^+\mu^-$ decay, with the recoil mass technique. The width of the recoil mass peak depends on both the beam energy spread and the muon momentum resolution. Figure 8 compares recoil mass distributions for two different momentum resolution cases: 2.0×10^{-5} GeV$^{-1} \cdot$ c and 8.0×10^{-5} GeV$^{-1} \cdot$ c [13]. To make the contribution from the momentum resolution negligible, we need the momentum resolution of $\frac{\sigma_{P_T}}{P_T^2}$ of 2×10^{-5} GeV$^{-1} \cdot$ c.

To achieve this momentum goal, the trackers are required to have high momentum resolution. VTX with a few μm spatial resolution is placed just outside the interaction point.

Table 1: Summary table of function and geometry of each sub-detector(Barrel region) [12].

System	R(in) [mm]	R(out) [mm]	z [mm]	function	Comment
VTX	16	60	125	identify vertexes	3 layers double-sided ladders(R=16 mm, 37 mm, and 58 mm), Silicon pixel sensors
Silicon					
SIT	153	300	644	provide hit point	2 silicon strip layers
SET	1811		2300	provide hit point	2 silicon strip layers
TPC	330	1808	2350	Track position with 200 hit points	Gas detector, readout anode with 1 × 6mm^2 pads.
ECAL	1843	2028	2350	Measure electromagnetic jet energy	(SiECAL) 30 Silicon sensor layers, 5 × 5mm^2 cells. (ScECAL) 30 Scintillator layers, 5 × 45mm^2 strips
HCAL	2058	3410	2350	Measure hadron jet energy	(AHCAL) 48 Scintillator layers, 3 × 3cm^2 cells, analogue. (SDHCAL) 48 Gas RPC layers, 1 × 1cm^2 cells, semi-digital
Coil	3440	4400	3950		3.5 T
Muon	4450	7755	2800	detect muon	14 scintillator layers.

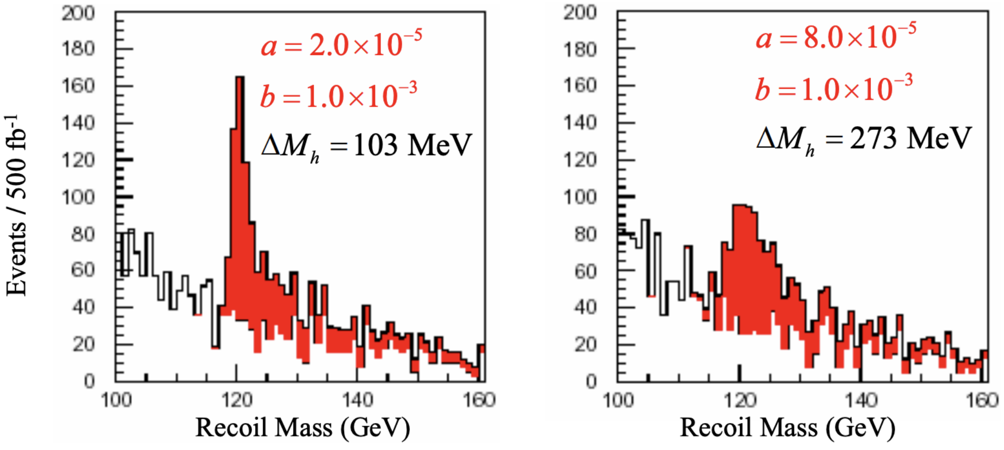

Figure 8: Recoil mass distributions for two momentum resolution cases: $a = 2.0 \times 10^{-5}$ GeV^{-1}c and $a = 8.0 \times 10^{-5}$ [13], where $\frac{\sigma_{P_T}}{P_T^2} = a \oplus b/p_t \sin\theta$ GeV^{-1}c [12].

The SIT, which surrounds the vertex detector, the TPC, the SET, which is placed just outside the TPC provide many track hit points. The TPC reconstructs charged particles bent by a magnetic field in three dimensions and measures the momentum from their curvature. The performance target of momentum resolution is $\frac{\sigma_{P_T}}{P_T^2}$ of 1×10^{-4} GeV$^{-1} \cdot$ c. To precisely measure the curvature, The TPC is required to have single hit $r\phi$ (transverse) resolution better than 100 μm.

Another important concept of the ILD is the Particle Flow Algorithm (PFA), which measures all particles accurately and without duplication. The key of PFA is effective separation of the hadron jets from Z bosons and W bosons better than 3σ in the mass peaks. This requires a di-jet invariant mass resolution of $\frac{\sigma_m}{m} = 2.7\% \approx \frac{\Gamma_\mathrm{W}}{\mathrm{m_W}} \approx \frac{\Gamma_\mathrm{Z}}{\mathrm{m_Z}}$. Using the daughter jets, energies (E_i and E_j), the invariant mass of Z and W can be written as $m_{ij} = 2E_iE_j\left(1 - \cos\theta_{ij}\right)$, where θ_{ij} is the angle between the 2 jets. We therefore require the jet energy resolution to be about 3% or better.

Two types of calorimeter are used to measure jet energy: electromagnetic calorimeters (ECAL), which measure electromagnetic showers, and hadron calorimeter (HCAL), which capture hadrons. There are two options for electromagnetic calorimeters: one is SiECAL, which uses silicon for the sensor, and the other is ScECAL, which uses a scintillator. The detected total energy in calorimeters is $E_c + E_n = \left(\tilde{E}_c + \Delta E_c\right) + \left(\tilde{E}_n + \Delta E_n\right)$. where E_c is the energy deposit by charged particles, E_n is that by neutral particles, $\tilde{E}$ is the true energy, and ΔE is its error. The energy resolution for hadrons is about $\frac{50\%}{\sqrt{E}}$, and that of photons and electrons is $\frac{17\%}{\sqrt{E}}$ [9], i.e. the magnitude and the shape of the hadron shower has a significantly more fluctuation than an electromagnetic shower.

The momentum of a charged particle can be measured more accurately with a tracker than with a calorimeter. Hence the charged particles are measured with a tracker and the neutral particles with a calorimeter to achieve a better energy resolution. When we measure the charged particle using the tracker and suppress its signal from the calorimeter, we can ignore the energy fluctuation of the charged particle ΔE_c. This method allows achieving the target jet energy resolution.

To remove the charged particle energy deposit in the calorimeter for PFA, the TPC track should be linked to the calorimeter signals. Therefore, even if several tracks are close to each other, the tracker needs to have enough resolution to separate them so as not to lose any information. The required 2-hit resolution in $r\phi$ is 2 mm and is 6 mm in z. It is also capable of dE/dx-based particle identification. Especially the separation between π and K is important for jet charge identification.

The vertex detector has an important role in identifying charm quarks, bottom quarks, and tau leptons. Table 2 shows which sub-detector is sensitive to each kind of particle.

Table 2: Summary table of each sub-detector's role for PFA.

	$e^\pm$	$\mu^\pm$	$\pi^\pm$	$K^\pm$	p	n	γ	$K_s \rightarrow \pi^+\pi^-$	$K_s \rightarrow \pi_0\pi_0 \rightarrow 4\gamma$	K_L	$\pi_0 \rightarrow 2\gamma$
Tracker	✓	✓	✓	✓	✓			✓			
ECAL	✓	✓	✓	✓	✓	✓	✓	✓	✓		✓
HCAL		✓	✓	✓	✓	✓		✓		✓	
μ		✓									

Part 1

3 Study of photon-associated Higgs production at the ILC

3.1 Introduction and Motivation

The primary motivation of this study is to determine the SM effective field theory(SMEFT) coefficient that are relevant to $h\gamma\gamma$ and $h\gamma Z$ couplings using $e^+e^- \to h\gamma$ process. A previous study [14] showed that the $e^+e^- \to h\gamma$ is difficult to observe in the case of the SM, but can be used to discover various BSM scenarios. However this study did not use full detector simulation, and used only a cut based event selection. We therefore performed a first full-simulation study, using a realistic detailed model of the ILD at ILC250. Our study is the first study with realistic detailed detector model. We declared an event selection and estimated the expected upper limits on the cross sections of the $e^+e^- \to h\gamma$ process at the ILC250 for the two beam polarisation combinations. The upper limit is then interpreted using model-independent EFT coefficients, and also in terms of the electron Yukawa coupling.

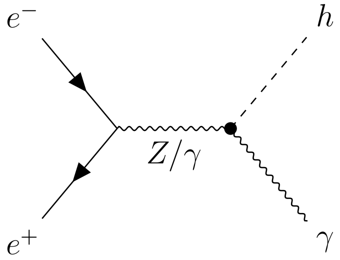

Figure 9: Feynman diagram of $e^+e^- \to h\gamma$.

3.2 Theoretical Framework

As mentioned above, Higgs-related SMEFT coefficients must be constrained to extract absolutely normalised Higgs couplings. In the SMEFT Lagrangian, the terms relevant to the $h\gamma\gamma$ and $h\gamma Z$ couplings are

$$\Delta\mathcal{L}_{h\gamma\gamma,h\gamma Z} = \mathcal{L}_{SM} + \frac{\zeta_{AZ}}{v} A_{\mu\nu} Z^{\mu\nu} h + \frac{\zeta_A}{2v} A_{\mu\nu} A^{\mu\nu} h, \tag{7}$$

with

$$\zeta_A = 8s_w^2\left((8c_{WW}) - 2\,(8c_{WB}) + (8c_{BB})\right) \tag{8}$$

$$\zeta_{AZ} = s_w c_w \left((8c_{WW}) - \left(1 - \frac{s_w^2}{c_w^2}\right)(8c_{WB}) - \frac{s_w^2}{c_w^2}\,(8c_{BB})\right), \tag{9}$$

where $A_{\mu\nu}$, $Z_{\mu\nu}$ are field strength tensors for photon and Z boson and v is the Higgs vacuum expectation value, and $s_w \equiv \sin\theta_w$, $c_w \equiv \cos\theta_w$, and c_{WW}, c_{WB}, c_{BB} are SMEFT coefficient in the Warsaw basis [10]. The coefficient ζ_A can be determined precisely by measurement of the $h \to \gamma\gamma$ partial width at LHC. The coefficient ζ_{AZ} can be also determined by the measurement of the $h \to \gamma Z$ partial width, which is expected to be much less precisely determined than the $h \to \gamma\gamma$. Thus we are motivated to determine ζ_{AZ} in a complementary way, that is to use the measurement of the cross section of $e^+e^- \to h\gamma$ at the ILC.

The leading Feynman diagrams for $e^+e^- \to h\gamma$ in the SM are shown in Figure 10. Figure 11 shows the cross section for each diagram, and their total. Large destructive interference occurs between these diagrams. The SM cross sections for different beam polarisations are shown in Table 3. σ^L_{SM} represent the cross section which beam polarisation $(P_{e^-}, P_{e^+}) = (-100\%, +100\%)$ (left-handed), σ^R_{SM} is $(P_{e^-}, P_{e^+}) = (+100\%, -100\%)$ (right-handed) case, σ^-_{SM} is $(P_{e^-}, P_{e^+}) = (-80\%, +30\%)$ case, and σ^+_{SM} is $(P_{e^-}, P_{e^+}) = (+80\%, -30\%)$ case. These cross sections are much smaller than 1 fb. It is thus expected that the measurement of this process is very challenging. This small cross section is also a potential advantage, since it will be easier to see the effects of BSM [1] [15]. We naively expect to have narrow limits as shown in Figure 12 in the ideal case of no backgrounds and 100% signal efficiency using the $h \to b\bar{b}$ channel only.

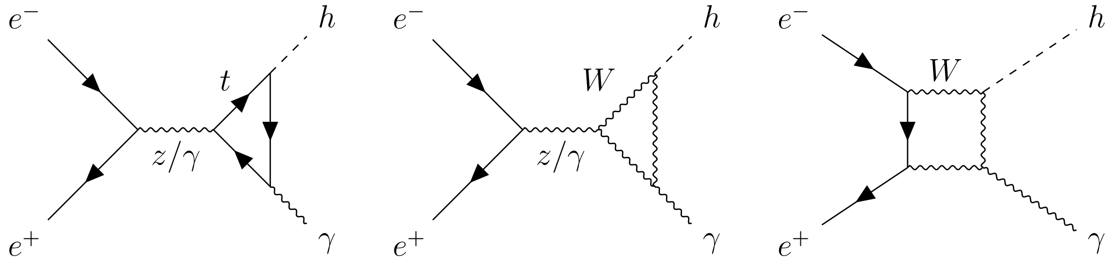

Figure 10: Loop-induced Feynman diagrams in the SM for $e^+e^- \to h\gamma$: (left) top quark loop, (centre) W boson loop, and (right) box diagram with internal W boson lines.

Table 3: SM cross sections for $e^+e^- \to h\gamma$ for different beam polarisations at $\sqrt{s} = 250$ GeV. $\sigma^{L,R}_{SM}$ are for 100% beam polarisation and $\sigma^{\pm}_{SM}$ are 80% electron and and 30% positron polarisations. [16]

	P_{e^-}	P_{e^+}	σ_{SM}[fb]
σ^L_{SM}	−100%	+100%	0.35
σ^R_{SM}	+100%	−100%	0.016
σ^-_{SM}	−80%	+30%	0.20
σ^+_{SM}	+80%	−30%	0.021

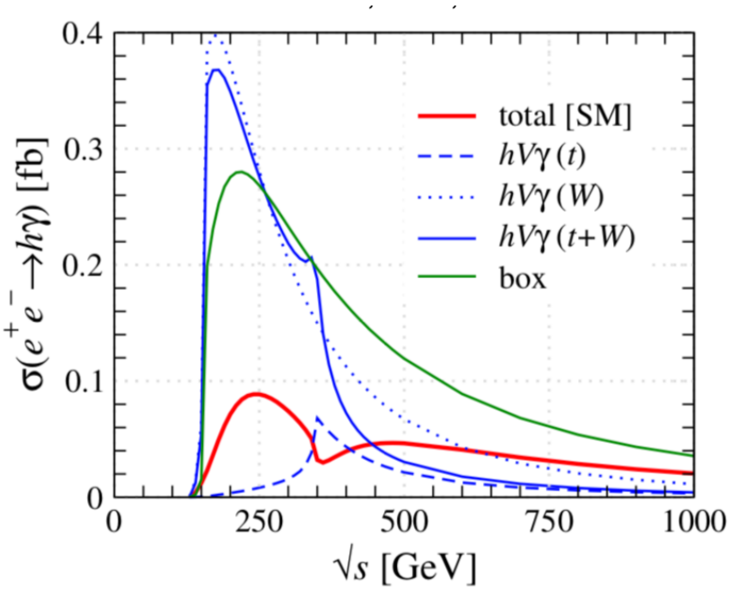

Figure 11: Contributions from individual diagrams of Figure 10 to $\sigma(e^+e^- \to h\gamma)$. The figure shows the cross-section of the diagram with top-quark in the loop (dashed blue line), the W boson in the loop (dotted blue line), their sum (solid blue line), the box diagram with W boson loop (solid green line). The red line is the total of all contributions [1].

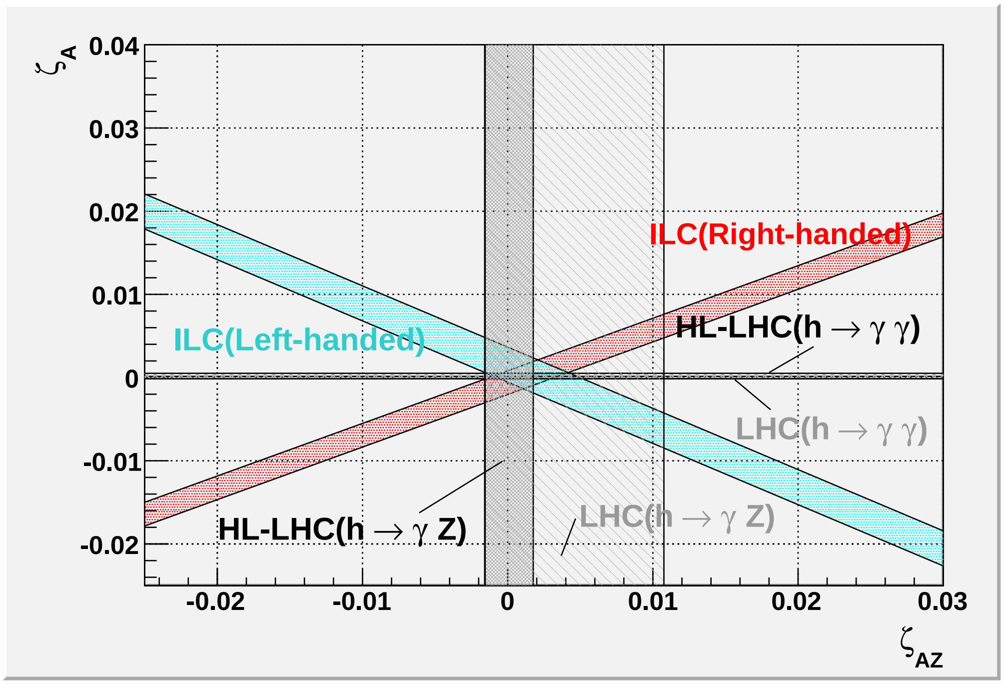

Figure 12: ILC limits on ζ_A and ζ_{AZ} in the left-handed (blue area) and right-handed (red area) polarisations, in the case of no experimented backgrounds and perfect selection efficiency, compared to limits from LHC and HL-LHC.

3.3 Simulation Framework

We performed a full simulation assuming a realistic ILD model. First, we generated the signal events using `Physsim` [17], including SM full 1-loop contribution for the matrix element calculation. For background, we used the events which had been produced for the ILD DBD study [12] using `Whizard` [18]. Full SM $e^+e^- \to$ 2-fermion (2f) and 4-fermion (4f) mainly $Z^+Z^-/W^+W^- \to$ 4f background events are included in this analysis. Initial State Radiation (ISR) and beamstrahlung effects were included.

All generated events are fully simulated with `Geant4` [2] for the ILD DBD model using `Mokka` [19]. The simulated events are then reconstructed using Marlin in `iLCSoft` [20], where particle flow analysis (PFA) is performed with `PandoraPFA` [21] and flavor tagging is done with `LCFI+` [22]. The analysis is carried out at $\sqrt{s} = 250$ GeV. According to the ILC run scenario [23], the ILC will accumulate 2 ab^{-1} data in 11 years at $\sqrt{s}$ =250 GeV. The integrated luminosity is 900 fb^{-1} for $(P_{e^-}, P_{e^+}) = (-80\%, +30\%)$ and $(+80\%, -30\%)$ polarisations, and 100 fb^{-1} for $(P_{e^-}, P_{e^+}) = (-80\%, +30\%)$ and $(+80\%, -30\%)$, respectively. In this study, we assume an integrated luminosity of 900 fb^{-1} for both $(P_{e^-}, P_{e^+}) = (-80\%, +30\%)$ and $(P_{e^-}, P_{e^+}) = (+80\%, -30\%)$.

3.4 Event Selection and Significance

Here we describe the procedure of signal event selection, background event suppression, and evaluation of the resulting signal significance. The signal process is $e^+e^- \to h\gamma$. We focus on the leading Higgs decay channels: $h \to b\bar{b}$ and $h \to WW^*$ (semi-leptonic) final states.

3.4.1 Pre-selection

All signal channels are characterized by the presence of an isolated photon. The signature of the signal events in this channel is one monochromatic energetic photon $E_\gamma = \sqrt{s}/2\left(1 - (m_h/\sqrt{s})^2\right) \sim 93$ GeV, where m_h is the Higgs mass. First, for every event, it is necessary to find at least one photon with an energy greater than 50 GeV. `PandoraPFA` supplies the photon identification algorithm. If more than one photon is found, the most energetic photon is selected as the signal photon. The remaining particles in every event other than the signal photon undergo the following channel-specific event selections.

3.4.2 $h \to b\bar{b}$ Channel

The energy resolution of the electromagnetic calorimeter is typically $\sigma_E = 17\%/\sqrt{E}$, where the energy E is in unit of GeV. The energy resolution for the isolated photon is thus around 1.9 GeV. There are also two b-jets whose invariant mass should be consistent with the Higgs mass 125 GeV. The particles other than the signal photon identified above are clustered into two jets using the Durham jet clustering algorithm [24]. The two jets are both flavor-tagged using the algorithm in `LCFI+`. Figure 13 and Figure 14 show the distributions of the larger of the two jet b-tag probabilities and the total missing energy, respectively for both $(P_{e^-}, P_{e^+}) = (-80\%, +30\%)$ and $(P_{e^-}, P_{e^+}) = (+80\%, -30\%)$. For each event, the highest b-likeliness of the two jets (named b-likeliness cut) is required to be greater than 0.77 to suppress events with other flavor jets. We also require total missing energy less than 35 GeV because the signal does not contain any neutrino, and we therefore expect small missing energy.

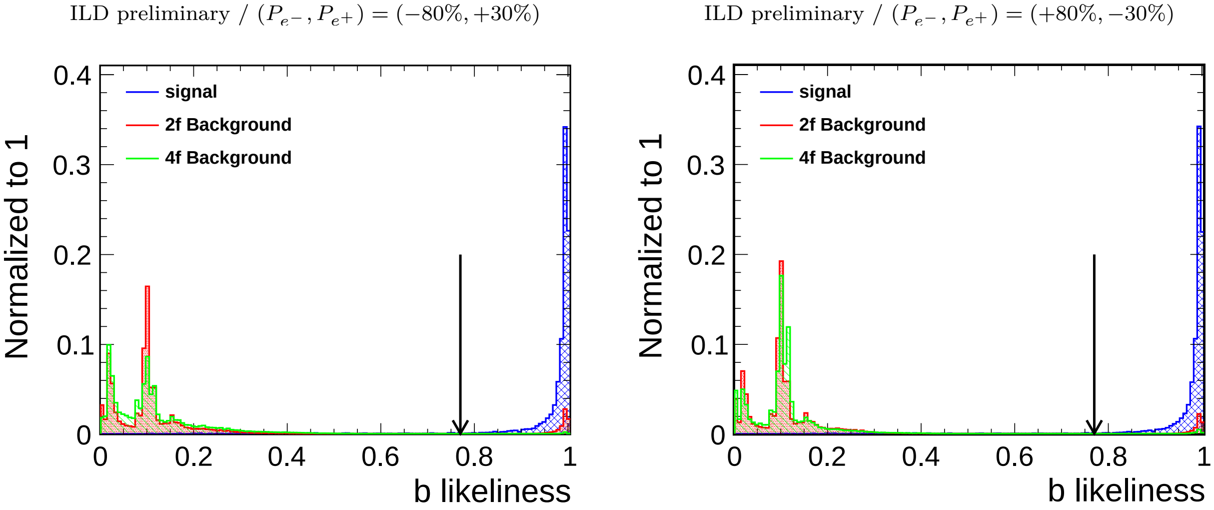

Figure 13: Distributions of the larger jet b-likeliness for signal, $2f$ and $4f$ events: (left) $(P_{e^-}, P_{e^+}) = (-80\%, +30\%)$, (right) $(P_{e^-}, P_{e^+}) = (+80\%, -30\%)$. Arrows shows the applied cuts.

The remaining background events after these cuts are supplied to a boosted decision trees (BDT) multivariate analysis (MVA), using the Toolkit for Multivariate Data Analysis (TMVA) package [25] of ROOT 5. We use following four input variables: the energy of the signal photon, the reconstructed Higgs mass, the angles between the signal photon and each of the two b-jets, and the angle between the two b-jets (Figure 15). Note that we used a new method to reconstruct the Higgs di-jet mass. In this method, the Higgs di-jet mass is reconstructed as an invariant mass of the two b-jets. Jet energies are calculated from the measured photon transverse momentum, b-jets directions and masses, imposing conservation of transverse momentum [26]. Compared to the recoil mass technique, the new method has advantages not sensitive to ISR and beamstrahlung effect. The MVA is first trained using half of the events, and then applied to the other half. Figure 16 shows the BDT output response. It was confirmed that there is no overtraining. Figure 17 shows the cut efficiency and the signal significance. We require the BDT output value for each event to be larger

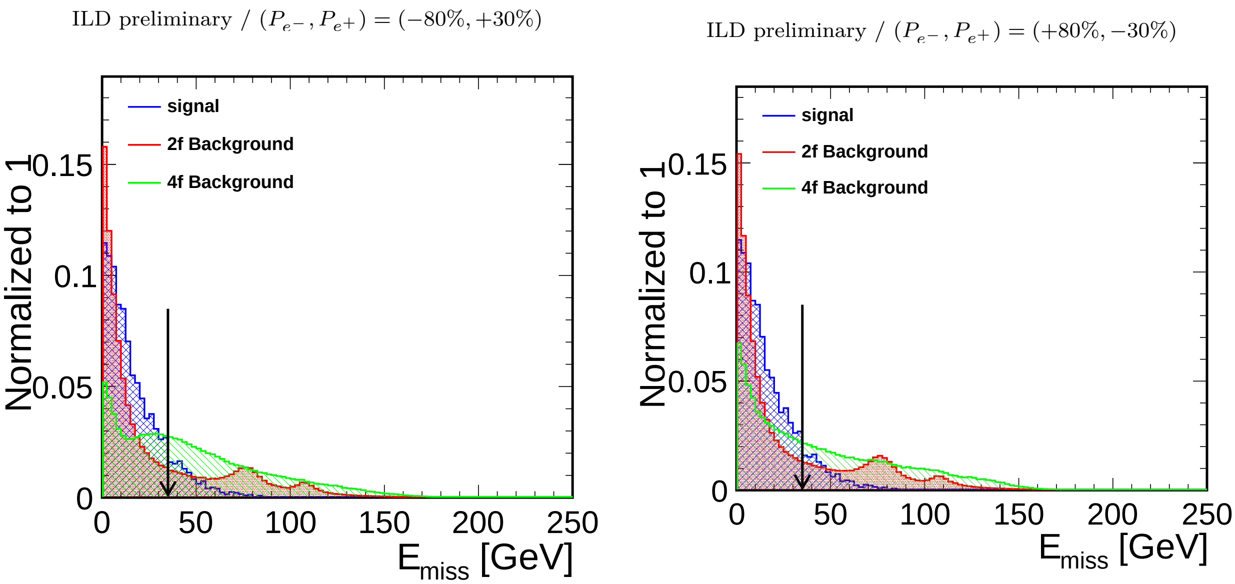
ILD preliminary / $(P_{e^-}, P_{e^+}) = (-80\%, +30\%)$

ILD preliminary / $(P_{e^-}, P_{e^+}) = (+80\%, -30\%)$

Figure 14: Distributions of the total missing energy of the signal, $2f$, and $4f$ events: (left) $(P_{e^-}, P_{e^+}) = (-80\%, +30\%)$, (right) $(P_{e^-}, P_{e^+}) = (+80\%, -30\%)$.

than 0.025.

As the final event selection, we applied a cut on the polar angle of the signal photon. As can be seen in Figure 18, photon in the backgrounds are often in the forward region. To suppress these backgrounds, we require to be $|\cos\theta_\gamma| < 0.92$.

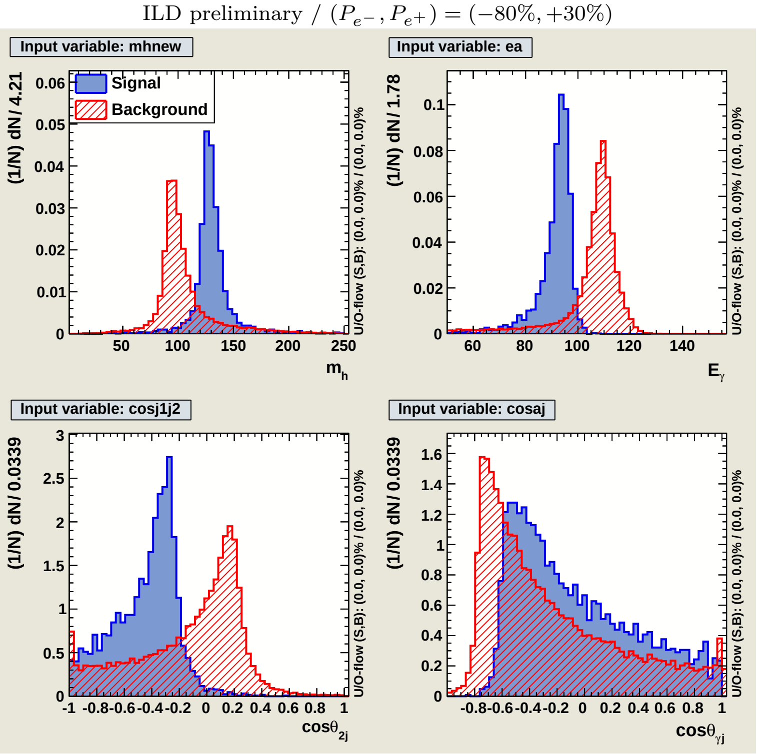

ILD preliminary / $(P_{e^-}, P_{e^+}) = (-80\%, +30\%)$

Figure 15: Distributions of input observables for MVA in $h \to b\bar{b}$ analysis. The blue histograms show the signal, and the red hatched histograms show the total background. Clockwise from top left: reconstructed Higgs mass, photon energy, cosine of the angle between the two jets, cosine of the larger of the angles between the signal photon and the b-jets.

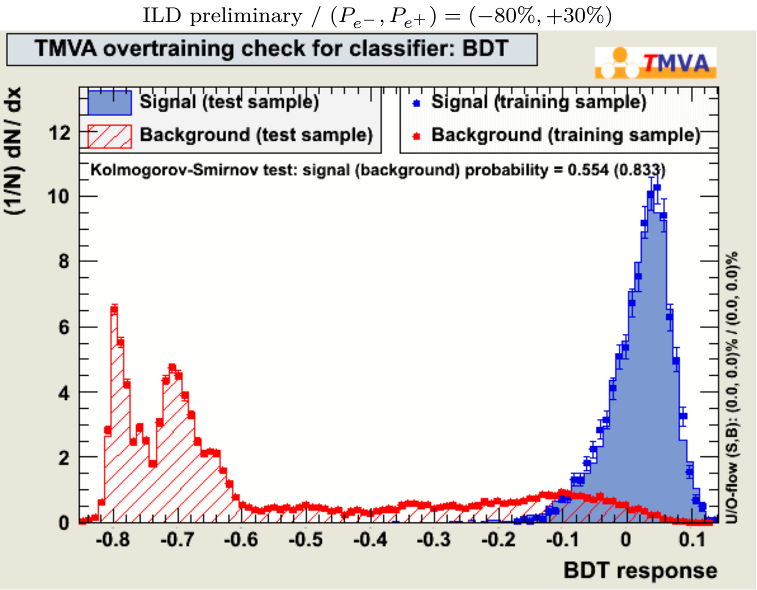

Figure 16: BDT output in the $h \to b\bar{b}$ analysis. The training sample and test sample are consistent.

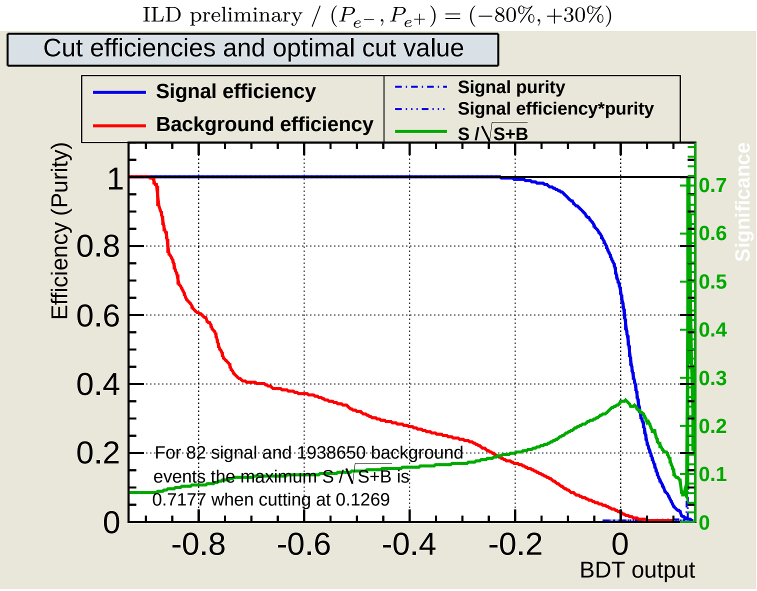

Figure 17: Signal and background separation as a function of the cut on the MVA output, in the $h \to b\bar{b}$ analysis.

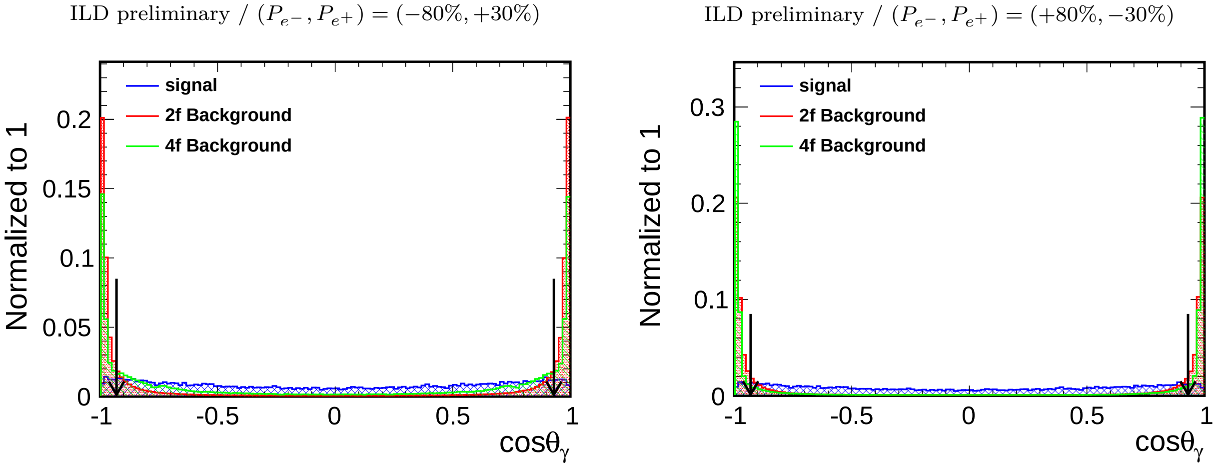

Figure 18: Distributions of the photon $\cos\theta_\gamma$ in signal, $2f$, and $4f$ events: (left) $(P_{e^-}, P_{e^+}) = (-80\%, +30\%)$, (right) $(P_{e^-}, P_{e^+}) = (+80\%, -30\%)$ in the $h \to b\bar{b}$ channel.

Table 4 shows a number of signal and background events as well as the signal significance in the $h \to b\bar{b}$ channel of $(P_{e^-}, P_{e^+}) = (-80\%, +30\%)$ after each event selection cut. The signal significance is defined as follows,

$$\text{Significance}\,(n_{sig}) \equiv \frac{N_S}{\sqrt{N_S + N_B}}, \tag{10}$$

where N_S is the number of selected signal events and N_B is the number of selected background events. Table 5 shows the similar table for $(P_{e^-}, P_{e^+}) = (+80\%, -30\%)$. After all cuts, we expect 29 signal events and 12 thousand background events for the SM signal process, with a signal significance of 0.26σ for $(P_{e^-}, P_{e^+}) = (-80\%, +30\%)$. For $(P_{e^-}, P_{e^+}) = (+80\%, -30\%)$, 3 signal events and 5.9×10^3 background event remain giving a significance is $3.9 \times 10^{-2}\sigma$.

Table 4: Expected number of events in $h \to b\bar{b}$ channel after applying the selection cuts ($(P_{e^-}, P_{e^+}) = (-80\%, +30\%)$), after applying the selection cuts.

$(P_{e^-}, P_{e^+}) = (-80\%, +30\%)$, $\int \mathcal{L} = 900$ fb^{-1}, $\sqrt{s} = 250$ GeV

	2f	4f	total bg	Signal	Significance
Expected	1.0×10^8	3.7×10^7	1.4×10^8	1.1×10^2	9.0×10^{-3}
Pre selection	2.8×10^7	1.6×10^6	2.9×10^7	9.9×10^1	1.8×10^{-2}
b likeliness> 0.77	2.2×10^6	2.1×10^4	2.2×10^6	9.0×10^1	6.0×10^{-2}
$E_{mis} < 35$ GeV	1.9×10^6	1.6×10^4	1.9×10^6	8.2×10^1	5.9×10^{-2}
mvabdt > 0.025	1.9×10^4	3.2×10^2	2.0×10^4	3.4×10^1	2.4×10^{-1}
$-0.92 < \cos\theta_\gamma < 0.92$	1.2×10^4	1.3×10^2	1.2×10^4	2.9×10^1	2.6×10^{-1}

Table 5: Expected number of events in $h \to b\bar{b}$ channel ($(P_{e^-}, P_{e^+}) = (+80\%, -30\%)$), after applying the selection cuts.

$(P_{e^-}, P_{e^+}) = (+80\%, -30\%)$, $\int \mathcal{L} = 900$ fb^{-1}, $\sqrt{s} = 250$ GeV

	2f	4f	total bg	Signal	Significance
Expected	7.3×10^7	4.6×10^6	7.8×10^7	1.1×10^1	1.3×10^{-3}
Pre selection	2.3×10^7	4.7×10^5	2.3×10^7	1.0×10^1	2.1×10^{-3}
b likeliness> 0.77	1.4×10^6	9.3×10^3	1.5×10^6	9.4	7.8×10^{-3}
$E_{mis} < 35$ GeV	1.3×10^6	7.7×10^3	1.3×10^6	8.4	7.5×10^{-3}
mvabdt > 0.025	1.0×10^4	2.1×10^2	1.0×10^4	3.4	3.4×10^{-2}
$-0.92 < \cos\theta_\gamma < 0.92$	5.9×10^3	5.7×10^1	5.9×10^3	3.0	3.9×10^{-2}

For both $(P_{e^-}, P_{e^+}) = (-80\%, +30\%)$ and $(P_{e^-}, P_{e^+}) = (+80\%, -30\%)$ beam polarisation combinations, the dominant background is $e^+e^- \to \gamma Z$ followed by $Z \to f\bar{f}$, mainly $Z \to b\bar{b}$.

Among $Z \rightarrow \mathrm{f\bar{f}}$, any flavor other than b can be relatively easily removed by cutting on b-likeliness as shown in Figure 19. However, $Z \rightarrow b\bar{b}$ was difficult to remove even using the reconstructed Higgs mass, E_γ and $cos\theta_\gamma$ cuts.

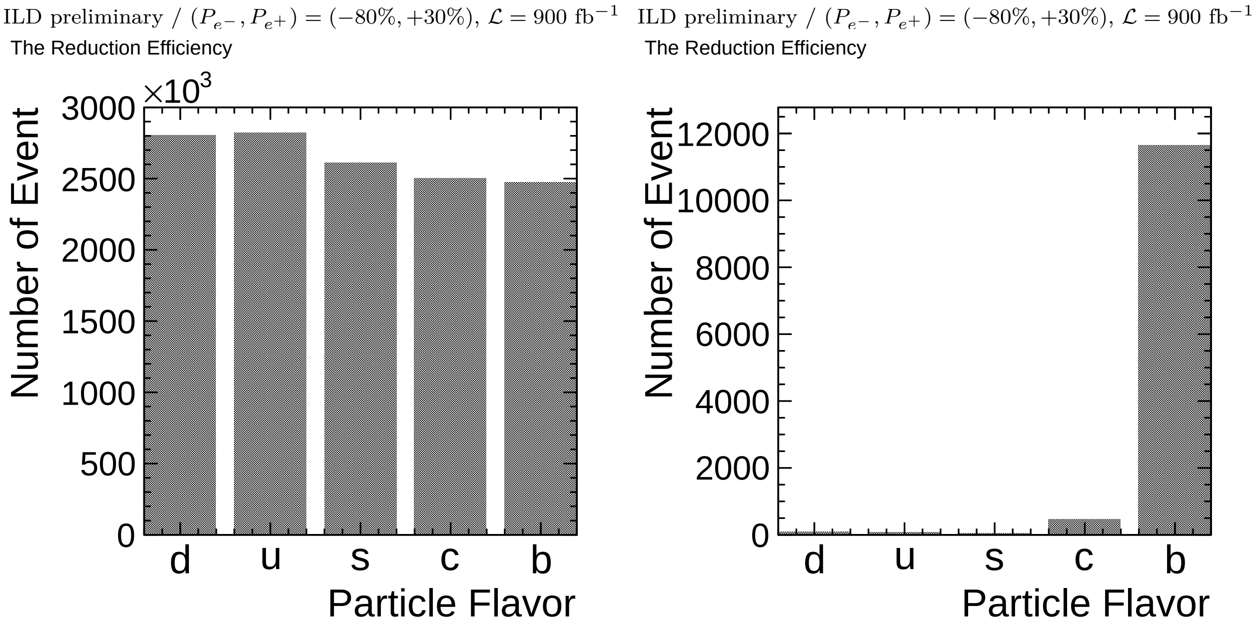

Figure 19: Reduction efficiency of particle of each flavor before cuts (left) and after cuts (right).

3.4.3 $h \to WW^*$ Semi-leptonic Channel

The signal events are characterised as having one monochromatic energetic photon with an energy of 93 GeV, one isolated electron or muon (we didn't study τ signal channel), two jets that are not b-tagged, and significant missing energy from the neutrino from leptonic W decay.

After the photon candidates have been identified, an isolated lepton algorithm is applied to find the signal electrons or muons using `isolatedLeptonTagging` processor as implemented in `iLCSoft`. Finally, the rest of the particles are clustered into two jets using the Durham jet clustering algorithm, and each is flavour tagged using `LCFI+`.

The number of charged particles in each event is required to be at least three. The b-likeness of both jets is required to be less than 0.77 to remove $h \to b\bar{b}$ events. The two jets are paired as one signal W boson (namely W_h), and the isolated lepton and missing four-momentum are paired as the other signal W boson (namely W_l). One of the two W bosons should be on-shell, with an invariant mass about 80.4 GeV, and one off-shell. We require $|m_{W_h} - 80.4| < 10$ GeV or $|m_{W_l} - 80.4| < 9.4$ GeV to select the on-shell W. Figure 20 and Figure 21 show the distributions of m_{W_h} and m_{W_l} for the signal and background events for both polarisations.

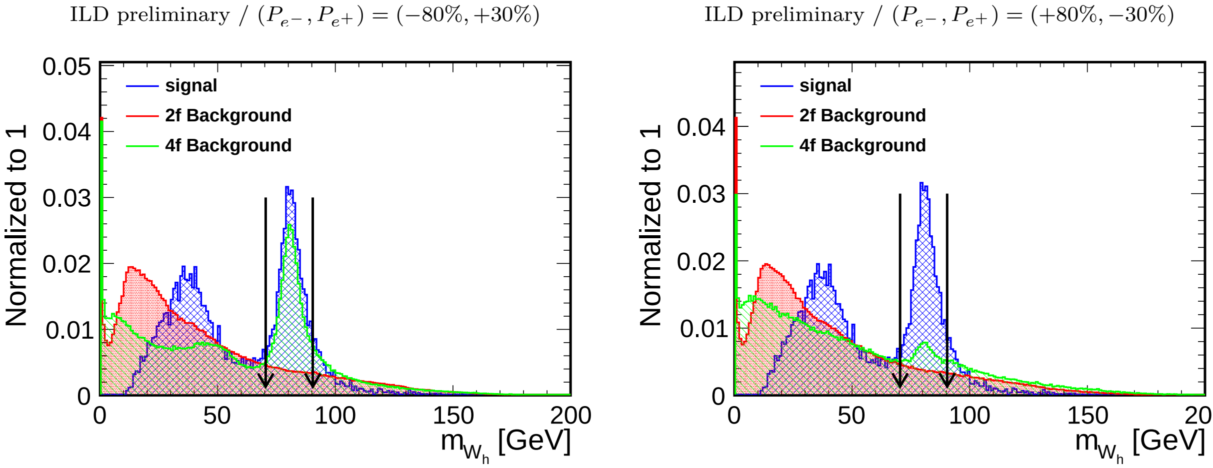

Figure 20: Distributions of the invariant mass of reconstructed W_h of the signal and background events: (left) $(P_{e^-}, P_{e^+}) = (-80\%, +30\%)$, (right) $(P_{e^-}, P_{e^+}) = (+80\%, -30\%)$. Arrows shows the applied cuts.

As with the $b\bar{b}$ channel, the remaining background events after these cuts are separated from the signal using a BDT multivariate analysis. In this analysis, the reconstructed higgs mass, missing energy, the energy of the photon, the total visible mass are the input variables as shown in Figure 22. We required the BDT output value (see Figure 23) for each event to be greater than 0.1.

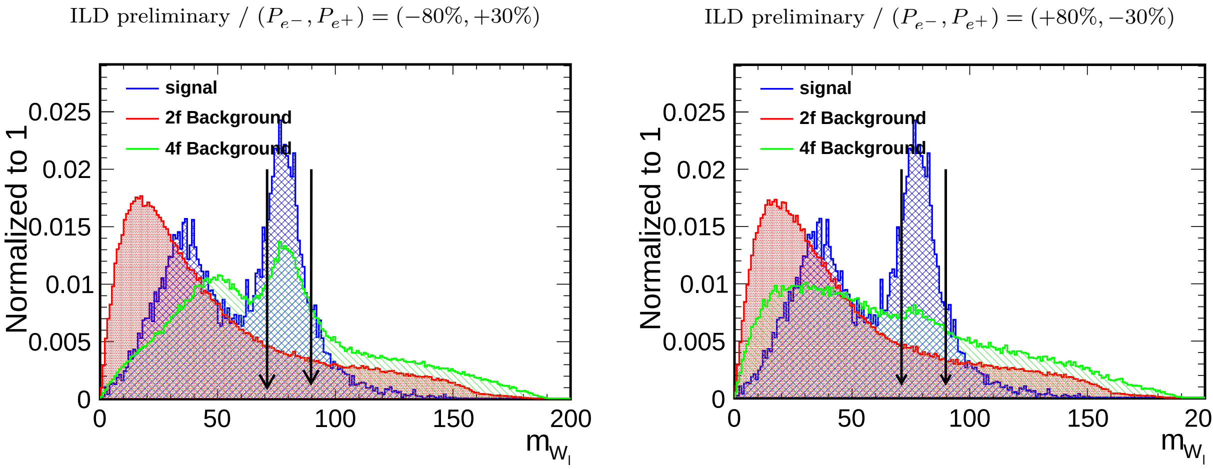

Figure 21: Distributions of the invariant mass of reconstructed W_l of the signal and background events: (left) $(P_{e^-}, P_{e^+}) = (-80\%, +30\%)$, (right) $(P_{e^-}, P_{e^+}) = (+80\%, -30\%)$

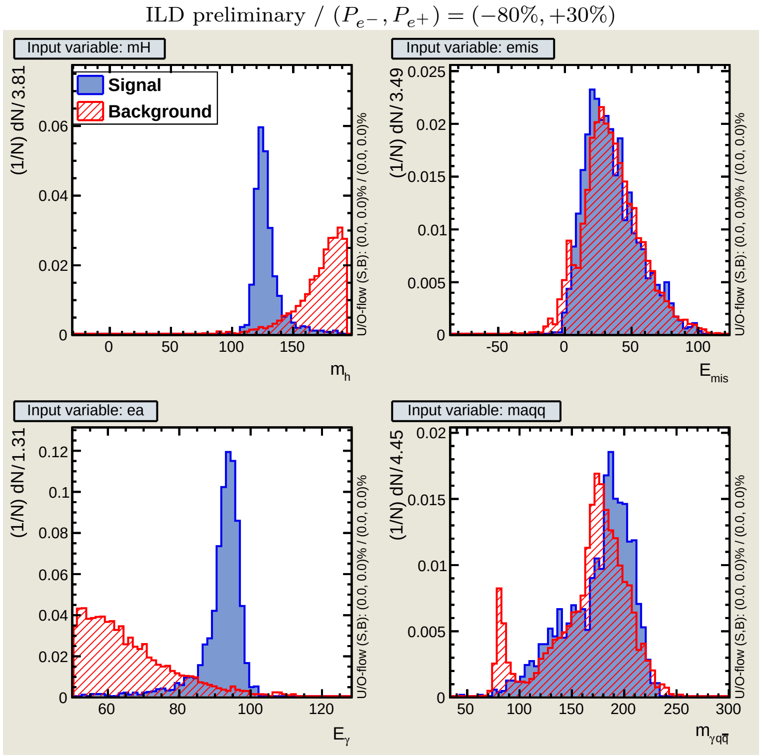

Figure 22: Signal and background distributions for each TMVA input for the $h \to WW^*$ (semi-leptonic) analysis. The blue histograms show the signal, and the red hatched histograms show the total background. Clockwise from top left: reconstructed Higgs mass, missing energy, total visible mass, and photon energy.

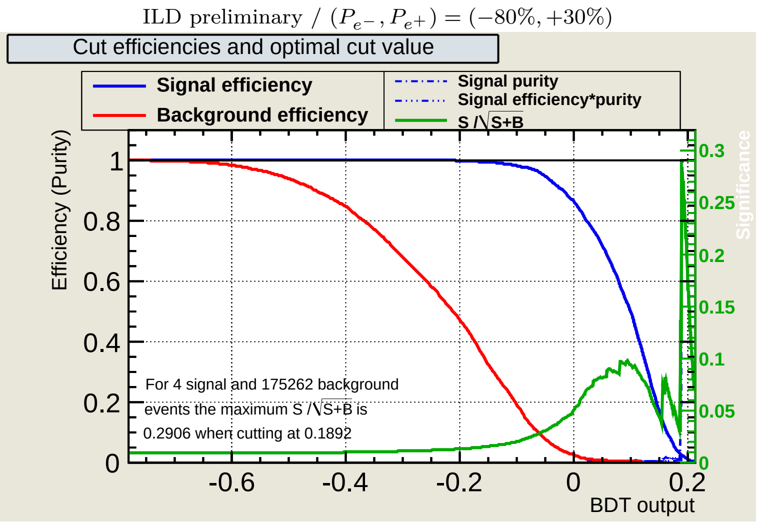

Figure 23: Cut efficiency as a function of MVA cut for the WW^* (semi-leptonic) analysis.

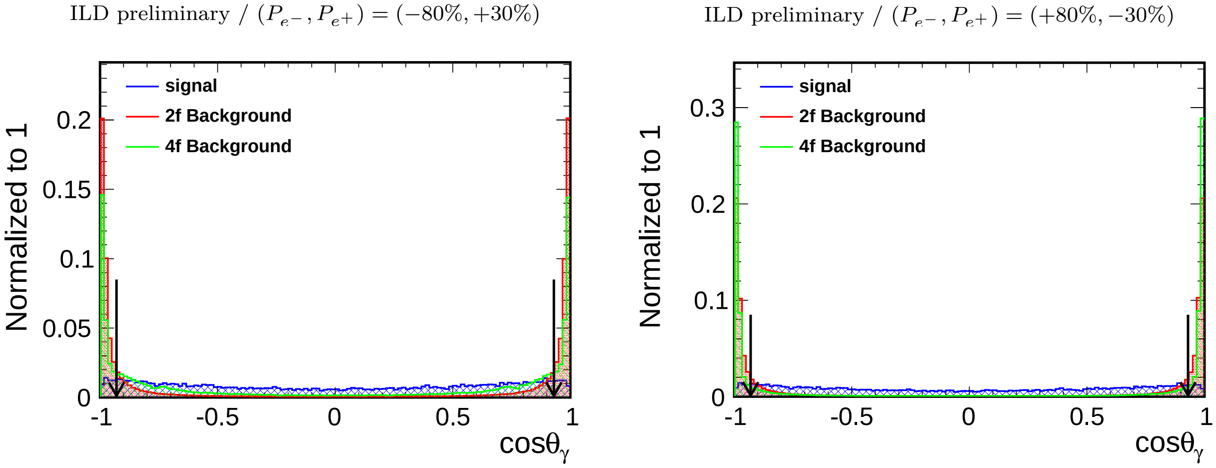

Figure 24: Distributions of the photon $\cos\theta$ for signal, $2f$, and $4f$ background in the WW^* channel: (left) $(P_{e^-}, P_{e^+}) = (-80\%, +30\%)$, (right) $(P_{e^-}, P_{e^+}) = (+80\%, -30\%)$.

Table 6 and Table 7 are the reduction tables for the two polarisation cases. The resulting signal significance is $3.1{\times}10^{-1}\sigma$ for $(P_{e^-}, P_{e^+}) = (-80\%, +30\%)$, and $4.2{\times}10^{-2}\sigma$ for $(P_{e^-}, P_{e^+}) = (+80\%, -30\%)$.

Table 6: Expected number of events in the $h \to WW^*$ semi-leptonic channel ($(P_{e^-}, P_{e^+}) = (-80\%, +30\%)$), after applying the selection cuts.

$(P_{e^-}, P_{e^+}) = (-80\%, +30\%)$, $\int \mathcal{L} = 900$ fb^{-1}, $\sqrt{s} = 250$ GeV

	2f	4f	total bg	Signal	Significance
Expected	1.0×10^8	3.7×10^7	1.4×10^8	1.8×10^1	3.4×10^{-3}
Pre selection	1.3×10^7	7.5×10^5	1.3×10^7	1.0×10^1	3.6×10^{-3}
# of charged particle>3	7.8×10^4	2.3×10^5	3.1×10^5	5.4	9.8×10^{-3}
$\lvert m_{W_h} - 80.4\rvert < 10$ GeV & $\lvert m_{W_l} - 80.4\rvert < 9.4$ GeV	2.5×10^4	1.6×10^5	1.9×10^5	3.7	8.6×10^{-3}
b likeliness< 0.77	1.7×10^4	1.6×10^5	1.8×10^5	3.7	8.7×10^{-3}
mvabdt > 0.1	3.1	3.8×10^1	4.1×10^1	1.0	1.6×10^{-1}
-0.93< $\cos\theta_\gamma$ <0.93	0.0	8.4	8.4	9.5×10^{-1}	3.1×10^{-1}

Table 7: Expected number of events in the $h \to WW^*$ semi-leptonic channel ($(P_{e^-}, P_{e^+}) = (+80\%, -30\%)$), after applying the selection cuts.

$(P_{e^-}, P_{e^+}) = (+80\%, -30\%)$, $\int \mathcal{L} = 900$ fb^{-1}, $\sqrt{s} = 250$ GeV

	2f	4f	total bg	Signal	Significance
Expected	7.3×10^7	4.6×10^6	7.8×10^7	1.9	4.8×10^{-4}
Pre selection	1.2×10^7	3.1×10^5	1.2×10^7	2.0	3.9×10^{-4}
# of charged particle > 3	5.0×10^4	3.6×10^4	8.6×10^4	1.5	1.9×10^{-3}
$\lvert m_{W_h} - 80.4\rvert < 10$ GeV & $\lvert m_{W_l} - 80.4\rvert < 9.4$ GeV	1.7×10^4	1.5×10^4	3.2×10^4	3.8×10^{-1}	2.1×10^{-3}
b likeliness< 0.77	1.2×10^4	1.4×10^4	2.6×10^5	3.7×10^{-1}	2.3×10^{-3}
mvabdt > 0.1	5.3×10^1	2.1×10^1	7.4×10^1	1.0×10^{-1}	1.2×10^{-2}
-0.93< $\cos\theta_\gamma$ < 0.93	0.0	4.7	4.7	9.3×10^{-2}	4.2×10^{-2}

The dominant background events are from $e^+e^- \to W^+W^-$ where one of the W bosons is on-shell, and one energetic photon is radiated from the initial states. This background is difficult to suppress because the reconstructed W mass completely overlaps with the signal as shown in Figure 20 and Figure 21. This background for the $(P_{e^-}, P_{e^+}) = (+80\%, -30\%)$ polarisation has a smaller peak around 80 GeV than $(P_{e^-}, P_{e^+}) = (-80\%, +30\%)$ polarisation because both the s-channel and t-channel of this reaction are suppressed in the $(P_{e^-}, P_{e^+}) = (-80\%, +30\%)$ case.

3.5 Result

3.5.1 95 % Confidence Level Upper Limit for the Cross Section of $e^+e^- \to h\gamma$

From the significance obtained, we put an 95% upper limit on the $e^+e^- \to h\gamma$ cross section using Equation 11 for each channel and polarisation as shown in Table 8.

$$\sigma_{h\gamma} = \sigma_{SM} + \frac{1.64}{\text{significance}} \sigma_{SM} \tag{11}$$

Table 8: Summary of the 95 % confidence level upper limit for the cross section of $e^+e^- \to h\gamma$.

Channel	Beam polarisation((P_{e^-}, P_{e^+}))	95% C.L. Upper limit [fb]
$h \to b\bar{b}$	$(-80\%, +30\%)$	$\sigma^-_{h\gamma} < 1.5$
$h \to b\bar{b}$	$(+80\%, -30\%)$	$\sigma^+_{h\gamma} < 0.9$
$h \to WW^*$ semi-leptonic	$(-80\%, +30\%)$	$\sigma^-_{h\gamma} < 1.3$
$h \to WW^*$ semi-leptonic	$(+80\%, -30\%)$	$\sigma^+_{h\gamma} < 0.8$

We combined the results of the two signal channels $h \to b\bar{b}$ and $h \to WW^* \to q\bar{q}l\nu (l = e, \mu)$, for each polarisation. The combined significance of these two channels is calculated by the square root of the sum of squares of significance for each channel. Using this combined significance, the combined 95% C.L. upper limits on the cross sections of the $e^+e^- \to h\gamma$ process are estimated. The results are as follows:

$$\sigma^-_{h\gamma} < 1.0 \text{ fb (95\% C.L.)} \tag{12}$$

$$\sigma^+_{h\gamma} < 0.6 \text{ fb (95\% C.L.).} \tag{13}$$

Normalising the SM cross section, these limits translate to

$$\frac{\sigma^-_{h\gamma}}{\sigma^-_{SM}} < 5.1 \text{ (95\% C.L.)} \tag{14}$$

$$\frac{\sigma^+_{h\gamma}}{\sigma^+_{SM}} < 28.3 \text{ (95\% C.L.),} \tag{15}$$

where we used $\sigma^-_{SM} = 0.20$ fb, and $\sigma^+_{SM} = 0.021$ fb.

We now convert these limits for the finite beam polarisations to limits for 100% beam polarisation values. The cross sections for the finite polarisations, $\sigma^-_{h\gamma}$ and $\sigma^+_{h\gamma}$, and those for the 100% polarisations, $\sigma^L_{h\gamma}$ and $\sigma^R_{h\gamma}$, are related by the following equation:

$$\begin{pmatrix} \sigma^-_{h\gamma} \\ \sigma^+_{h\gamma} \end{pmatrix} = \begin{pmatrix} \frac{1}{4}\left(1+|P_{e^-}|\right)\left(1+|P_{e^+}|\right) & \frac{1}{4}\left(1-|P_{e^-}|\right)\left(1-|P_{e^+}|\right) \\ \frac{1}{4}\left(1-|P_{e^-}|\right)\left(1-|P_{e^+}|\right) & \frac{1}{4}\left(1+|P_{e^-}|\right)\left(1+|P_{e^+}|\right) \end{pmatrix} \begin{pmatrix} \sigma^L_{h\gamma} \\ \sigma^R_{h\gamma} \end{pmatrix} \tag{16}$$

In the ILC case, $(|P_{e^-}|, |P_{e^+}|) = (80\%, 30\%)$. Therefore, the 100% polarisation values can be obtained by matrix inversion as

$$\begin{pmatrix} \sigma^L_{h\gamma} \\ \sigma^R_{h\gamma} \end{pmatrix} = \begin{pmatrix} 1.70 & -0.10 \\ -0.10 & 1.70 \end{pmatrix} \begin{pmatrix} \sigma^-_{h\gamma} \\ \sigma^+_{h\gamma} \end{pmatrix}. \tag{17}$$

Since the measurement of $\sigma^-_{h\gamma}$ is statistically independent of that of $\sigma^+_{h\gamma}$, the statistical errors on $\sigma^L_{h\gamma}$ and $\sigma^R_{h\gamma}$ are given by

$$\begin{aligned} \left(\Delta\sigma^L_{h\gamma}\right)^2 &= \left(\frac{\partial\sigma^L_{h\gamma}}{\partial\sigma^-_{h\gamma}}\Delta\sigma^-_{h\gamma}\right)^2 + \left(\frac{\partial\sigma^L_{h\gamma}}{\partial\sigma^+_{h\gamma}}\Delta\sigma^+_{h\gamma}\right)^2 \\ &= (1.70)^2\left(\Delta\sigma^-_{h\gamma}\right)^2 + (-0.10)^2\left(\Delta\sigma^+_{h\gamma}\right)^2 & (18) \\ \Delta\sigma^L_{h\gamma} &= 0.85 \text{ fb}, & (19) \end{aligned}$$

$$\begin{aligned} \left(\Delta\sigma^R_{h\gamma}\right)^2 &= \left(\frac{\partial\sigma^R}{\partial\sigma^-}\Delta\sigma^-\right)^2 + \left(\frac{\partial\sigma^R_{h\gamma}}{\partial\sigma^+}\Delta\sigma^+_{h\gamma}\right)^2 \\ &= (-0.10)^2\left(\Delta\sigma^-_{h\gamma}\right)^2 + (1.70)^2\left(\Delta\sigma^+_{h\gamma}\right)^2 & (20) \\ \Delta\sigma^R_{h\gamma} &= 0.60 \text{ fb}, & (21) \end{aligned}$$

where

$$\begin{aligned} \Delta\sigma^-_{h\gamma} &= \frac{\sigma^-_{SM}}{n^-_{sig}} = \frac{0.20 \text{ fb}}{0.40} = 0.5 \text{ fb} & (22) \\ \Delta\sigma^+_{h\gamma} &= \frac{\sigma^+_{SM}}{n^+_{sig}} = \frac{0.021 \text{ fb}}{0.06} = 0.35 \text{ fb}. & (23) \end{aligned}$$

We can then calculate the significance for $(P_{e^-},\ P_{e^+}) = (-100\%,\ +100\%)$, n^L_{sig}, and that for

$(P_{e^-}, P_{e^+}) = (+100\%, -100\%)$, $n^R_{\rm sig}$ as follows:

$$n^L_{\rm sig} = \frac{\sigma^L_{SM}}{\Delta\sigma^L_{h\gamma}} = \frac{0.35\ \text{fb}}{0.85\ \text{fb}} = 0.41 \tag{24}$$

$$n^R_{\rm sig} = \frac{\sigma^R_{SM}}{\Delta\sigma^R_{h\gamma}} = \frac{0.016\ \text{fb}}{0.60\ \text{fb}} = 0.027. \tag{25}$$

Finally the 95% confidence level upper limits for the 100% polarisations are given by

$$\sigma^L_{h\gamma} < \left(1 + \frac{1.64}{0.41}\right)\sigma^L_{SM} = 1.8\ \text{fb (95\% C.L.)} \tag{26}$$

$$\sigma^R_{h\gamma} < \left(1 + \frac{1.64}{0.027}\right)\sigma^R_{SM} = 0.99\ \text{fb (95\% C.L.)}, \tag{27}$$

or in units of the SM cross section:

$$\frac{\sigma^L_{h\gamma}}{\sigma^L_{SM}} < 5.0\ \text{(95\% C.L.)} \tag{28}$$

$$\frac{\sigma^R_{h\gamma}}{\sigma^R_{SM}} < 61.9\ \text{(95\% C.L.)}. \tag{29}$$

It turned out that the $e^+e^- \to h\gamma$ process is very difficult to observe at the ILC if there is no BSM contribution.

3.5.2 Monte-Carlo Uncertainty

In this section, we estimate the uncertainties due to limited Monte-Carlo statistics of background samples on the upper limits shown above. The uncertainty due to the signal MC statistics is negligible. The uncertainty due to the MC statistics of the dominant background in each channel can be rather large, because the weights of those events are as high as between 20 to 40. The large uncertainty appears mainly after the tight MVA and $\cos\theta_\gamma$ cuts. Thus we tried to re-estimate the efficiency of these cuts by appropriately loosening the cuts applied before the MVA and $\cos\theta_\gamma$ cuts to gain statistics.

We make a conservative estimate of the number of background event as follows. We define suppression ratios as follows

$$\text{MVA suppression ratio} = \frac{\text{\# of events when apply only MVA cut}}{\text{\# of events before all cuts}} \tag{30}$$

$$\cos\theta_\gamma\ \text{suppression ratio} = \frac{\text{\# of events when apply only } \cos\theta_\gamma \text{ cut}}{\text{\# of events before all cuts}} \tag{31}$$

Then we calculate conservative number of background.

$$\begin{aligned}\text{conservative \# of background} &= \text{\# of background just before MVA cut} \\ &\times \text{ MVA suppression ratio} \\ &\times \cos\theta_\gamma \text{ suppression ratio}\end{aligned} \tag{32}$$

This is, however, accurate only when the MVA cut is uncorrelated to the other cuts. We then take the difference between this re-estimated amount of background and that of the nominal background as a conservative estimation of the uncertainty due to MC statistics.

The results are summarised in Table 9, where the nominal and re-estimated (conservative) numbers of background events and corresponding significance values are compared. For the $b\bar{b}$ channel, the nominal and conservative cases are in perfect agreement. On the other hand, for the WW^* semi-leptonic channel, they differ by a factor of two. This discrepancy makes no difference in practice since the WW^* semi-leptonic result is not dominant in the combined result.

Table 9: Estimation of the uncertainty of the number of signal and background events due to limited MC statistics for $h \to b\bar{b}$ channel and $h \to WW^*$ semi-leptonic channel for $(P_{e^-}, P_{e^+}) = (-80\%, +30\%)$ and $(P_{e^-}, P_{e^+}) = (+80\%, -30\%)$ beam polarisations.

		Total background	Signal	Significance
$h \to b\bar{b}$	Nominal	12422	29	0.26
$(P_{e^-}, P_{e^+}) = (-80\%, +30\%)$	Conservative	13488	29	0.25
$h \to b\bar{b}$	Nominal	5946	3	0.04
$(P_{e^-}, P_{e^+}) = (+80\%, -30\%)$	Conservative	7204	3	0.04
$h \to WW^*$ (semi-leptonic)	Nominal	8	0.9	0.31
$(P_{e^-}, P_{e^+}) = (-80\%, +30\%)$	Conservative	92	0.9	0.09
$h \to WW^*$ (semi-leptonic)	Nominal	5	0.1	0.04
$(P_{e^-}, P_{e^+}) = (+80\%, -30\%)$	Conservative	21	0.1	0.02

3.5.3 Efficiency Uniformity

In general, BSM physics contributions can modify the $\cos\theta_\gamma$ distribution. We designed our selection cuts to obtain a selection efficiency as uniform as possible in the $\cos\theta_\gamma$ region in which we selected the signal events. As can be seen in Figure 25, the signal selection efficiency as a function of $\cos\theta_\gamma$ is flat. This facilitates the efficiency estimation in the presence of some BSM physics contributions.

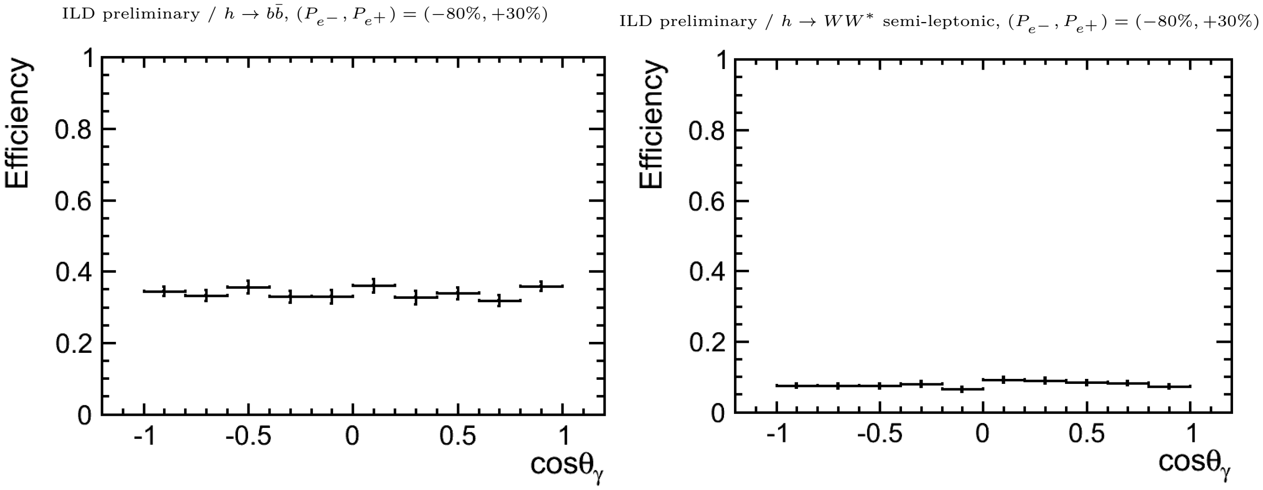

Figure 25: Selection efficiency as a function of $\cos\theta_\gamma$: (left) $h \to b\bar{b}$ channel, (right) $h \to WW^*$ (semi-leptonic) channel.

3.6 Interpretation of the Measurement

The analysis so far has allowed us to determine the upper limits on the cross sections for left- and right-handed beam polarisations. We will try to understand the role of this measurement in a model-independent EFT-based analysis, and for the Electron Yukawa coupling.

3.6.1 Constraint on $h\gamma Z$ Coupling

We use the EFT framework described in Section 2.2.1 to identify Lagrangian parameters that describe BSM effects. Equation 33 and Equation 34 [27] give the cross sections of $e^+e^- \to h\gamma$ (normalized by its SM value) in terms of ζ_{AZ} and ζ_A for 100% left- and right-handed polarisations, respectively:

$$\frac{\sigma^L_{h\gamma}}{\sigma^L_{SM}} = 1 - 201\zeta_A - 273\zeta_{AZ} \tag{33}$$

$$\frac{\sigma^R_{h\gamma}}{\sigma^R_{SM}} = 1 + 492\zeta_A - 311\zeta_{AZ}. \tag{34}$$

Using these formulae, we can constrain ζ_{AZ} from the upper limits on the cross section for $e^+e^- \to h\gamma$ for each polarisation and assuming that $\sigma_{h\gamma} > 0$. For the left-handed case, the constraint on the ζ_{AZ} was

$$5.0 \;>\; \frac{\sigma^L_{h\gamma}}{\sigma^L_{SM}} = 1 - 273\zeta_A - 201\zeta_{AZ} > 0 \tag{35}$$

$$\therefore -0.020 < \zeta_{AZ} < 0.005, \tag{36}$$

when we assume $\zeta_A = 0$ because ζ_A will be precisely constrained at HL-LHC. For the right handed case the constraint was,

$$61.9 > \frac{\sigma^R_{h\gamma}}{\sigma^R_{SM}} = 1 + 492\zeta_A - 311\zeta_{AZ} > 0 \tag{37}$$

$$\therefore -0.195 < \zeta_{AZ} < 0.003. \tag{38}$$

We now compare the constraints on the EFT coefficients with those from current LHC results and the HL-LHC projections as shown in Table 10. The LHC limit on $h \to \gamma\gamma$ is taken from the ATLAS experiment [28], and the LHC limit on $h \to \gamma Z$ from the CMS experiment [29]. These results provide 1σ limits for $\sigma \times BR(h \to \gamma\gamma)$ of 127 ± 10 fb and $\frac{BR(h\to Z\gamma)}{BR(h\to\gamma\gamma)}$ of $1.54^{+0.65}_{-0.58}$, thus we calculate the upper and lower values of these limits divided by its SM value $(\sigma \times BR(h \to \gamma\gamma))_{SM} = 116\pm$ 5 fb, and $\frac{BR(h\to Z\gamma)}{BR(h\to\gamma\gamma)}_{SM} = 0.69 \pm 0.04$. These include the SM cross-section, therefore, we should subtract one from observed values (details in appendix). We convert the HL-LHC projections from ATLAS experiment [30] [30] to the limits $-0.072 < 526\zeta_A < 0.076$ and $-0.46 < 290\zeta_{\mathrm{AZ}} < 0.51$ as shown in appendix.

Table 10: Current LHC limits and HL-LHC projections for ζ_{AZ} and ζ_A.

Process	Limitation
LHC limit ($h \to \gamma\gamma$) (Measured)	$0.92 < 1 + 526\zeta_{\mathrm{A}} < 1.27$ [28]
LHC limit ($h \to \gamma Z$) (Measured)	$0.55 < 1 + 290\zeta_{AZ} < 4.12$ [29]
HL-LHC limit ($h \to \gamma\gamma$) (Expected)	$-0.072 < 526\zeta_A < 0.076$ [30]
HL-LHC limit ($h \to \gamma Z$) (Expected)	$-0.46 < 290\zeta_{\mathrm{AZ}} < 0.51$ [30]

These results are shown in Figure 26. The blue and red areas show the limitation from our analysis at the $\sqrt{s} = 250$ GeV ILC with left- and right-handed case, respectively. The gray area shows the limitation from the LHC, and the black from the HL-LHC. Our result are inadequate to constrain ζ_A and ζ_{AZ} beyond the expected limits from HL-LHC. Unfortunately, our expected limits turned out to be rather weak.

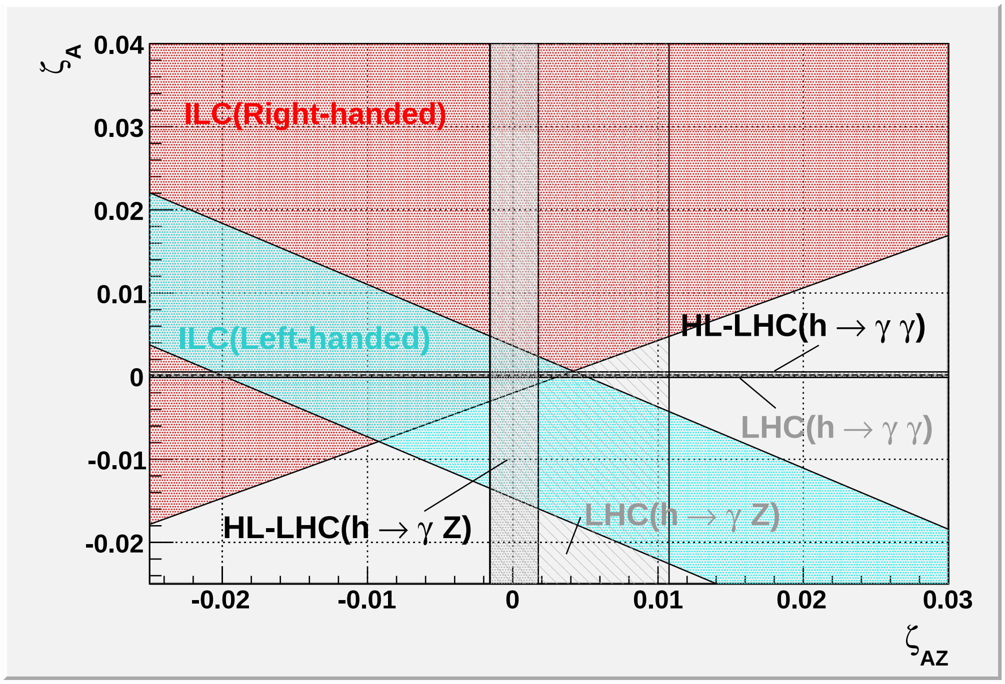

Figure 26: The blue and red areas show our left- and right-handed projected limits on ζ_A and ζ_{AZ} from our analysis at the $\sqrt{s} = 250$ GeV ILC, respectively. The gray and dark gray area shows the current limits from the LHC, and expectation from the HL-LHC.

Before we did this simulation, we naively expected that constraints on ζ_{AZ} and ζ_A would have been much stronger as shown in Figure 27 in the ideal case of no backgrounds and

100% signal efficiency using the $h \to b\bar{b}$ channel only. The backgrounds turned out to be overwhelming, and much more difficult to suppress as shown in Figure 28. Our full simulation showed that $e^+e^- \to h\gamma$ process is much more difficult to observe than naively expected.

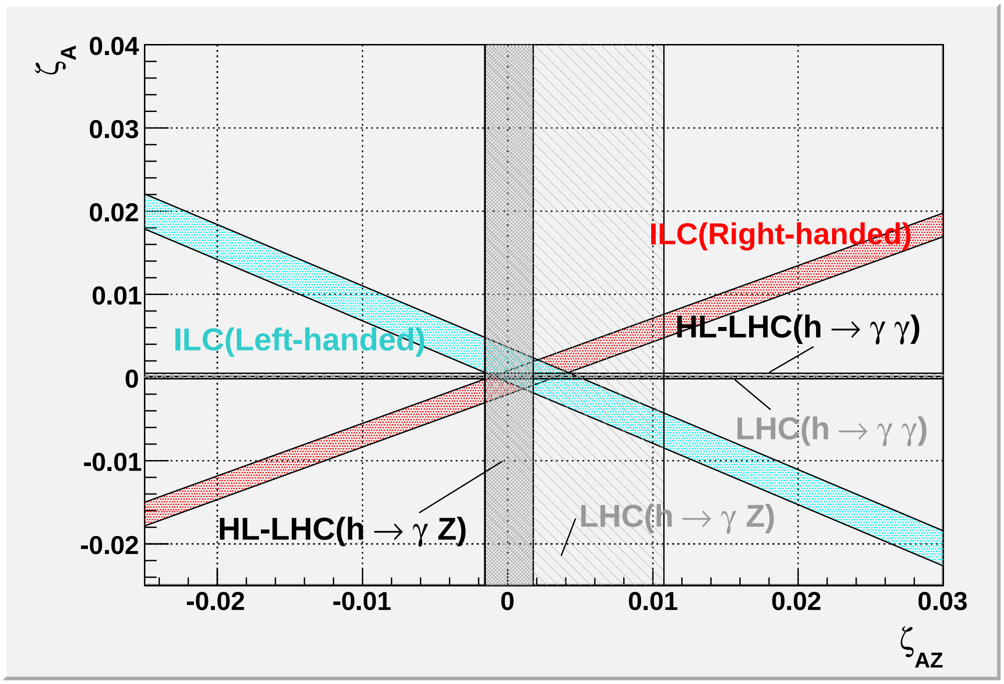

Figure 27: ILC limits on ζ_A and ζ_{AZ} limitation in the case of no experimented backgrounds and perfect selection efficiency.

ILD preliminary / $h \to b\bar{b}$, $(P_{e^-}, P_{e^+}) = (-80\%, +30\%), \int \mathcal{L} = 900$ fb^{-1}

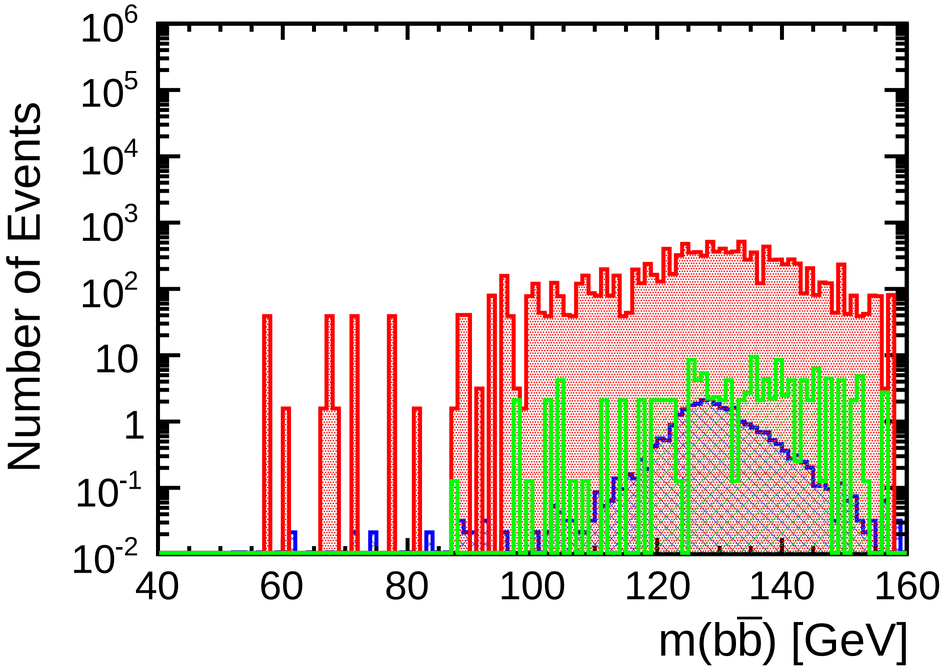

Figure 28: Number of event of signal and background after all cuts.

3.6.2 Constraint on Electron Yukawa Coupling

As shown in Figure 29, the electron Yukawa coupling can produce the same $h\gamma$ final state. This reaction can only occur with electrons and positrons have the same chirality combinations because the Higgs boson is spin 0. The differential cross section $\frac{d\sigma_{LL}}{d\cos\theta}$ and $\frac{d\sigma_{RR}}{d\cos\theta}$ is given by

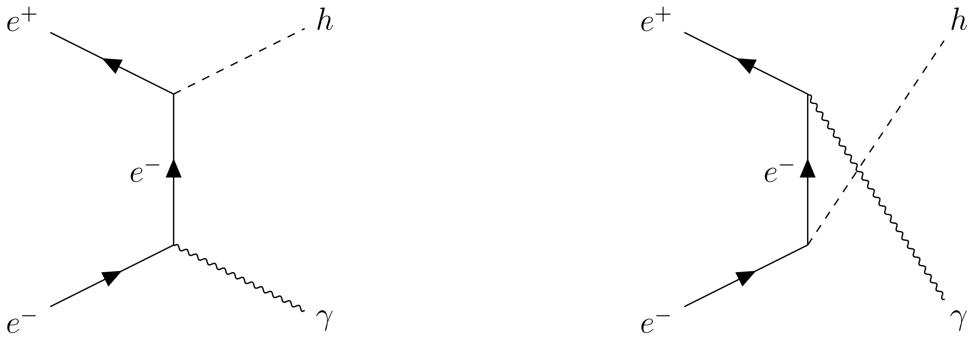

Figure 29: Feynman diagrams of $e^+e^- \to h\gamma$ via the Electron Yukawa coupling.

$$\frac{d\sigma_{LL}}{d\cos\theta} = \frac{d\sigma_{RR}}{d\cos\theta} = \frac{1}{2s\beta_e}2e^2\left(\frac{m_e}{v}\right)^2 D_tD_us^2\left[\left(1-\frac{m_h^2}{s}\right)^2 tuD_tD_u + 2\left(\frac{m_h^2}{s}\right)\right]\frac{\bar{\beta}}{16\pi}, \quad (39)$$

where D_t is $\frac{1}{q^2-m_e^2}$, D_u is $\frac{1}{r^2-m_e^2}$. Details of the calculation is shown in appendix. Plotting the cross section against $\cos\theta$, we get Figure 30. This result shows that the cross section is sharply peaking in the region where $|\cos\theta|$ is large. It is extremely difficult to detect the

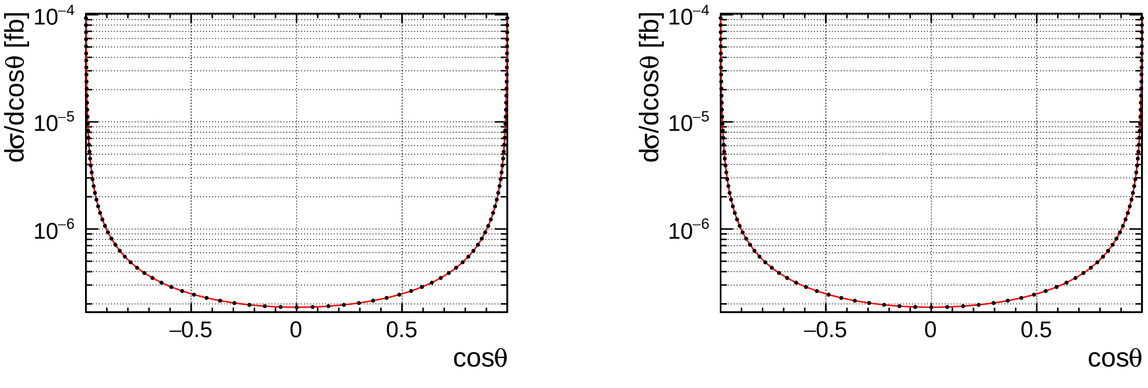

Figure 30: (Left) Differential $e^+e^- \to h\gamma$ cross section as a function of $\cos\theta$; ($P(e^-)$, $P(e^+)$)=(-80%, +30%), (Right) ($P(e^-)$, $P(e^+)$)=(+80%, -30%).

photon since it is often in the beampipe of the detector.

Since the measurement of the Electron Yukawa coupling turned out to be impossible in the SM case, we tried to estimate the 95% C.L. upper limit on it. We use (P_{e^-}, P_{e^+})=(-80%, -30%) and (P_{e^-}, P_{e^+})=(+80%, +30%) polarised portions in (P_{e^-}, P_{e^+})=(-80%, +30%) and (P_{e^-}, P_{e^+})=(+80%, -30%) polarisation cases, because we performed our simulation for only these two polarisation cases. Assuming all detected signal events come from the Electron Yukawa coupling, we can estimate the error of the cross section from the Electron Yukawa coupling as follows:

$$\frac{1}{(\Delta\sigma_y)^2} = \frac{1}{(\Delta\sigma^+)^2} + \frac{1}{(\Delta\sigma^-)^2} = \frac{1}{(0.29\text{ fb})^2}, \tag{40}$$

where $\Delta\sigma^+$ and $\Delta\sigma^-$ were given in Equation 23. Therefore, $\Delta\sigma_y = 0.29$ fb. Then the 95% C.L upper limit is $\sigma_y^{95} = 1.64 \times 0.29$ fb. The cross section from the Electron Yukawa coupling is $\sigma_{SM}^{L/R} = 3.6 \times 10^{-7}$ fb from the analytic calculation with $\cos\theta_\gamma$ cut $|\cos\theta| < 0.92$.

$$\frac{\sigma_y^{95}}{\sigma_y^{SM}} = \frac{1.64 \times 0.29}{3.6 \times 10^{-7}} = \left(\frac{y_e^{95}}{y_e^{SM}}\right)^2 \tag{41}$$

$$\frac{y_e^{95}}{y_e^{SM}} = 1.1 \times 10^3 \quad \text{(combined)} \tag{42}$$

The combined 95% C.L. upper limit on the Electron Yukawa coupling is therefore $\frac{y_e}{y_e^{SM}} < 1.1 \times 10^3$. This result is conservative because signal events contributed from the SM 1-loop process is not included. It should be added that combining the results of $(P_{e^-}, P_{e^+}) = (-80\%, -30\%)$ and $(P_{e^-}, P_{e^+}) = (+80\%, +30\%)$ polarisation cases may improve the results.

3.7 Summary of Part 1

We performed the world-first full simulation study of the $e^+e^- \to h\gamma$ process at the ILC, assuming a realistic ILD detector model to constrain SMEFT coefficients related to the $h\gamma Z$ coupling to determine the SMEFT Lagrangian. We generated the signal events using `Physsim` [17] and the 2f and 4f backgrounds using `Whizard` [18] at 250 GeV with 900 fb^{-1} for each of the following beam polarisation combinations: $(P_{e^-}, P_{e^+}) = (-80\%, +30\%)$ and $(P_{e^-}, P_{e^+}) = (+80\%, -30\%)$. The events simulated with `Geant4` [2] for the ILD DBD model [12] using `Mokka` [31] were fed into a full reconstruction chain from detector signals to reconstructed 4-vectors. `Marlin` in `iLCSoft` [20] was used for event reconstruction, where particle flow analysis (PFA) was performed with `PandoraPFA` [21] and flavor tagging with `LCFI+` [22]. The reconstructed events were analysed in the following two Higgs decay modes: $h \to b\bar{b}$, WW^* semi-leptonic. The signal significance was estimated after the event selection combining cut-based analysis and multi-variate analysis using TMVA. Signal significance of $h \to b\bar{b}$ is 0.26σ for $(P_{e^-}, P_{e^+}) = (-80\%, +30\%)$, $3.9\times10^{-2}\sigma$ for $(P_{e^-}, P_{e^+}) = (+80\%, -30\%)$, and of $h \to WW^*$ semi-leptonic channel is $3.1\times10^{-1}\sigma$ for $(P_{e^-}, P_{e^+}) = (-80\%, +30\%)$, $4.2\times10^{-2}\sigma$ for $(P_{e^-}, P_{e^+}) = (+80\%, -30\%)$. These results showed that the $e^+e^- \to h\gamma$ process is much more difficult to observe than naively expected. We, hence, estimated the upper limit on the signal cross section by combining the results for the $b\bar{b}$ and WW^* semi-leptonic channels. The expected upper limits were then estimated by combining $b\bar{b}$ and WW^* semi-leptonic channels for the two beam-polarisation combinations of $\frac{\sigma^-_{h\gamma}}{\sigma^-_{SM}} < 5.1$ (95% C.L.), and $\frac{\sigma^+_{h\gamma}}{\sigma^+_{SM}} < 28.3$ (95% C.L.), where we used $\sigma^-_{SM} = 0.20$ fb, and $\sigma^+_{SM} = 0.021$ fb, respectively.

In this part, we have shown the following.

1. The combined 95% C.L. upper limits on the $h\gamma$ production cross section for the SM are found to be $\frac{\sigma^L_{h\gamma}}{\sigma^L_{SM}} < 5.0$, and $\frac{\sigma^R_{h\gamma}}{\sigma^R_{SM}} < 61.9$ for purely left- and right-handed polarisations, respectively.

2. The upper limits constrain the EFT coefficient ζ_{AZ} as -0.020$< \zeta_{AZ} <$0.003.

3. The upper limits on the signal cross section can also be translated into a 95% C.L. upper limit to the electron-Yukawa coupling: $\frac{y_e}{y_e^{SM}} < 1.1 \times 10^3$.

Part 2

4 R&D for the ILD-TPC

4.1 Introduction & Motivation

A charged particle tracker with high momentum resolution is essential for precision Higgs measurements, particularly the cross section measurement using the recoil mass technique. The main tracker of the ILD is a Time Projection Chamber (TPC), and its momentum resolution goal is $\frac{\sigma_{P_T}}{P_T^2} = 1 \times 10^{-4}\ \mathrm{GeV}^{-1} \cdot c$. This momentum resolution goal requires 200 hit points with spatial resolution is better than 100 μm in the $r\phi$ direction (transverse) and 0.4-1.4 mm (for zero – full drift) in the z (longitudinal) direction over the full drift length. The end-plane readout modules that can achieve this spatial resolution goal are being developed.

An obstacle to achieving this performance has been the ion back-flow problem. This is caused by ions generated by ionisation in the amplification region of the ILD-TPC readout module. When the generated ions return to the drift region, they distort the electric field and deteriorate the spatial resolution. The idea of a gating device was conceived by F. Sauli in 2006 [32]. Sauli's idea was to use a GEM with a structure similar to that of a signal amplification GEM as a gate to stop the ions, however it was difficult to realise high electron transmission in this way. In collaboration with the FUJIKURA company, we have developed a new gating device which is very thin (25 μm) and has 80% optical aperture. We are now verifying that the end-plane readout module equipped with this gating device can achieve the required performance.

We carried out the world-first beam test of a prototype end-plane readout module with our gating device at DESY, which has a large prototype of ILD-TPC, and evaluated its performance in terms of spatial resolution. We report the beam test results of both $r\phi$ and z resolution and the extrapolation of the result to a full-size ILD-TPC. In the course of this study, we tested various methods of coordinate estimation and calibrations, details of which are also described.

4.2 TPC for the ILD

The TPC is a gas detector, which can reconstruct 3-dimensional tracks of charged particles. In the ILD, a TPC is used for the central tracker. Figure 31 shows a cross-sectional view of the ILD-TPC. The ILD-TPC has a cylindrical shape with a 1.8 m outer radius. It is divided by a cathode called a central membrane into two volumes about 2.2 m long, and has readout modules on each end-plane. The ILD-TPC is filled with the so-called T2K gas ($\mathrm{Ar} : \mathrm{CF}_4 : \text{iso-}\mathrm{C}_4\mathrm{H}_{10} = 95 : 3 : 2$). An electric field of 230 V/cm and magnetic field of 3.5 T are applied parallel to the cylinder axis. When charged particles enter the ILD-TPC, they ionise the gas molecules, and the ionised electrons drift along the applied electric field. Since the current generated by the ionised electrons is too weak to be recognised as a signal, they are gas-amplified and read out by the end-plane readout module. The charged particle trajectory is recorded as a projection of the ionised electrons on the end-plane ($r\phi$ plane) with an arrival time tag from which the z coordinate is estimated.

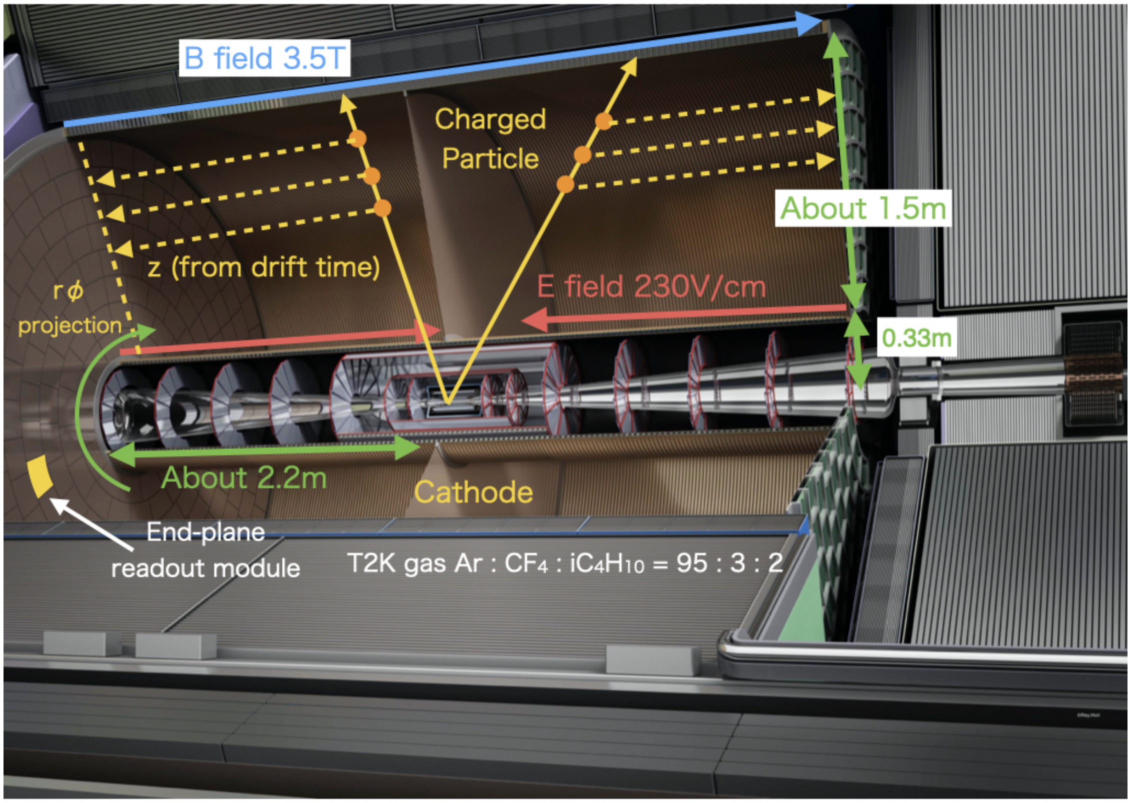

Figure 31: Principle of operation of ILD-TPC [11]©Rei.Hori/KEK.

4.3 Spatial Resolution Requirement for the ILD-TPC

The required asymptotic transverse momentum resolution at high P_T for the whole ILD is

$$\frac{\sigma_{P_T}}{P_T^2} = 2 \times 10^{-5}\ \mathrm{GeV}^{-1} \cdot c. \tag{43}$$

To achieve this goal together with the vertex detector and the internal and external silicon trackers, the following momentum resolution is required for the ILD-TPC:

$$\frac{\sigma_{P_T}}{P_T^2} = 1 \times 10^{-4}\ \mathrm{GeV}^{-1} \cdot c \tag{44}$$

at high P_T. The ILD-TPC measures momenta of charged particles from their trajectory curvatures caused by the magnetic field. According to Glückstern [33], the momentum resolution can be written in the form:

$$\frac{\sigma_{P_T}}{P_T} \simeq \sqrt{\left(\frac{\alpha' \sigma_x}{BL^2}\right)^2 \left(\frac{720}{n+4}\right) P_T^2 + \left(\frac{\alpha' C}{BL}\right)^2 \left(\frac{10}{7}\left(\frac{X}{X_0}\right)\right)} \tag{45}$$

where B is the magnetic field, L is the lever arm length, n is the number of measurement points, σ_x is the spatial resolution, α' is 333.56 $\mathrm{cm} \cdot \mathrm{T} \cdot \mathrm{GeV}^{-1}$, C is 14.1 MeV, and $\frac{X}{X_0}$ is the gas thickness that the track passes through measured in radiation length units. Therefore, the momentum resolution depends on magnetic field B, the lever arm length L, the number of measurement points n, and the spatial resolution σ_x. Especially, the spatial resolution is important because other parameters are almost fixed. Substituting the ILD-TPC numbers to Glückstern's formula: the magnetic field B of 3.5 T, the track detection length L of 1.5 m, and 200 measurement points, we find that the $r\phi$ (transverse section to beam line) spatial resolution should be better than 100 μm over the full drift length 2.2 m. The high z resolution of 0.4-1.4 mm for zero to full drift length is required to estimate the longitudinal momentum from P_T.

4.4 Experimental Apparatus

4.4.1 End-Plane Readout Module

End-plane readout modules are being developed to achieve the requirements. The LCTPC Asia group is developing an end-plane readout module with a double stack of gas electron multipliers (GEM) as an amplification device ("Asian module") as shown in Figure 32. The module is made by stacking a pad plane as the anode, two amplification GEMs, and a gating device. When we took data without the gating device, we used a field shaper. In what follows, we will explain more about each part of the Asian module.

Anode (Pad Plane) The anode (pad plane) carries many small readout pads on a PC board, where avalanche electrons are collected as signals. On the other side of the PC board, there are many small connectors to attach readout cables. The pad plane used in this study has 5152 pads, each of which is about 1.2 mm wide and 5.26 mm long, as shown in Figure 33. These pads are arranged in 28 pad rows.

Amplification GEM The GEM is a 100 μm thick sheet of insulating polyimide sandwiched by copper electrodes as shown in Figure 34, which amplifies electrons to a readable charge amplitude. The GEM sheet has evenly spaced 70 μm diameter holes with 140 μm

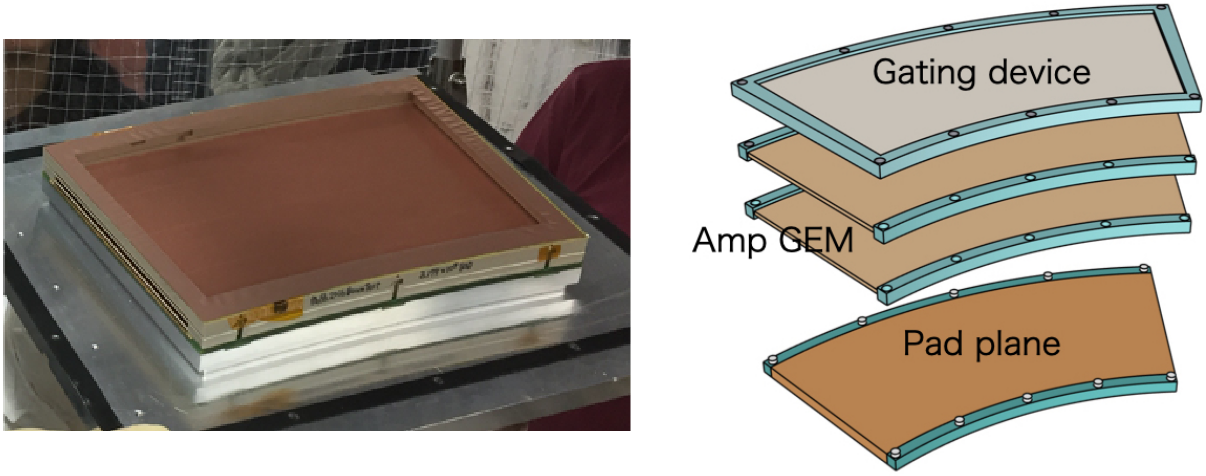

Figure 32: (left) Appearance of the module, (right) Structure of the Asian module.

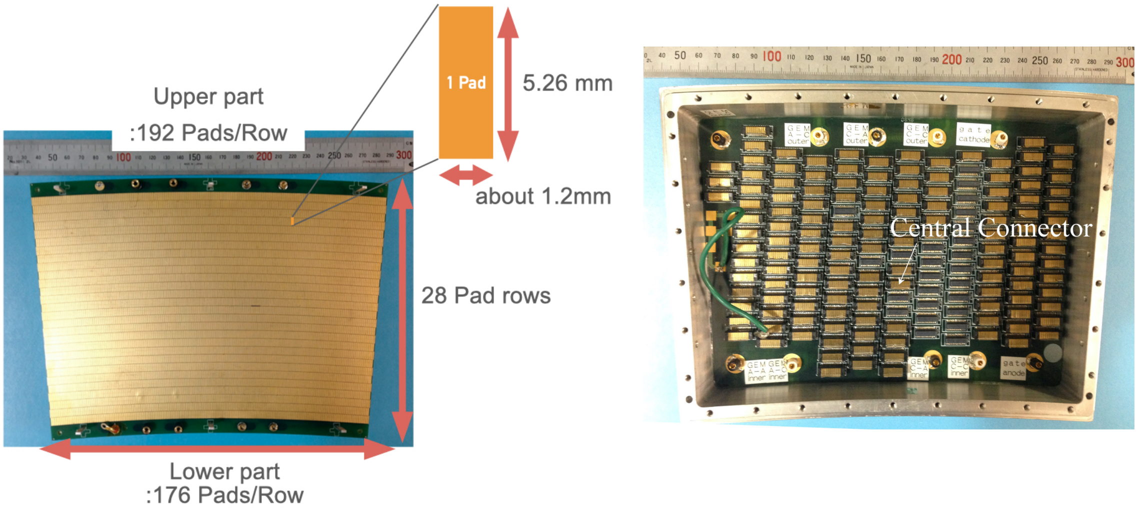

Figure 33: (left) Front of the pad plane. (right) Readout of pad plane (based on [34]).

pitch as shown in Figure 35, and inside these holes amplifies the seed electrons by creating an avalanche of electrons. Figure 36 shows an example of electric field lines in GEM holes. The avalanche electrons have a sufficient spread of a few hundred microns to apply the centre-of-gravity method when read out with readout anode pads of about 1 mm pitch. The electrode not facing the drift volume of the amplification GEM is divided into four segments to protect the GEM foil against possible discharge. There are hence three gaps.

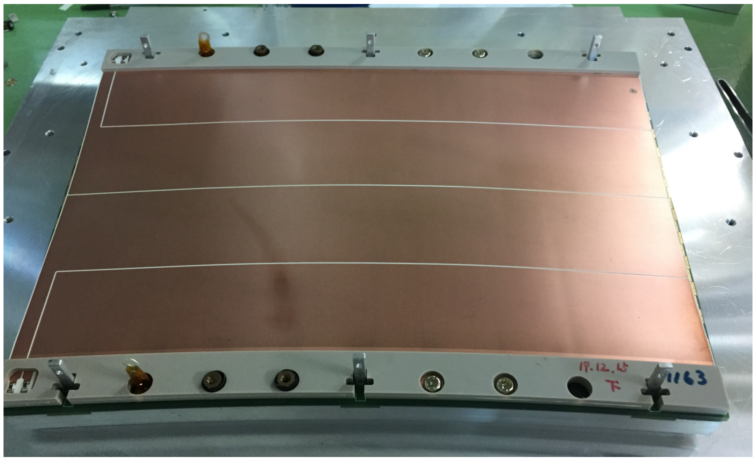

Figure 34: Amplification GEM.

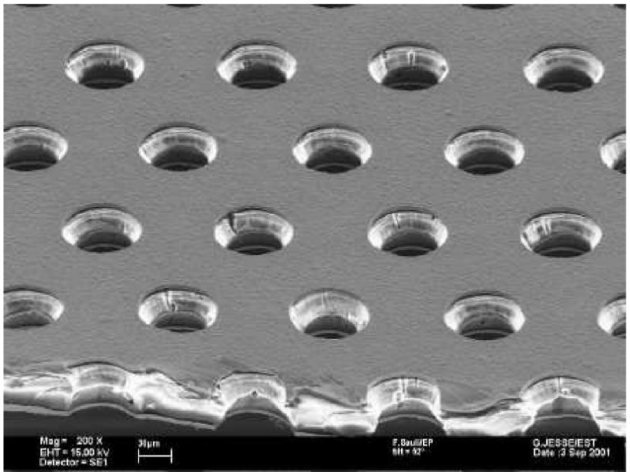

Figure 35: Enlarged photograph of an amplification GEM [35].

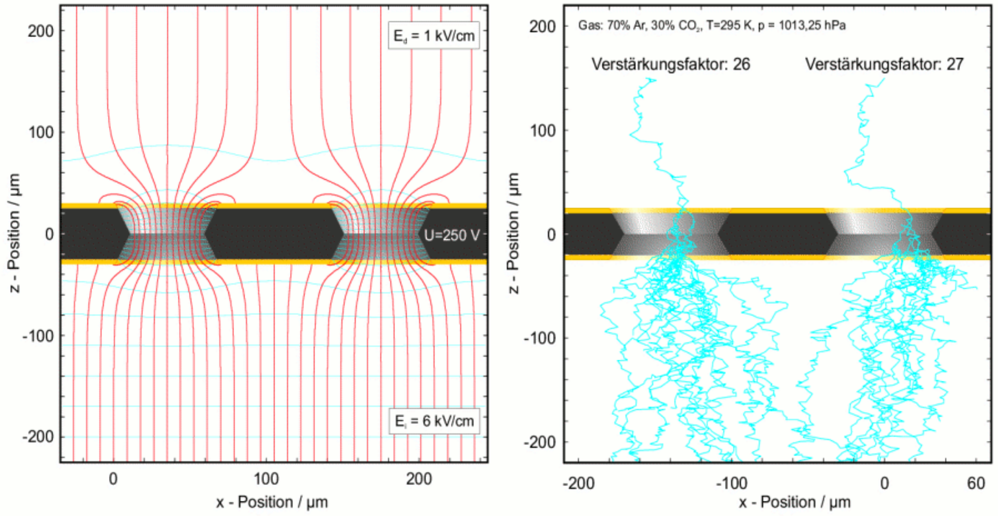

Figure 36: Electric field line of GEM (left), and avalanche creation in the GEM holes (right). [35]

4.4.2 Gas Mixture

We need a gas mixture that minimises electron diffusion in the drift region and provides sufficient gas gain in the amplification region. We chose the so-called T2K gas ($\mathrm{Ar} : \mathrm{CF}_4 : \text{iso-}\mathrm{C}_4\mathrm{H}_{10} = 95 : 3 : 2$) for the ILD-TPC. Argon gas is often used as a base chamber gas because it has a valley structure, which is called a Ramsauer dip, in the electron Argon cross section as shown in Figure 37. The dip allows electrons to relatively easily gain high enough energy to ionise gas molecules in a high electric field thereby providing high gas gain.

The transverse diffusion constant C_{dT} depends on the magnetic field as

$$C_{dT}(B) \approx \frac{C_{dT}(0)}{\sqrt{1+(\omega\tau)^2}}, \tag{46}$$

where $\omega = eB/m_e$ is the cyclotron frequency and τ is the electron mean free time. Near the cross section minimum, the electron mean free time becomes large and hence the transverse diffusion becomes small. CF_4 keeps the electron energy around the Ramsauer dip because the cross section for CF_4 has a wall around the Ramsauer dip as shown in Figure 37.

Both CF_4 and iso-$\mathrm{C}_4\mathrm{H}_{10}$ work as a quencher to absorb ultraviolet photons emitted by the de-excitation of Argon molecules. iso-$\mathrm{C}_4\mathrm{H}_{10}$ also contributes to the gas gain because it has the penning effect: when an excited Argon scatters off an iso-$\mathrm{C}_4\mathrm{H}_{10}$, the iso-$\mathrm{C}_4\mathrm{H}_{10}$ emits an electron. This is because the minimum ionisation energy of iso-$\mathrm{C}_4\mathrm{H}_{10}$ is smaller than the excitation energy of Argon.

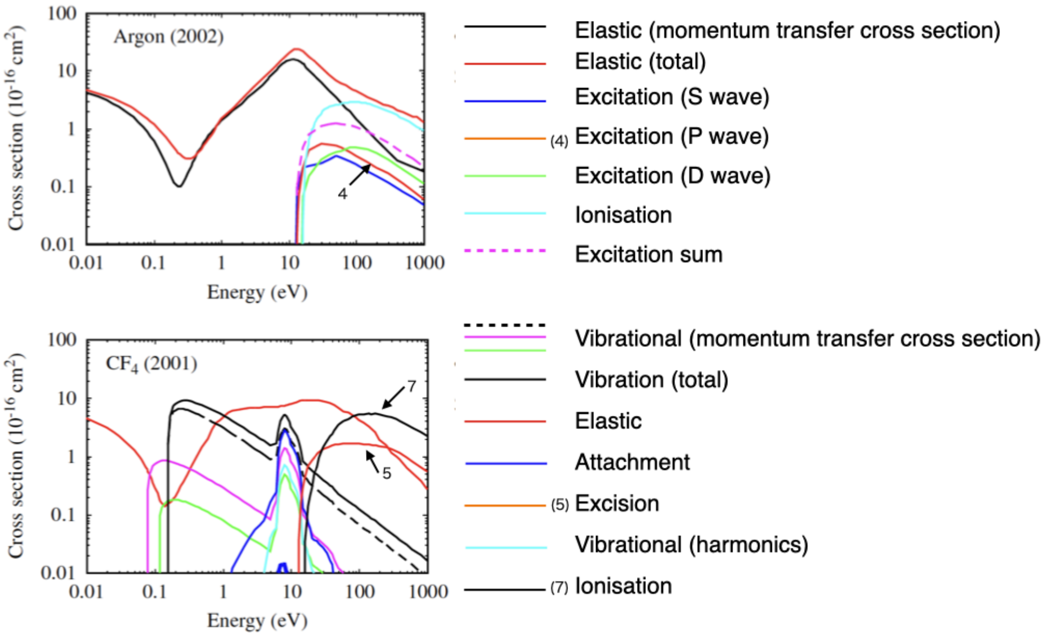

Figure 37: Electron molecule cross sections as a function of the electron energy for Argon and CF$_4$ [34]. The detail explanation of different color lines is in [36].

4.5 Ion Back-Flow Problem

The potential problem that stands in the way of achieving the resolution goal is positive ion back-flow. When many positive ions created by gas amplification back-flow into the drift volume, they distort the electric field and deteriorate the spatial resolution. As we explain in the introduction, the ILC has a bunch train every 200 ms. The ions a single ILC bunch train form an ion disk with about 1 cm thickness in the ILD-TPC. Since the ion drift velocity is O(1000) times slower than that of electrons, there will be up to three ion disks in the drift volume. Hit point distortion due to the three ion disks is estimated to be 60 μm [12], therefore this effect can not be ignored to achieve our $r\phi$ spatial resolution of 100 μm.

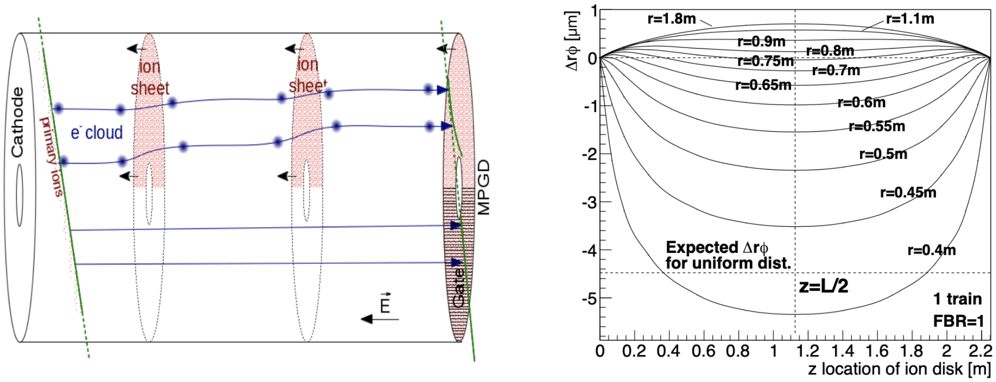

Figure 38: (Left) Distortion of electric field lines caused by ion disks. (Right) Estimated deterioration in $r\phi$ resolution caused by back-flow ions [12].

4.5.1 Gating Device

To solve the ion back-flow problem, we developed a large aperture gating device with the FUJIKURA company. We call it the "gating device" hereafter. It is like a GEM foil, but is only about 25 μm thick, and has much bigger holes about 300 μm wide in a honeycomb structure, as shown Figure 40. The optical aperture of the gating device is about 80%. The gating device can be opened or closed by changing the voltage applied to the copper electrodes. Figure 41 shows the electric field lines when the gating device is closed (right). We open the gate before the bunch train arrival and close the gate after it has passed.

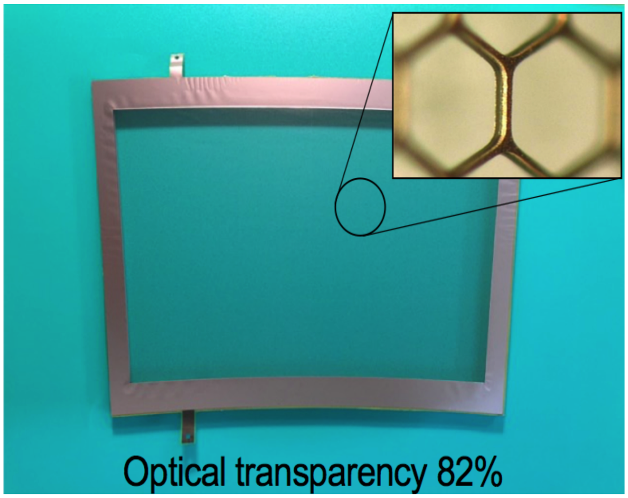

Figure 39: Photograph of the gating device.

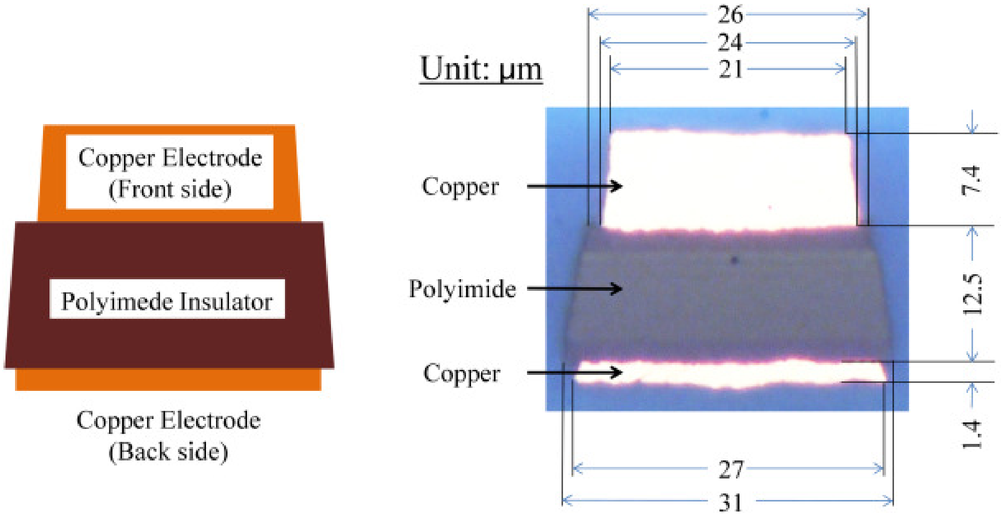

Figure 40: Cross-section of the gating device [37].

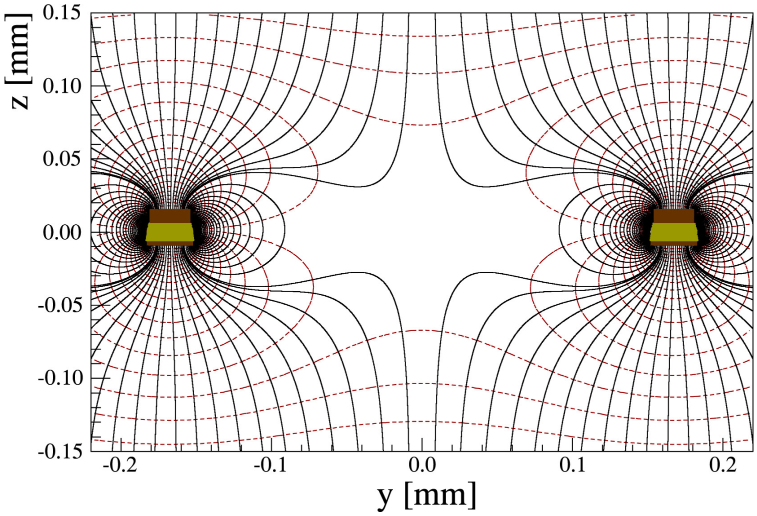

Figure 41: Gating device electric lines when the gate is closed [37].

4.6 Previous Study Without Gating Device

The ILD-TPC end-plane readout module without gating device was studied in [3]. This study developed a full analytic formula for the $r\phi$ resolution $\sigma_{r\phi}$, which can be written in the following form, when electronic noise effect is negligible

$$\sigma_{r\phi}^2 = A(z) + \frac{C_{dT}^2 z}{N_{eff}}, \tag{47}$$

where z is the drift length, N_{eff} is the effective number of electrons, and C_{dT} is the transverse diffusion constant that depends on the magnetic field B. N_{eff} is given by

$$\frac{1}{N_{eff}} = \left\langle \frac{1}{N} \right\rangle_N \left\langle \left(\frac{G}{\bar{G}} \right)^2 \right\rangle_G, \tag{48}$$

where N is the number of seed electrons, G is the gas gain for a single seed electron, and $\bar{G}$ is the average gas gain. $A(z)$ represents the so-called hodoscope effect,[1] while the second term corresponds to the diffusion effect. A schematic image of this formula is shown in Figure 43. The detailed explanation of each term is given in [3]. The asymptotic analytic formula at long drift distance can be written in the form:

$$\sigma_{r\phi}(z)^2 \simeq \sigma_0^2 + \frac{1}{N_{eff}} C_{dT}^2 z, \tag{49}$$

where σ_0 is given by $\frac{A(0)}{N_{eff}}$. This formula works in the sufficiently long drift distance region $C_{dT}\sqrt{z}/w > 0.4$, where w is the pad pitch. This formula can be also written as

$$\sigma_{r\phi}(z)^2 = \frac{1}{N_{eff}} \left(A(0) + C_{dT}^2 z \right). \tag{50}$$

$(A(0) + C_{dT}^2 z)$ represents the coordinate error for a single seed electron, namely, the accuracy of coordinate information provided by a single electron. On average we have N_{eff} seed electrons providing the same original hit point coordinate information. Equation 50 exactly shows the position resolution for N_{eff} independent measurements.

This previous study concluded that the performance goal of $\sigma_{r\phi} < 100$ μm over the

---

[1] At a short distance, the transverse diffusion of electrons is small. The hit point is determined using the centre-of-gravity method, but the signal electrons arrive at only one pad in the worst case. This is called the hodoscope effect. In general, when the charge diffusion is small and the number of pads with signals is small, the hit coordinate calculated with the centre-of-gravity method is biased (the so-called S-shape systematics) and hence the spatial resolution becomes worse than when the charge diffusion is large enough to spread over several pads.

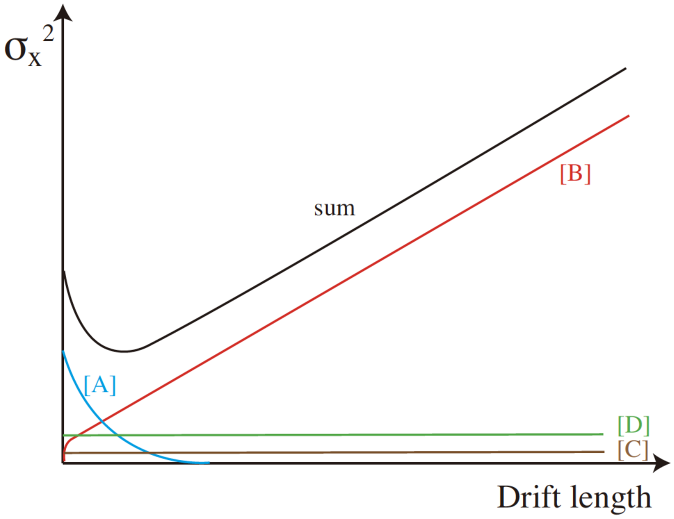

Figure 42: Terms [A], [B], [C], and [D] are the short drift distance effect, the diffusion effect, the electric noise effect, and the angular pad effect, respectively. [D] term vanishes for tracks perpendicular to pad rows. Details can be found in [3].

full 2.2 m drift length of the ILD-TPC can be achieved with an end-plane readout module without the gating device.

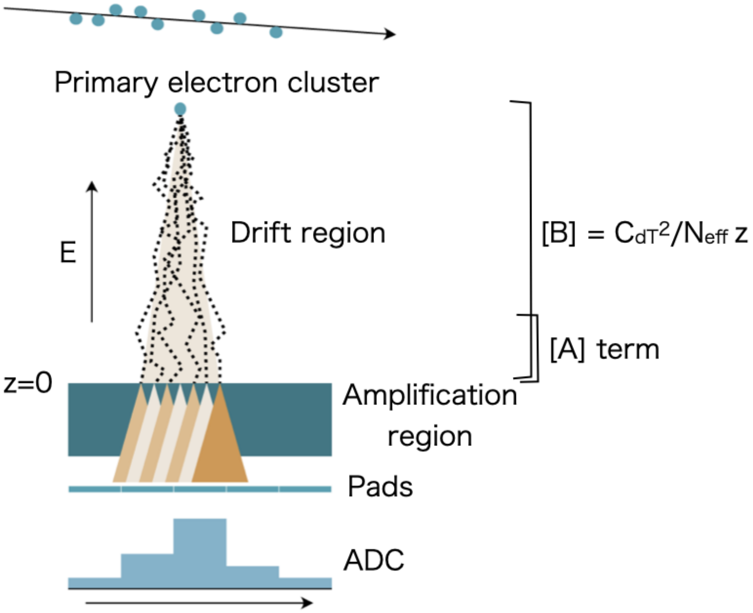

Figure 43: Schematic image of electron diffusion.

4.7 DESY Beam Test Facility and ILD-TPC Large Prototype

For the experiments, we used a 5 GeV electron test beam at DESY in Germany. The ILD-TPC large prototype is installed there, and data can be acquired under a magnetic field of 1 T. The data acquisition was carried out from October 31 to November 14, 2016.

Figure 44 is the schematic view from above of the DESY test facility. DESY has three test beam lines (T21, T22 and T24) and the large prototype of the ILD-TPC is installed in the T24/1 beam line. The 1 GeV to 6 GeV test beam is provided at 10 Hz [38]. The electron beam passes two trigger counters and through the prototype as shown in Figure 45. The sensitive volume of the large prototype is inside a solenoid magnet that can apply 1 T. The whole system is mounted on a movable stage so we can change drift length z and two angles θ and ϕ.

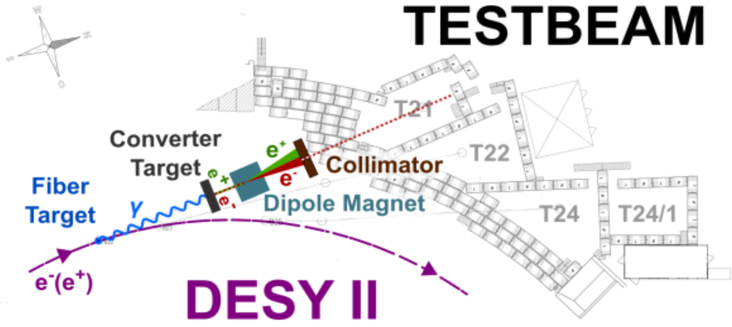

Figure 44: DESY test facility [39].

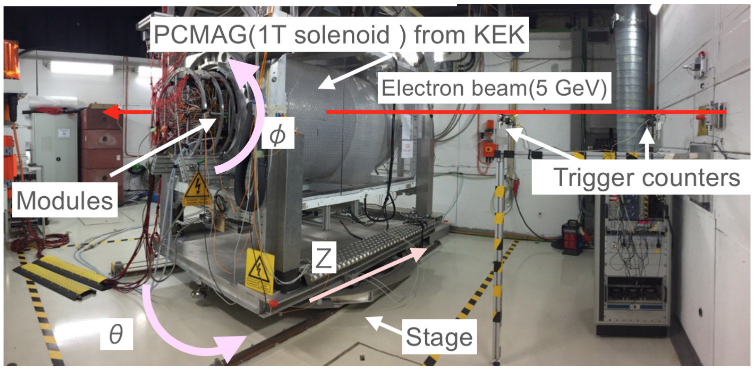

Figure 45: Large prototype: LP1.

4.7.1 Readout Electronics

Figure 46 sketches the structure of the readout system. After arriving at the anode, the signal charge amplified by the electronic avalanche is sent to the front-end electronics through a 25 cm readout Kapton cable. The front-end electronics is composed of the following components: four Kapton cables are connected to a protection card to prevent circuit breakdown due to electrical discharge, and the Front-End Card (FEC) is attached to each protection card. The FEC contains eight Pre-Amplifier-Shaper-Amplifier (PASA) and eight ALICE TPC Read Out (ALTRO) chips. The PASA chip called PCA16 has 16 channels. Each channel consists of a pre-amplifier followed by a unipolar shaper that shapes the delta function current input into a semi-Gaussian form. As parameters, we can choose the peaking time (30, 60, 90, 120 ns), amplification factor (12, 15, 19, 27 mV/fC), delay time, and signal polarity. The peaking time is the time input needed for a pulse to reach its peak height. We use a peaking time of 120 ns and amplification factor of 12 mV/fC in this study. The ALTRO chip is responsible for the time-to-time digital conversion of the electric signal; it has 16 channels, each of which has a 10-bit flash ADC. The FEC is bus-connected at the opposite end from the input, and its readout is controlled by a Readout Control Unit (RCU). A single RCU can control a maximum of 32 FECs. The data is then sent via optical fibre cables to the Data ReadOut Receiver Card (DRORC) installed on the computer.

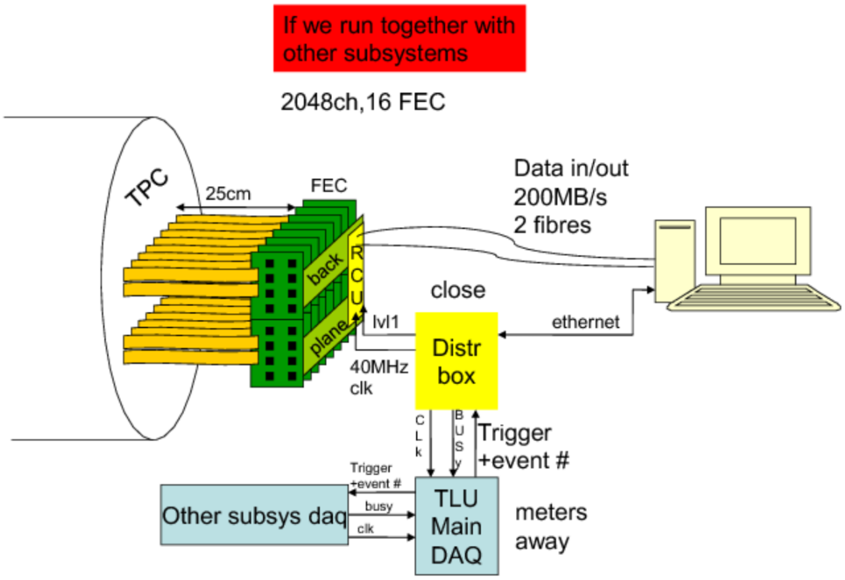

Figure 46: Schematic image of the readout system of the ILD-TPC large prototype. [40]

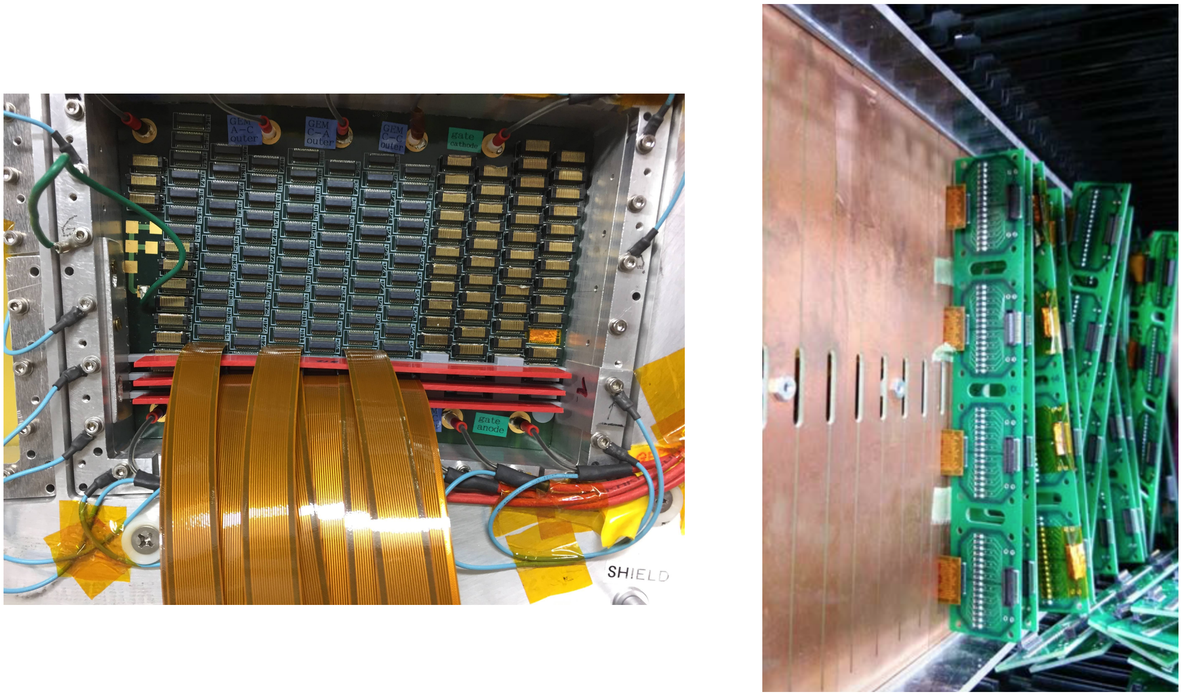

Figure 47: (left) Kapton cables inserted into the pad planes. (Right) Other end of the Kapton cables which are fixed to protection cards.

Figure 48: Picture of the FEC. The Left four chips are ALTRO chips, and right four are PASA chips.

4.7.2 Data Taking

We took data with a prototype of Asian module with and without the gating device at various drift lengths, angles, gating device voltages, and magnetic field as shown in Table 11. The voltage setting of the GEMs and ILD-TPC are summarised in Table 12 and Figure 49. As shown in Figure 50, 230 V/cm result fast drift velocity and small transverse diffusion.

Table 11: Data taking conditions

Center module	With gating device, Without gating device
z[cm](drift length)	2.5, 5.0, 7.5, 10, 12.5, 15, 20, 25, 30, 35, 40, 45, 50, 55
ϕ[degree]	-10, 0 ,10 ,20
θ[degree]	0, 10, 20
B(Magnetic field)[T]	1, 0
Beam	5 GeV electron beam
Gas	T2K gas ($Ar : CF_4 : iC_4H_{10} = 95 : 3 : 2$)
Software Framework	`MarlinTPC` (20000event/1 run)

Table 12: Voltage setting of GEMs, and electric fields in the different region.

Gating GEM [V]	3.55, -3.55
GEM 1 [V]	355
GEM 2 [V]	315
Drift region [V/cm]	230
Transfer region [V/cm]	887.5
Induction region [V/cm]	2700

The concentration of O_2, H_2O, and the temperature and pressure inside the ILD-TPC prototype and atmospheric pressure in the experimental hall were recorded through out the data taking using a monitoring system.

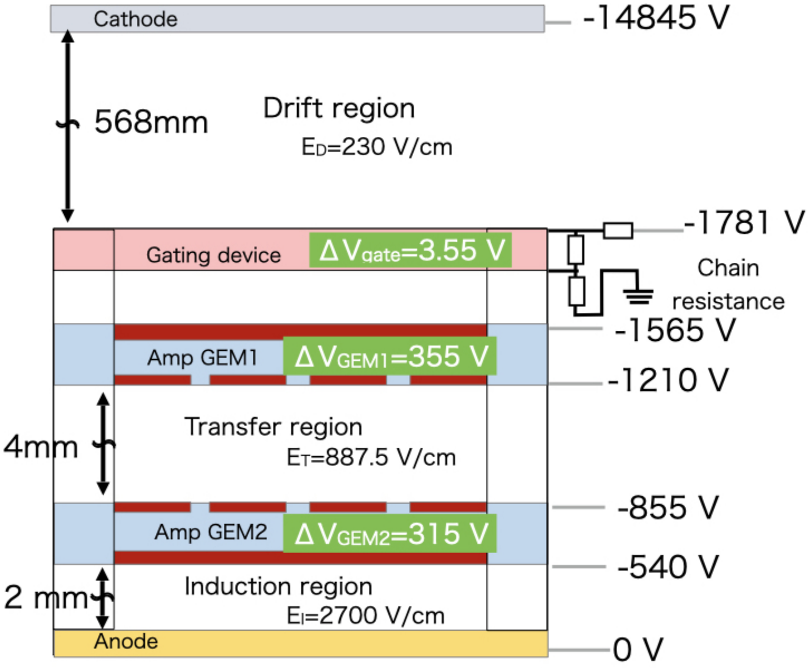

Figure 49: Voltages applied to the module (gating device is open).

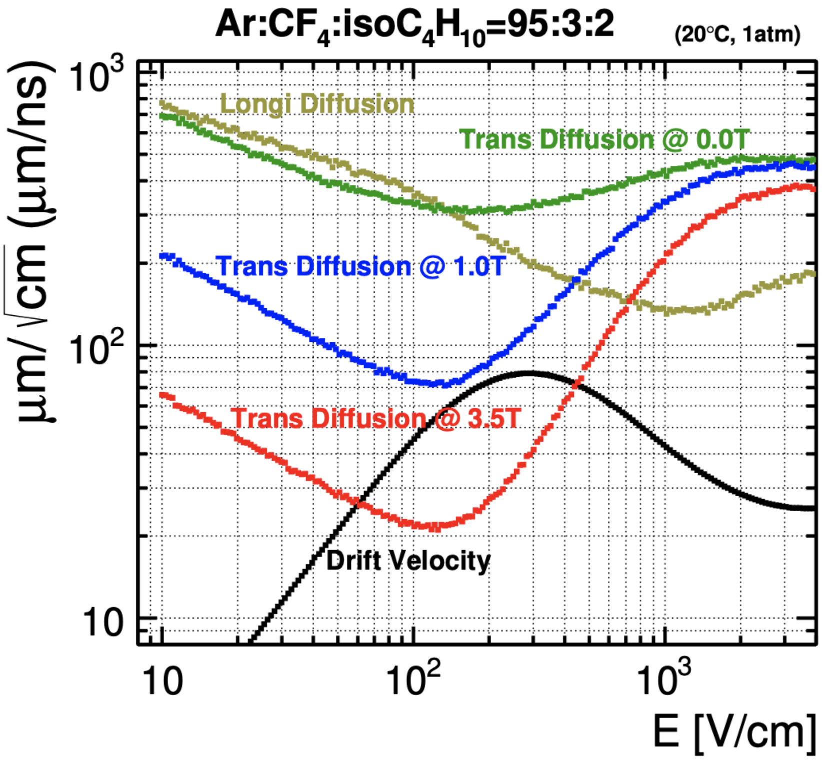

Figure 50: Transverse and longitudinal diffusion constant and drift velocity as a function of electric field in the drift region [41].

4.8 Event Reconstruction

The raw data from each channel of the ALTRO readout system are output as a series of ADC counts corresponding to the signal current integrated over 50 ns-wide time bins with an electronics channel address encoding RCU ID, FEC ID, and readout channel ID within the FEC. The electronics channel address is then decoded and translated into a detector address that encodes the ID numbers of the GEM module and the pad in question according to a channel map (see Figure 51). The detector channel address allows us to locate the pad connected to the electronics channel. The series of ADC values from the readout channel is associated with one or more signal pulses on the pad created by seed electrons from one or more charged particle tracks. Our task is to reconstruct these tracks from the raw ADC data. The track reconstruction process consists of the following four steps:

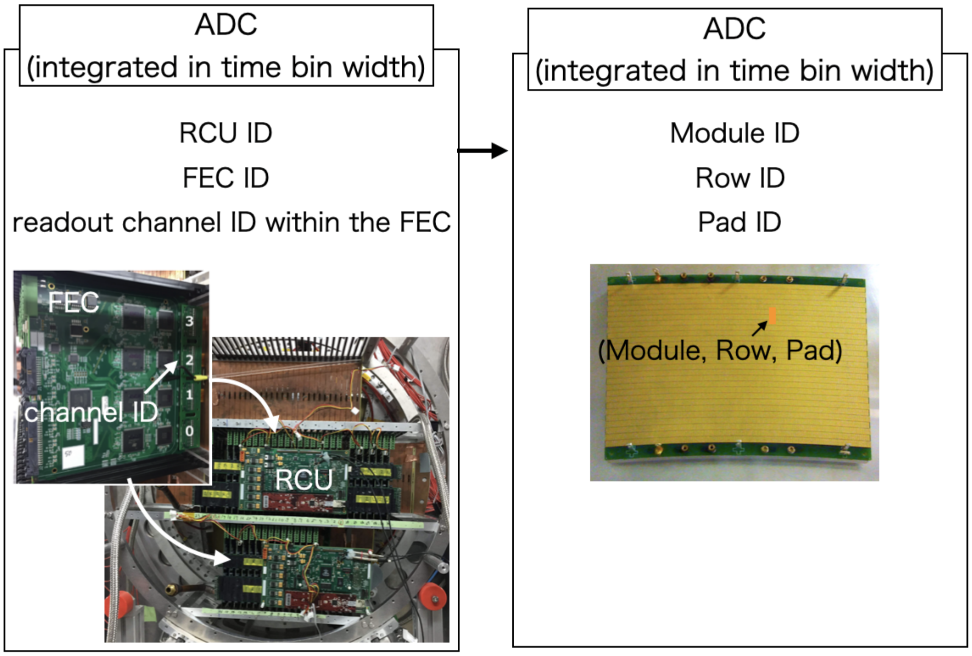

Figure 51: Channel mapping translation.

1. Pulse finding,
2. Hit point making,
3. Track finding, and
4. Track fitting.

We first group the ADC data into contiguous clusters each corresponding to a pulse created by some charged particle track. This first step is called pulse finding. The next step, hit point making, is to collect pulses that are considered to be coming from the same track hence having similar arrival times and hitting a set of contiguous pads on each pad row. We now need to group these hit points into one or more sets each corresponding to a single track. This step is called track finding. Finally, each selected set of hit points are fitted to a helix to determine the track parameters. This final step is called track fitting. The flow of track reconstruction is shown in Figure 52,

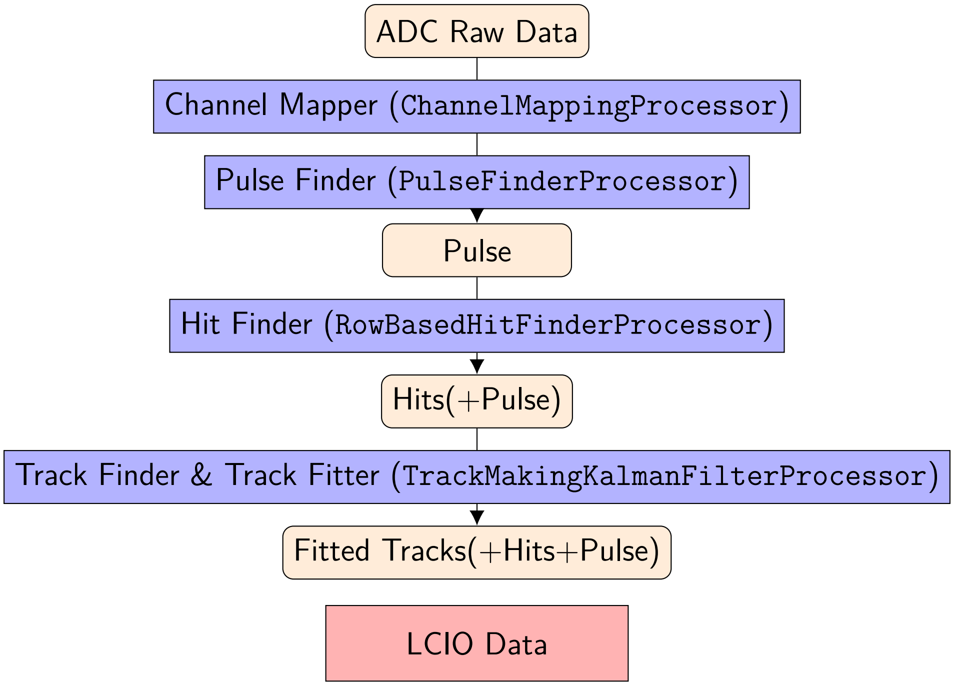

Figure 52: Reconstruction scheme of ILD-TPC data.

We used the `MarlinTPC` framework [42] based on `Marlin` in `iLCSoft` for track reconstruction. `MarlinTPC` can treat the Linear Collider Input/Output persistency framework (`LCIO`), which is the standard framework for detector studies related to ILC.

Pulse Finding Figure 53 is a schematic image of pulses contained in a single hit. Firstly, we find a series of ADC values on a set of contiguous time bins of 50 ns to form a pulse on each pad. Figure 54 shows a schematic image of the pulse. To remove noise pulses we require the following. There must be at least two contiguous time bins with ADC values greater than 3σ, where σ is the standard deviation of the ADC pedestal distribution. The peak time bin must have an ADC value above three ADC counts. We then add one time bin before the

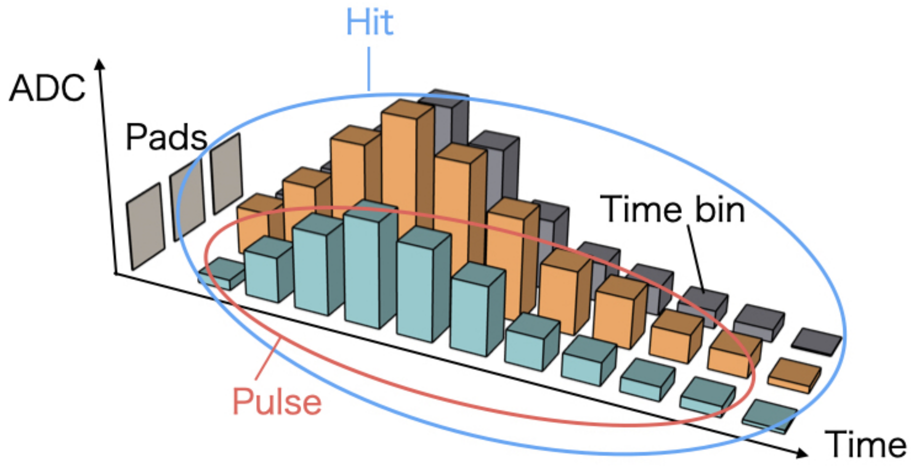

Figure 53: Schematic view of the time bins and pulses which make up a hit.

first time bin above the threshold, and three time bins after the last time bin that exceeds the threshold to the pulse. The arrival time of the pulse is determined by a method that uses

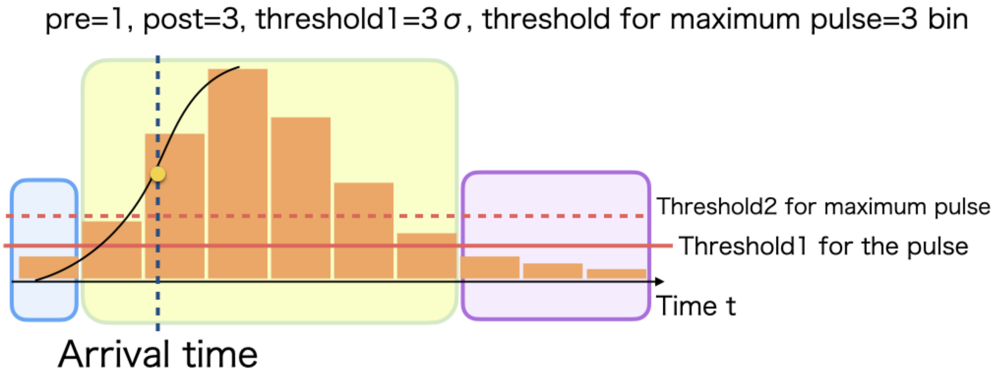

Figure 54: Pulse formation. Threshold1=3σ and threshold2=3ADC.

the inflection point of the leading part of the pulse (inflection point method). Given that the reference time corresponding to zero-drift length and the drift velocity of seed electrons in the ILD-TPC drift volume is known, we can determine the z coordinate as the product of the drift velocity and the drift time.

Hit Point Making From the pulses found in the previous step we make hits by finding in each pad row clusters that consist of pulses on contiguous pads with arrival times consistent with coming from the same track. Those clusters which have a peak ADC value of 12 ADC counts or more are accepted as hit points. Their coordinates are estimated by the so-called Centre of Gravity (C.O.G) method. This method determines the hit point coordinate as the charge weighted mean given by

$$\mathrm{C.O.G} = \frac{\sum (Q_i \cdot x_i)}{\sum Q_i}, \tag{51}$$

where Q_i is the sum of the ADC counts of the i-th pad and x_i is the coordinate of the centre of the i-th pad (see Figure 55).

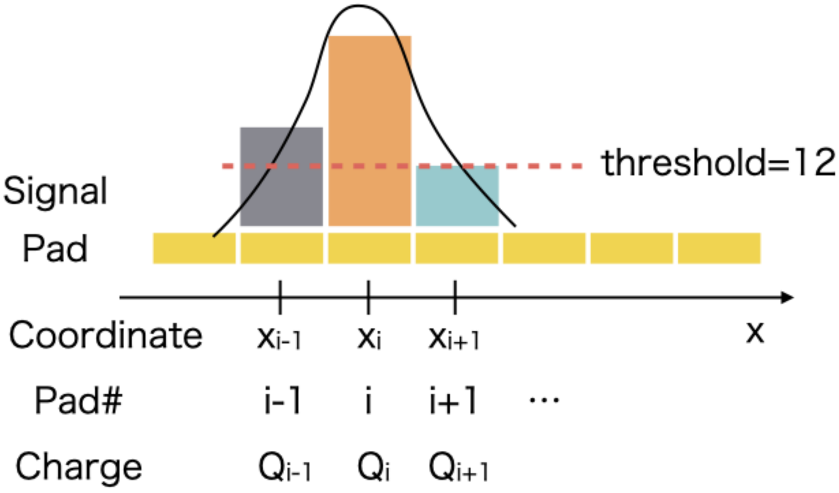

Figure 55: Hit formation.

Track Finding & Fitting Up to this point, one or more hits have been formed in each pad row. Using a Kalman-filter-based track maker, we collect hit points that belong to the same track and fit them to a helix given by the following equation [43] :

$$x(\phi, \mathbf{a}) = \begin{pmatrix} x \\ y \\ z \end{pmatrix} = \begin{pmatrix} x_0 + d_\rho \cos\phi_0 + \rho\left(\cos\phi_0 - \cos\left(\phi_0 + \phi\right)\right) \\ y_0 + d_\rho \cos\phi_0 + \rho\left(\sin\phi_0 - \sin\left(\phi_0 + \phi\right)\right) \\ z_0 + d_z + \rho \tan\lambda \cdot \phi \end{pmatrix}, \tag{52}$$

where $x_0 = (x_0, y_0, z_0)^T$ is the pivot which is usually taken at the hit point, $\mathbf{a} \equiv (d_\rho, \phi_0, \kappa, d_z, \tan\lambda)^T$, $\rho = \frac{\alpha}{\kappa} = \frac{\alpha \cdot P_t}{Q}$. The ρ is the signed radius of the helix, which is equal to $\frac{1}{cB}$ when the magnetic field B is constant (c is the speed of light). ϕ is the angle of deflection from the reference point to a point on the helix, relative to the centre of the helix. This helix equation contains the following five parameters as illustrated in Figure 56:

d_ρ: the distance between the helix and the reference point in the x-y plane perpendicular to the z-axis (axis parallel to the magnetic field),

ϕ_0: the azimuthal angle of the reference point relative to the centre point of the helix,

κ: charge Q of a charged particle divided by its transverse momentum (momentum projected onto the x-y plane) P_t,

d_z: distance in the z-axis direction between the helix and the reference point, and

$\tan\lambda$: angle of the helix from the plane perpendicular to the beam axis (dip angle).

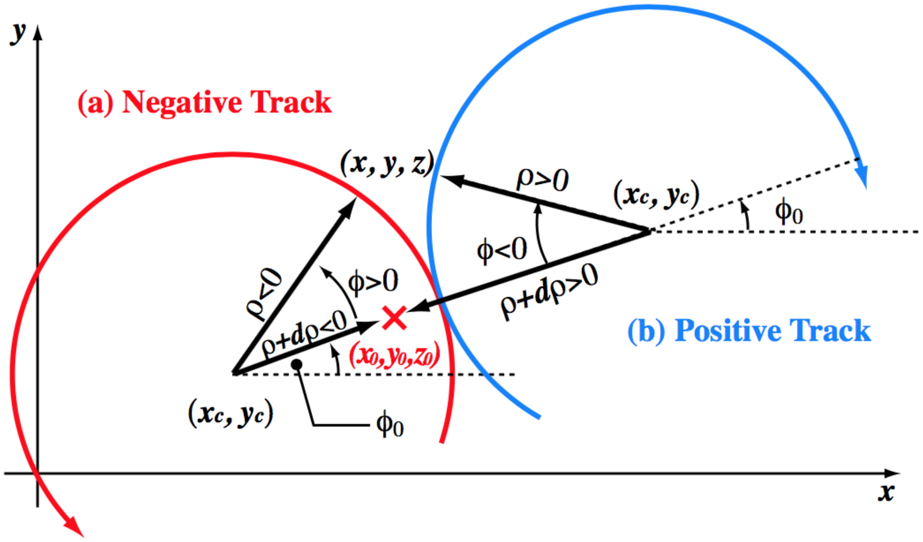

Figure 56: Track parameters [43].

4.9 Analysis

4.9.1 Event Selection

In order to select good events, we applied cuts on the number of tracks per event, number of degrees of freedom, $\kappa = Q/P_T$ in Equation 4.8, and the incident angle ϕ.

Number of Tracks Figure 57 shows the distribution of the number of tracks per event. Single track events were selected to exclude events with electromagnetic showers caused by interaction with matter.

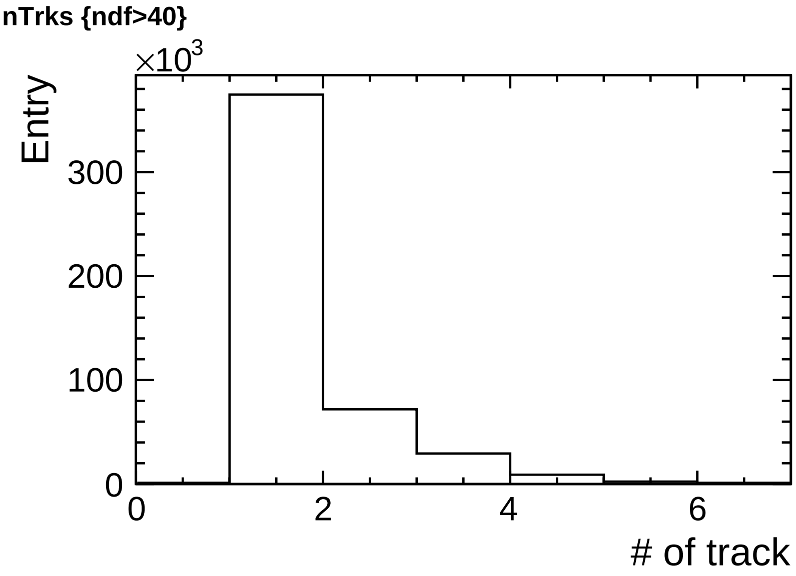

Figure 57: Number of tracks distribution.

Number of Degrees of Freedom (NDF) The number of degrees of freedom (NDF) is determined by the number of rows and track parameters. We use a modules with 28 rows providing two coordinates $r\phi$ and z, while five helix parameters are used for track fitting, resulting in $NDF = 28 \times 2 - 5 = 51$. Therefore, we required NDF to be at least 40, corresponding to 23 hits.

κ Figure 58 shows the κ distribution for single-track events after the NDF cut. The peak is at -0.2, corresponding to an incident electron beam with momentum of 5 GeV. The lower tail is from bremsstrahlung. In order to suppress the electrons associated with bremsstrahlung photons, we apply a cut on κ. However, the tighter the κ cut becomes, the higher the apparent momentum resolution results, potentially biasing our spatial resolution analysis. In Figure 59, we show the $r\phi$ resolution as a function of the upper (left) and lower (right) limits of κ values and selected the cut values within the flat region. Finally, we decided to require $-4\ \mathrm{GeV}^{-1} \cdot c < \kappa < 5\ \mathrm{GeV}^{-1} \cdot c$.

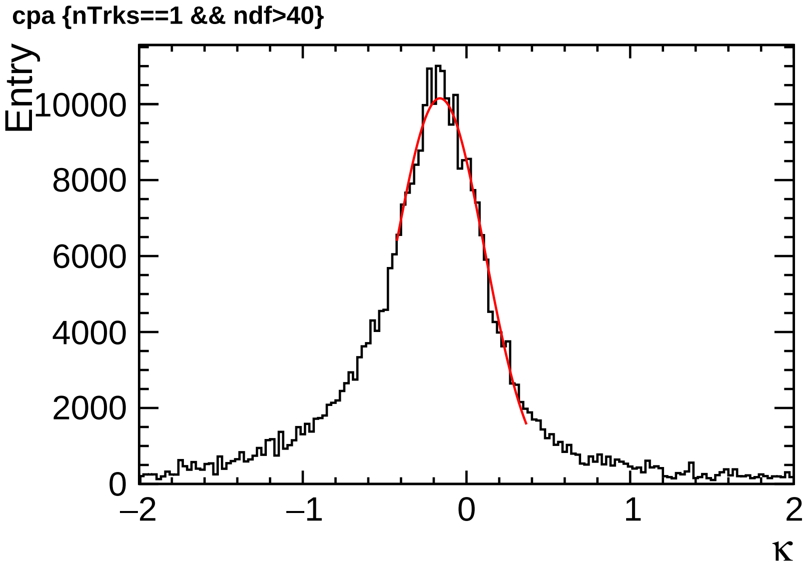

Figure 58: κ distribution in units of $\mathrm{GeV}^{-1}c$.

Incident Angle ϕ The incident angle ϕ is the angle the track makes to the line perpendicular to the pad row in question. The left plot in Figure 60 shows the distribution of the incident angles. The tracks in the lower tail have a small momentum because of bremsstrahlung. These small momentum particles have large curvature. In order to select only stiff tracks with a momentum close to the nominal 5 GeV, we apply a cut on ϕ. To determine the cut value, we scan the ϕ cut value and check how the $r\phi$ resolution depends on it. The right plot of Figure 60 shows the $r\phi$ resolution as a function of the ϕ cut value. We select a cut value of 4σ of standard deviation from fit of incident angle distribution, which is in the flat region.

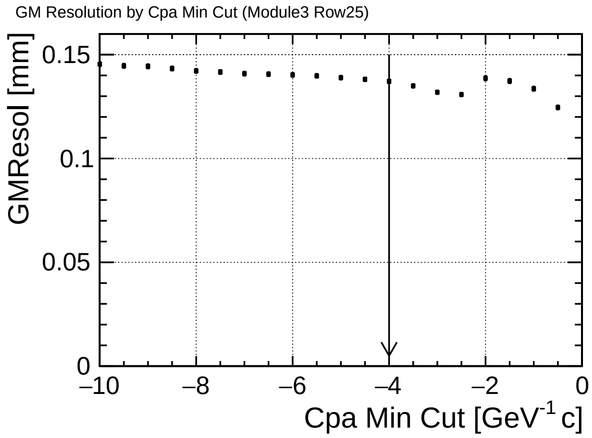

Figure 59: $r\phi$ resolution as a function of κ: (left) minimum value cut, (right) maximum value cut.

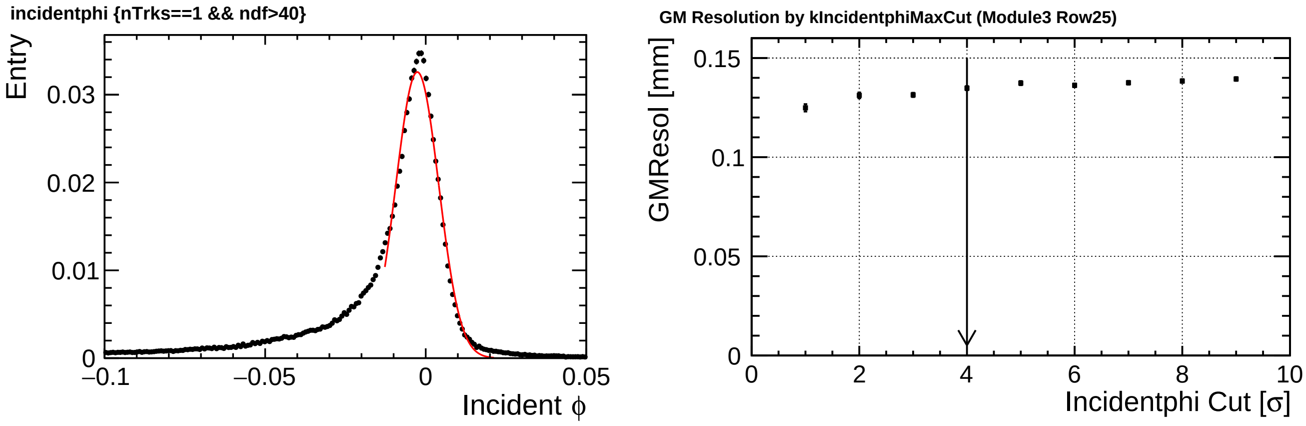

Figure 60: (Left) Incident ϕ distribution. (Right) $r\phi$ resolution at different incident ϕ cut.

4.9.2 Drift Length Calibration

The ILD-TPC large prototype is mounted on a mover, thus we can change the incident position and angles as well as drift length. The mover z position reading should be one-to-one mapped to the drift length.

We calibrated the drift length using data taken at different mover z positions, one of which was chosen to make the beam hit the chamber cathode plane (cathode hit data). The calibration proceeds as follows.

1. We determine the time t_c, corresponding to the cathode z position, using the cathode hit data.

2. We then estimate the drift velocity (V) from the dependence of the drift time on the z mover position.

3. We determine the time t_0 for zero drift length ($z = 0$) corresponding to the surface of the first amplification GEM facing the drift volume. The t_0 satisfies the following equation:

$$V \times (t_c - t_0) = 57.7 \text{ cm (full drift length)}. \tag{53}$$

4. We decide the calibrated drift length using

$$z_i = V(t_i - t_0), \tag{54}$$

where t_i is the time corresponding to the i-th mover z position.

To determine t_c, we plotted the ADC count against the arrival time (Figure 61). The beam has about a 1 cm width. In the case of the cathode hit data, a part of the beam hits the cathode, therefore the drift time distribution is missing the part of the track that is behind the cathode. The higher edge of the time distribution should be identified with t_c. To estimate the drift velocity V, we plot the mover z position against the mean value of the corresponding arrival time distribution (Figure 62) as shown in Figure 63. We can get the drift velocity from the slope of this plot. We substitute the drift velocity in the following equation:

$$V \times (t_c - t_0) = 57.7 \text{ cm}. \tag{55}$$

We can then determine t_0, which is the arrival time for the zero-drift length ($z = 0$). Finally, the calibrated drift length z_i is obtained by substituting t_i, the time corresponding to the i-th mover z position, in the following equation:

$$z_i = V(t_i - t_0). \tag{56}$$

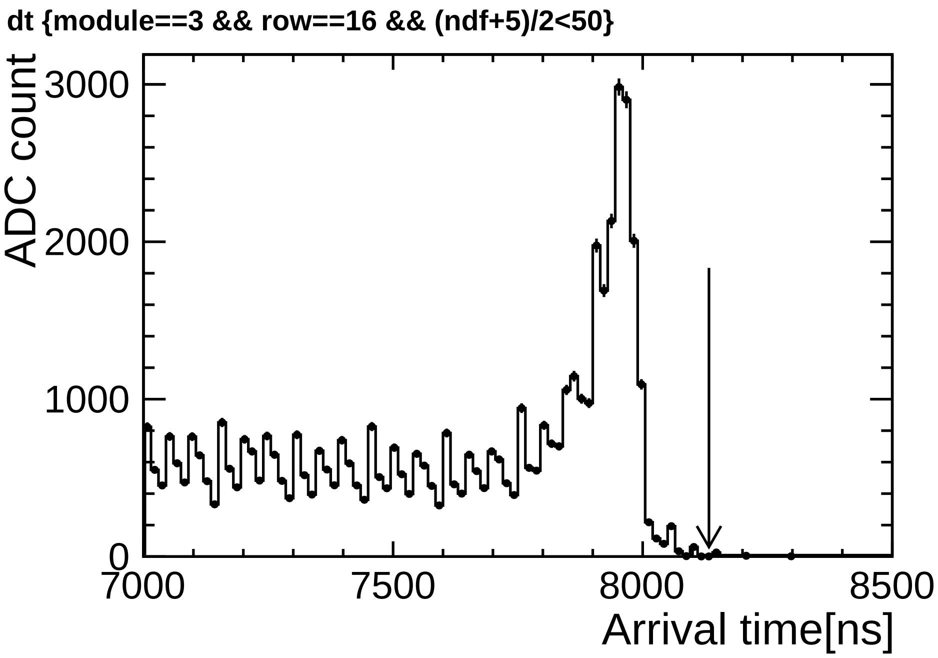

Figure 61: Arrival time distribution of the cathode hit data. The arrow indicates t_c

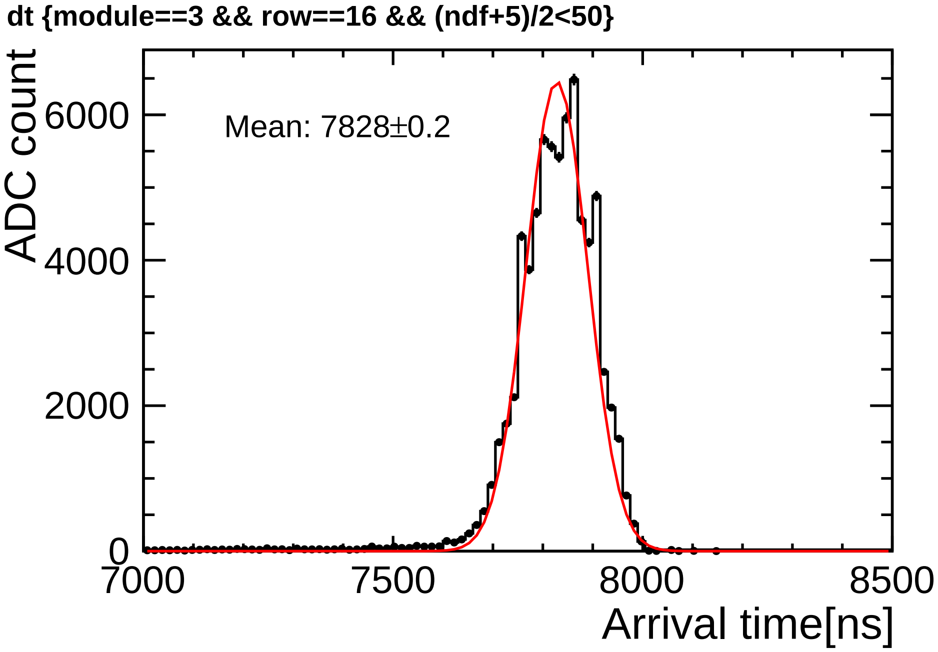

Figure 62: Arrival time distribution of typical data.

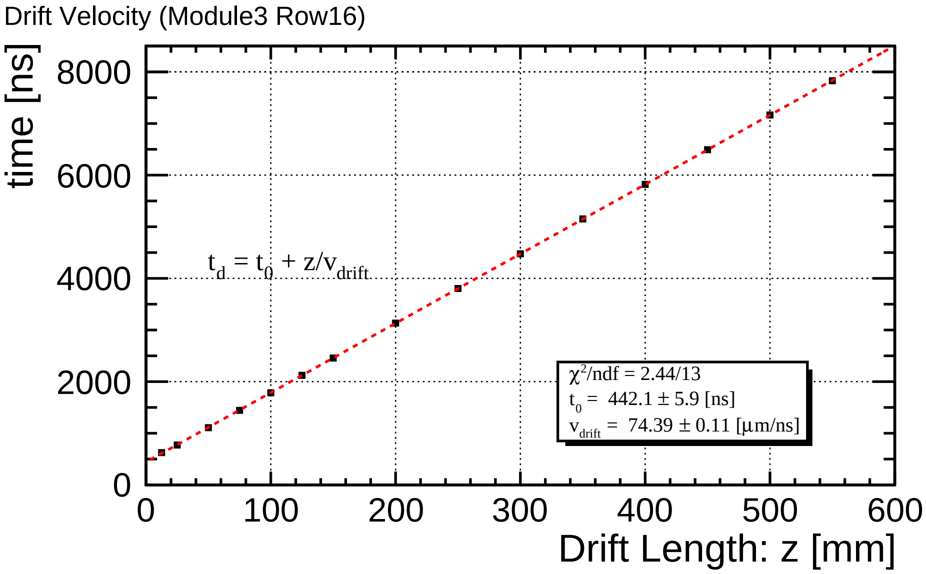

Figure 63: Drift velocity fit of a typical run set.

4.9.3 $r\phi$ Resolution Result

In this section, we estimate the $r\phi$ resolution of the Asian module using the events selected and calibrated as above. The resolution can be determined from the standard deviation of the distribution of the residual which is defined to be the distance from each fitted track to the hit position in the pad row in question. The standard deviation of the residual distribution differs depending on whether we include the hit point in question in the fit or not. If the hit point is included in the track fit, the fitted track is pulled towards the hit point, and the width of the residual distribution becomes smaller than the true spatial resolution. On the other hand, if the hit point is not included in the track fit, since the fitted track itself fluctuates by the fluctuations of the other hit points, the width of the residual distribution becomes larger than the true spatial resolution. This effect is known to be cancelled by taking the geometric mean of the results with and without including the hit point in the track fit. The $r\phi$ resolution is thus given by

$$\sigma_{r\phi} = \sqrt{\sigma_{r\phi(in)}\sigma_{r\phi(out)}}. \tag{57}$$

A plot comparing $r\phi$ resolutions with and without the gating device is shown in Figure 64. The spatial resolution is proportional to $\frac{C_{dT}}{\sqrt{N_{eff}}}$ according to the asymptotic formula, Equation 49. In order to obtain $\frac{C_{dT}}{\sqrt{N_{eff}}}$ we fitted the data points to Equation 49 at drift length > 20 cm, where the so-called hodoscope effect can be neglected.

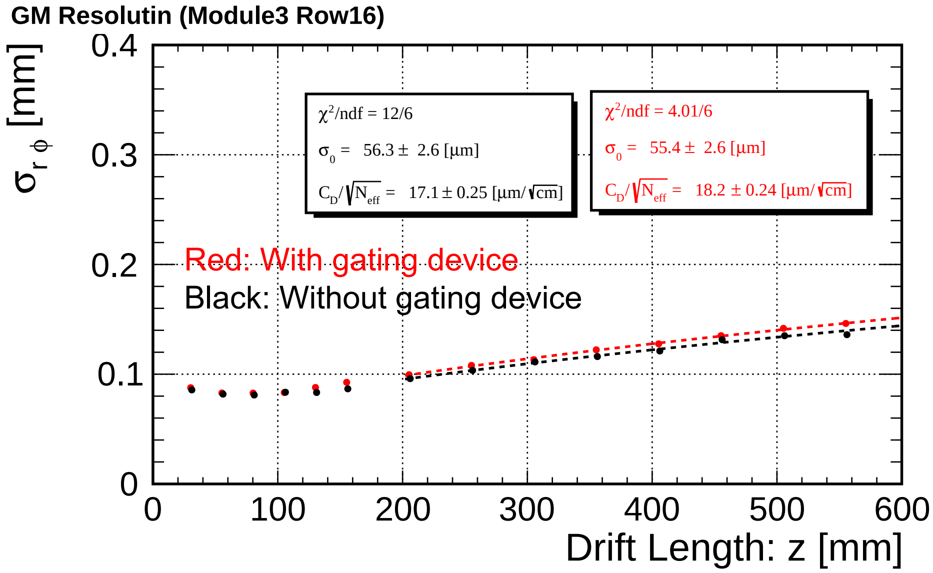

Figure 64: Comparison of $r\phi$ resolution with and without the gating device.

Determination of C_{dT} We now evaluate the transverse diffusion in the drift region from the transverse charge spread of a signal on the readout pad plane. The transverse charge distribution is obtained by plotting the ratio of the charge reaching the i-th pad to the total charge against the distance from the hit point to the centre of the i-th pad. The width of the charge distribution σ_{PR} is obtained by fitting it with the charge distribution function $PR(z)$ representing the pad response to seed electrons:

$$PR(z) = \frac{1}{\sqrt{2\pi}\sigma_{PR}(z)} \exp\left[-\frac{1}{2}\left(\frac{x}{\sigma_{PR}(z)}\right)^2\right]. \tag{58}$$

Figure 65 is an example of the charge distribution with the fit result.

We can obtain the diffusion constant by plotting σ_{PR} at each drift length and fitting the resultant plot to the following equation:

$$\sigma_{PR}^2 = \frac{w^2}{12} + \sigma_{PRF}^2 + C_{dT}^2 z, \tag{59}$$

where w is the pad pitch, σ_{PRF} is the intrinsic charge diffusion in the GEM module, C_{dT} is the transverse diffusion constant, and z is drift length. Figure 66 shows the comparison of the width of the apparent charge spread on the pad plane with and without the gating device. The extracted values of C_{dT} in the two data sets are different: 90.1±0.3 $\mu\text{m}/\sqrt{\text{cm}}$ and 93.2±0.3 $\mu\text{m}/\sqrt{\text{cm}}$ with and without the gating device, respectively. In principle, the

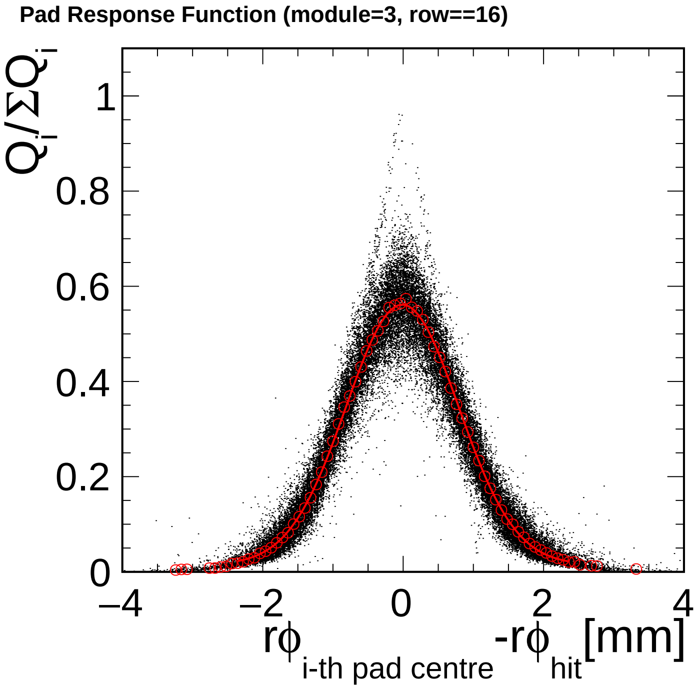

Figure 65: Pad response function.

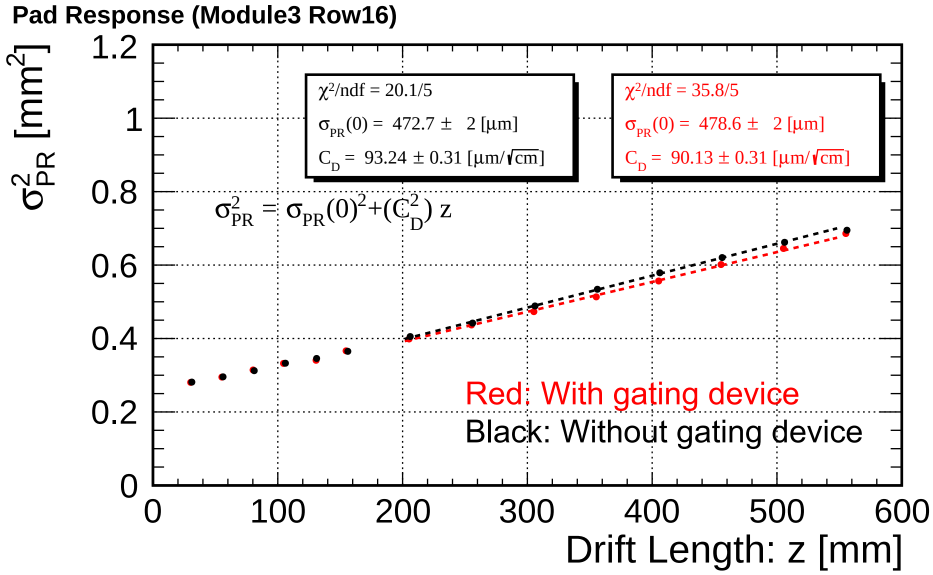

Figure 66: Comparison between the data with and without gating device.

transverse diffusion constant should be the same with and without the gating device because C_{dT} is independent of N_{eff}, if the temperature and pressure are the same. We estimated the C_{dT} values by Garfield++ [44], a toolkit for drift chamber simulation, with the measured temperature and pressure values for the two data taking runs corresponding to the data with and without the gating device. The simulation turned out to be $C_{dT} = 94.1\pm0.6\ \mu\mathrm{m}/\sqrt{\mathrm{cm}}$ and $94.3\pm0.4\ \mu\mathrm{m}/\sqrt{\mathrm{cm}}$, for the data with and without the gating device, respectively, as shown in Table 13. These two values are the same within errors. The observed C_{dT} difference cannot be explained by the temperature or pressure difference.

Table 13: C_{dT} calculated by Garfield++.

	With gate	Without gate
Temperature[K]	291.3	290.4
Pressure[hPa]	1010.8	1005.3
$C_{dT}[\mu\mathrm{m}/\sqrt{\mathrm{cm}}]$	94.1 ± 0.6	94.3 ± 0.4

Difference of C_{dT} from Expectation In order to understand the difference of C_{dT}, we first check if the difference in C_{dT} is due to the gating device by comparing different data sets taken with the gating device as shown in Figure 67. We call the data shown by the red line “Set 1”, the green line “Set 2”, and the blue line “Set 3”. The C_{dT} differed between the different data sets with the gating device. Therefore, the difference in C_{dT} between the data sets with and without the gating device cannot to be attributed to the gating device.

Another potential cause is the underestimation of C_{dT}. When we estimated the charge spread, we used the hit position instead of the track position as the charge centre. This makes the apparent charge spread smaller than reality. This effect can be suppressed by adding the square of the pad response and the square of the spatial resolution as follows. Note that

$$\sigma_{r\phi}^2 = \sigma_0^2 + \left(\frac{{C_{dT}}^2}{N_{eff}}\right) z \sim \frac{k}{N_{eff}} + \left(\frac{C_{dT}^2}{N_{eff}}\right) z \tag{60}$$

$$\sigma_{PR}^2 = \sigma_{PR}^2(0) + C_{dT}^2 \cdot z \sim \left(1 - \frac{1}{N_{eff}}\right) k + \left(1 - \frac{1}{N_{eff}}\right) C_{dT}^2 \cdot z, \tag{61}$$

where k is a common constant. Then we have

$$\sigma_{r\phi}^2 + \sigma_{PR}^2 = \frac{w^2}{12} + C_{dT}^2 \cdot z. \tag{62}$$

Figure 68 shows $\sigma_{r\phi}^2 + \sigma_{PR}^2$ as a function of the drift length. The difference between C_{dT} values did not disappear even with this method. Since the change by this method turned

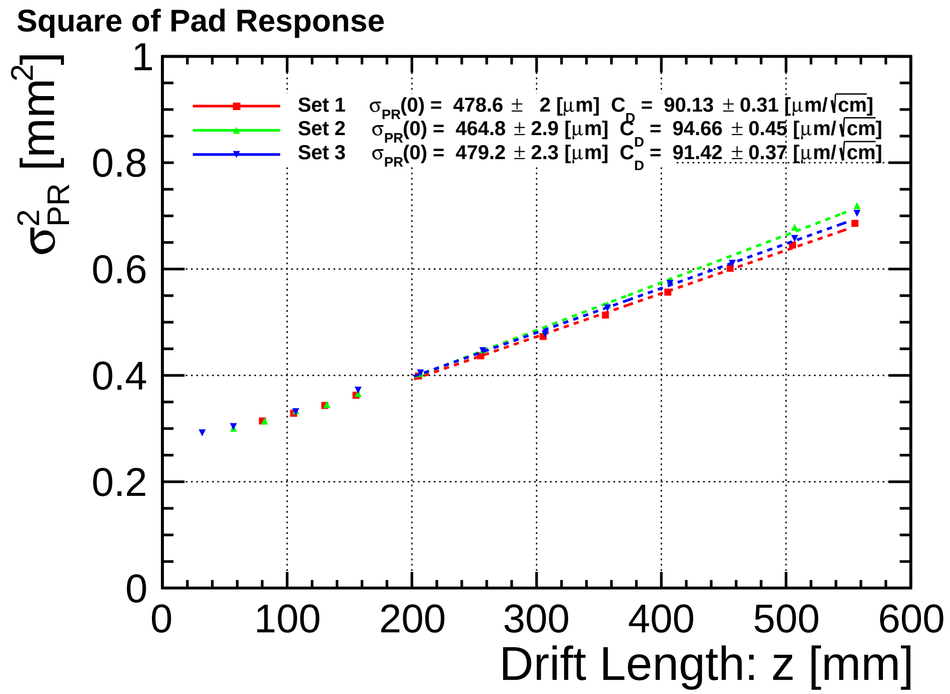

Figure 67: Comparison of different run sets at 1 T with the gating device.

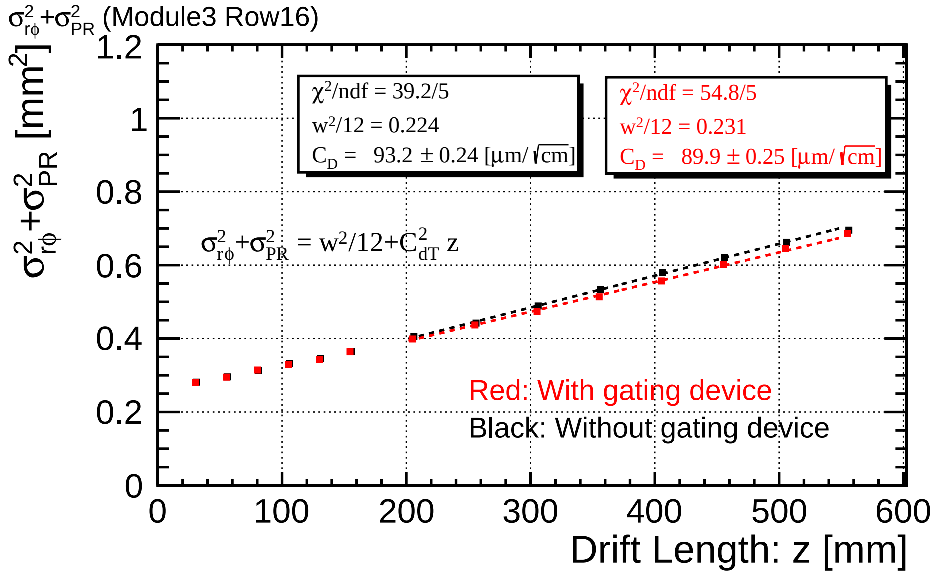

Figure 68: $\sigma_{r\phi}^2 + \sigma_{PR}^2$ as a function of drift length with and without gating device.

out to be small, we use C_{dT} values without this correction in the following.

The remaining possibility is that the positive ions produced in the amplification region returned to the drift region and changed the electric field in the drift region. For this beam test, we did not operate the gating device because we believed that this effect would be small and would not affect the data. Assuming that C_{dT} is affected by positive ions, we tried to estimate how much the magnitude of the electric field had to decrease.

Firstly, C_{dT} was simulated by Garfield++ at the following three drift field values: 200 V/cm, 210 V/cm, and 230 V/cm as plotted in Figure 69. With the linear function $C_{dT} = 0.29 \times (\text{E-field}) + 26.6$ obtained from this plot, the E-field was calculated to be 213 V/cm, 223 V/cm and 220 V/cm for Cd of 90.0 $\mu\text{m}/\sqrt{\text{cm}}$, 91.8 $\mu\text{m}/\sqrt{\text{cm}}$, and 91.0 $\mu\text{m}/\sqrt{\text{cm}}$, respectively. The drift velocities were also compared, since we expect that as the electric field in the drift region becomes smaller, the drift velocity also becomes smaller. The drift velocities of the beam test data are $74.3 \pm 3.1 \times 10^{-6}$ μm/ns, $74.9 \pm 9.3 \times 10^{-6}$ μm/ns, $74.1 \pm 2.0 \times 10^{-6}$ μm/ns for set 1, set 2, and set 3, respectively. The comparison of C_{dT}, E-field, and the drift velocity for each run set is summarised in Table 14. Set 1 and Set 2 show drift velocities smaller than that at 230 V/cm as expected, while Set 3 shows an even smaller drift velocity than expected. It was roughly estimated that the electric field could vary by ± 19 V/m with back flowed ions [45]. The variation of the drift velocity is consistent with this change, suggesting that the variation of the number of positive ions in the drift volume caused by beam intensity variation could be the reason for the C_{dT} difference. This C_{dT} difference is, however, not yet completely understood, and should be verified by a future beam test with a proper beam intensity monitor or gating device operation or both.

Table 14: Diffusion constant, drift velocity of beam test data and electric field estimated using C_{dT} simulation result.

	C_{dT} [$\mu\text{m}/\sqrt{\text{cm}}$]	Drift Velocity [μm/ns]	Simulated E field[V/cm]
set1	90.0 ± 0.3	$74.3 \pm 3.1 \times 10^{-6}$	213
set2	91.8 ± 0.3	$74.9 \pm 9.3 \times 10^{-6}$	223
set3	91.0 ± 0.3	$74.1 \pm 2.0 \times 10^{-6}$	220

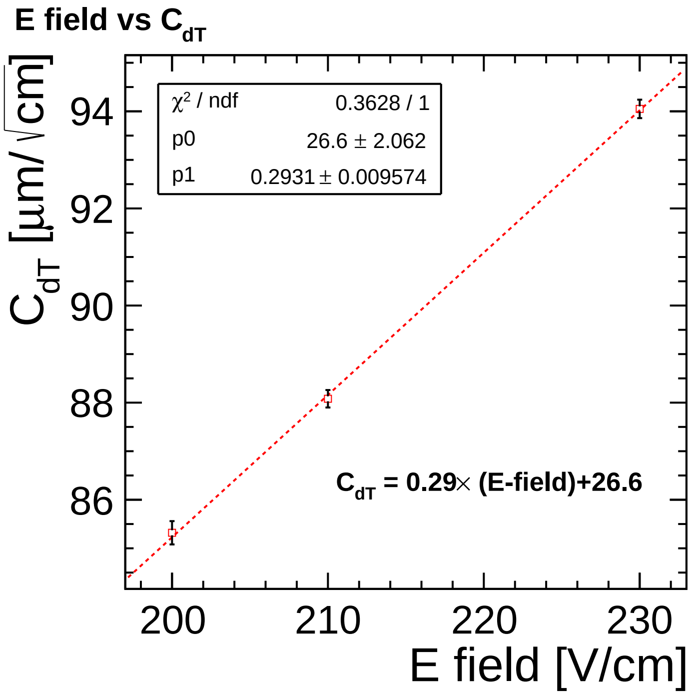

Figure 69: Fitted relation between electric field and C_{dT} of Garfiled++ simulation.

N_{eff} and Electron Transmission of Gating Device In order to estimate the electron transmission rate, we calculated N_{eff} using C_{dT} and $C_{dT}/\sqrt{N_{eff}}$ obtained by fitting the pad response (see Figure 66) and $r\phi$ resolution (see Figure 64) results, respectively. By taking the ratio of N_{eff} with and without the gating device, we can estimate the electron transmission rate, $R_{e.t.}$ as shown in Equation 63.

$$\frac{N_{eff}(\text{w/ Gate})}{N_{eff}(\text{w/o Gate})} \approx R_{e.t.} \tag{63}$$

We summarise C_{dT}, $C_{dT}/\sqrt{N_{eff}}$, the estimated N_{eff} with and without the gating device, and their ratio in Table 15. The electron transmission rate was estimated to be 82.5%, which is consistent with the optical aperture of the gating device.

Table 15: Summary table of estimated N_{eff} and the electron transmission rate.

	w/gate	w/o gate	ratio[%]
C_d [μm/$\sqrt{\text{cm}}$]	90.1 ± 0.3	93.2+0.3	
$C_d/\sqrt{N_{eff}}$ [μm/$\sqrt{\text{cm}}$]	18.2 ± 0.2	17.1+0.3	
N_{eff}	24.5 ± 0.7	29.7 ± 0.9	82.5 ± 3.3

Extrapolation of $r\phi$ Resolution to a Real-size ILD-TPC In the previous section, we showed that the $r\phi$ resolution results for the module with the gating device can be expressed in terms of the parameters of the analytic $r\phi$ resolution formula and that the values of the parameters agree well with theory except for C_{dT}. Using the analytical resolution formula, we therefore extrapolated the $r\phi$ resolution of the beam test to that of the ILD-TPC case with a magnetic field of 3.5 T and a maximum drift distance of 2.2 m, assuming the Garfield++ simulation value of C_{dT} and the experimentally obtained value of N_{eff}. Figure 70 shows the result of this extrapolation. The red line (a) shows the $r\phi$ resolution extrapolated with the same parameters of the large prototype. In this case, the $r\phi$ resolution deteriorates at short drift distances because the width of the pad response function (σ_{PRF}) decreases as the magnetic field increases. The black line (b) corresponds to the case in which the distance between the GEM and the pad plane is increased so that σ_{PRF} is kept at the same value as at B=1 T. This way, the target spatial resolution of 100 μm can be achieved over the full drift length up to 2.2 m with our end-plane readout module with the gating device.

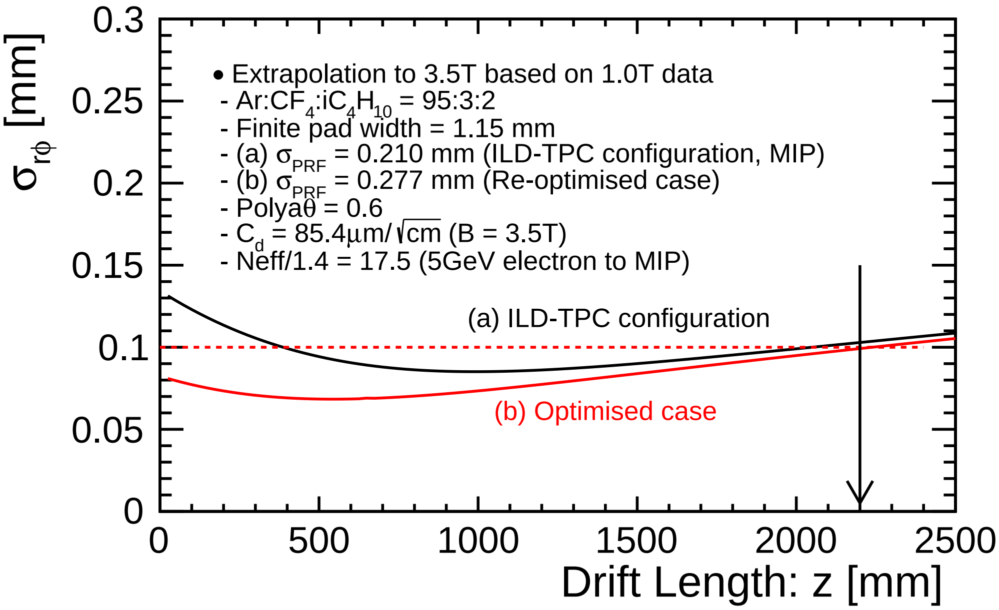

Figure 70: Extrapolation of the beam test to 3.5 T as a function of drift length. The red line shows the directly extrapolated result, the back line shows the case with adjusted σ_{PRF}.

4.9.4 z Resolution

Let us now move on to the z resolution. The z resolution can be express as $\sigma_z = \sqrt{\sigma_0^2 + (C_{dL}^2/N_{eff})\, z}$, where C_{dL} is the longitudinal diffusion constant. We again compare data with and without the gating device. The results are shown in Figure 71. The red line shows the z resolution with the gating device, and the black line indicates that without the gating device. If we assume that the z resolution is independent of the magnetic field, we estimate the z resolution at the full drift of 2.2 m as

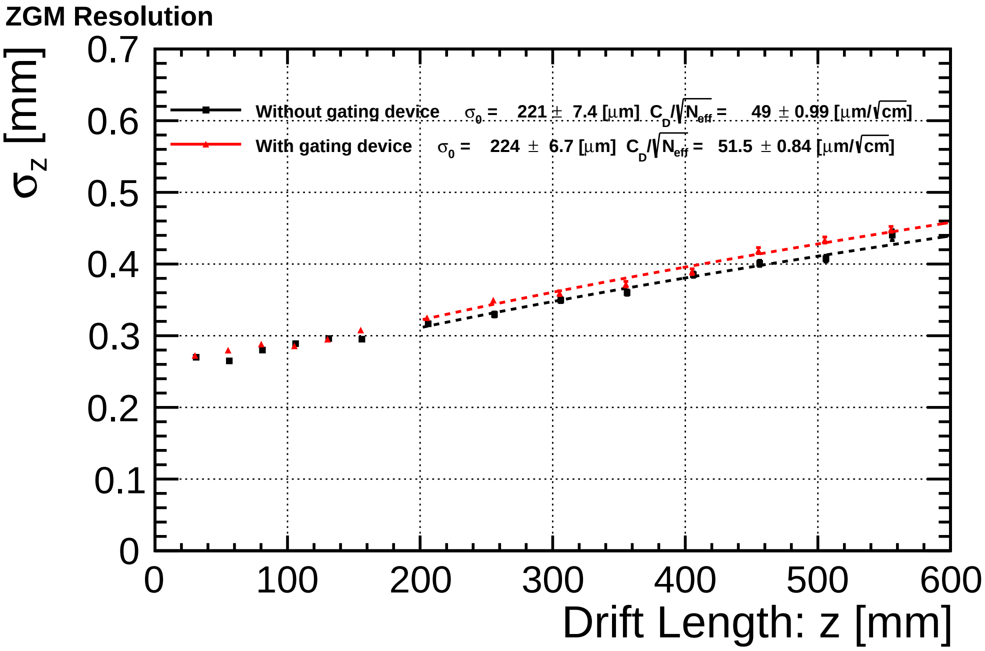

Figure 71: Comparison between with and without gating device. The red line shows the σ_z with gate, and the black line shows the σ_z without gate.

$$\begin{aligned} \sigma_z &= \sqrt{\sigma_0^2 + (C_{dL}^2/N_{eff})\, z} = \sqrt{(224 \pm 6.7)^2 + (51.5 \pm 0.84)^2 \cdot 220}[\mu\mathrm{m}] \\ &= 796 \pm 12\ [\mu\mathrm{m}]. \end{aligned} \tag{64}$$

This result indicates that the z resolution at the full drift of 2.2 m would be 796±12 μm, well below the target value of 1.4 mm. To confirm whether the assumption that the z resolution is independent of the magnetic field is correct, we compare the z resolution with and without the magnetic field of 1 T in Figure 72. Contrary to our expectation, the z resolutions at 0 T and 1 T differ significantly, by about 20%. The slope value C_{dL} of 0 T is 52.2±1.6 $\mu\mathrm{m}/\sqrt{\mathrm{cm}}$, and 1 T of 51.5±0.8 $\mu\mathrm{m}/\sqrt{\mathrm{cm}}$. These two values are in good agreement, on the other hand the intercept value σ_0 of 0 T of 312±9 μm differ from its of 1 T of 224±7 μm.

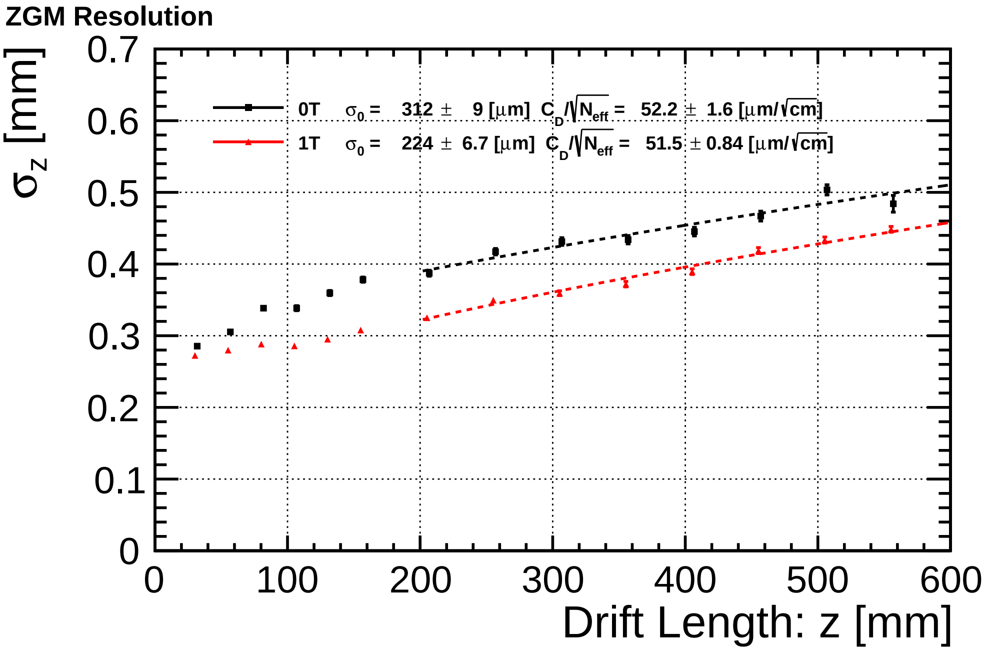

Figure 72: Comparison between with and without gating device. The red line shows σ_z with gate, and the black line shows the σ_z without gate, as a function of the drift length. Use 1 pad for calculation of z coordinate, inflection point method.

The dependence of the z resolution on the magnetic field has not been studied carefully, since the z resolution has been believed to be independent of the magnetic field because of the absence of the electron curling up effect that suppresses the diffusion in the transverse directions. To understand the observed difference of the z resolution caused by the magnetic field, we analyse in the next section the pulse shape that affects the z resolution.

4.10 Pulse Shape Study

Since the main factor affecting the z resolution is the pulse shape, we now analyse the pulse shape of the beam test data. The z coordinate of a hit point is determined by the inflection point of the leading part of the peak pulse in the hit. The z coordinate accuracy hence depends on the pulse shape.

4.10.1 Factors that Determine Pulse Shape

We first assume that the pulse shape is solely determined by the characteristics of the readout electronics, the shaper in particular, and the longitudinal diffusion in the drift region. Each electron arriving at a readout pad generates a delta function-like impulse current which is shaped into a shape according as unipolar-shaper signal function by the shaper. The observed pulse is then a superposition of the contributions from multiple electrons with an arrival time spread determined by the longitudinal diffusion. The effect of diffusion can hence be estimated as the spread of arrival times.

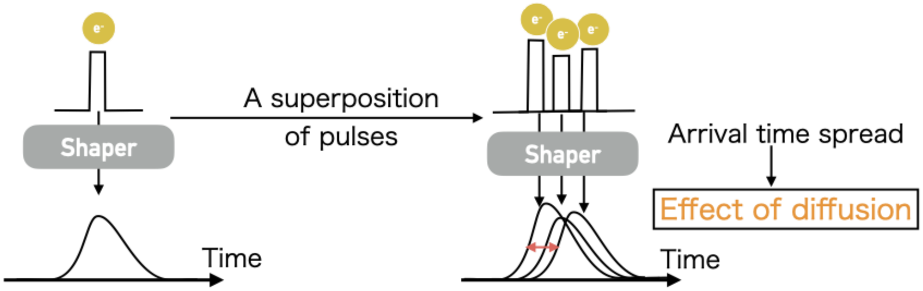

Figure 73: Illustration of signal shaping.

We will now explain how we evaluate the pulse shape. The characteristics of the shaper in the current setup can be represented by a unipolar-shaper signal function as follows.

$$f(t,\tilde{t}) = \frac{1}{n!\,(t_{pk}/n)} \left(\frac{t-\tilde{t}}{t_{pk}/n}\right)^n e^{-\left(\frac{t-\tilde{t}}{t_{pk}/n}\right)}, \tag{65}$$

where n is a parameter called shaper order, t_{pk} is the peaking time, and $\tilde{t}$ is the true electron arrival time. Their nominal values are $n = 3$ and $t_{pk} = 120$ ns according to the shaper circuit specification sheet. The arrival times of the seed electrons are expected to be Gaussian-distributed, which means that the pulse shape can be represented by a convolution function of this Gaussian and the shaper function $f(t)$ as follows.

$$\left\{f(t,\tilde{t}) = \frac{1}{n!\,(t_{pk}/n)}\left(\frac{t-\tilde{t}}{t_{pk}/n}\right)^{n} e^{-\left(\frac{t-\tilde{t}}{t_{pk}/n}\right)}\right\} \otimes \left\{g(\tilde{t}) = \frac{1}{\sqrt{2\pi\sigma_t^2}}\exp\left(-\frac{(\tilde{t}-\mu)^2}{2\sigma_t^2}\right)\right\}, \tag{66}$$

where $\sigma_t = \sigma_L/v_{\mathrm{drift}}$. The standard deviation of the Gaussian part can then be interpreted as the diffusion effect. If we can assume that the pulse shape depends only on the characteristics of the shaper and the longitudinal diffusion effect in the drift region, then the pulse shape of the beam test data should be described by this convoluted function.

The standard deviation due to longitudinal diffusion is expected to increase as the drift length increases. If the square of the standard deviation is plotted as a function of the drift length, the function can be expressed as

$$\sigma_L^2 = \sigma_L(0)^2 + C_{dL}^2 \cdot z. \tag{67}$$

where $\sigma_L(0)$ is the finite time bin width effect that can be expressed as

$$\sigma_L(0) = \frac{\text{Drift velocity } \times \text{ time bin width}}{\sqrt{12}} \tag{68}$$

Substituting the input values into Equation 68, we obtain the expected intercept value of about 1.1 mm. We can extract the longitudinal diffusion constant C_{dL} as the slope of this function.

4.10.2 Validity Test of the Method by Simulation

Before we estimate the longitudinal diffusion constant C_{dL} for the beam test data, we test whether this method of C_{dL} estimation works or not with simulation data generated with the longitudinal diffusion in the drift region as the only source of the arrival time spread. We generate a pulse as the superposition of the pulses for individual seed electrons with the arrival time spread corresponding to the longitudinal diffusion constant of 226.3 $\mu\mathrm{m}/\sqrt{\mathrm{cm}}$, which is rough estimate by Garfield++. For the simulation, we use the nominal shaper parameters: $n = 3$ and $t_{pk} = 120$ ns, the nominal time bin width of 50 ns, and a drift velocity of beam test result of 74.4 μm/ns. We then fit so generated pulses with the convolution function.

The square of the standard deviation of the resulting Gaussian part is plotted for each drift length as shown in Figure 74. The diffusion constant C_{dL} is obtained as the slope of this plot. The resultant C_{dL} value is 222.7 ± 0.1 $\mu\mathrm{m}/\sqrt{\mathrm{cm}}$, which agrees with the input value to about 1%. This method of evaluating C_{dL} is hence valid to 1 % accuracy.

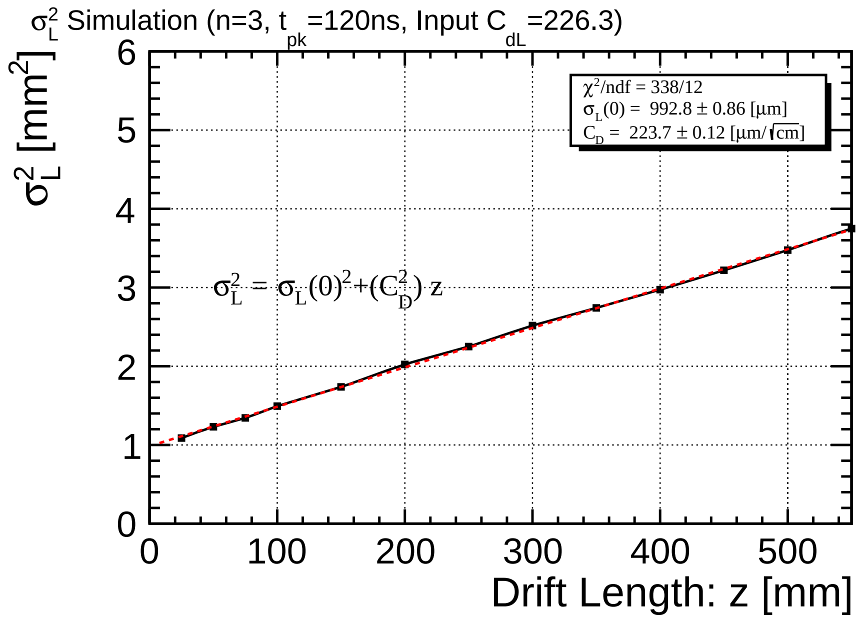

Figure 74: Estimation of the effect of diffusion by pulse convolution fit using simulation data with input $C_{dL} = 226.3$. ($n = 3$ and $t_{pk} = 120$ ns.)

4.10.3 Comparison with Beam Test Data

Similarly, the pulses of the beam test data were fitted first with the convolution function with fixing the shaper parameters at their nominal values: $n = 3$ and $t_{pk} = 120$ ns. The fit resulted in $C_{dL} = 267.4 \pm 0.5$ μm/$\sqrt{\text{cm}}$, larger than the expected diffusion constant of 226.1 ± 3.5 (see Appendix). The resultant intercept value of 2.4 mm is also larger than the expected value.

The nominal t_{pk} value might be different from reality, and the resultant C_{dL} value from the fit might depend on the choice of the fixed input t_{pk} value. We hence investigated whether we could reproduce the expected C_{dL} and intercept values by adjusting the input peaking time. As shown in Figure 76, at $t_{pk} = 135$ ns, we obtain C_{dL} of 224.2 ± 0.4 μm/cm and σ_0 of $1.1 \pm 3 \times 10^{-3}$ mm, which are in reasonable agreement with the expectation. This shows that the C_{dL} fit method is rather sensitive to the input t_{pk} value.

4.10.4 C_{dL} Estimation Using z Resolution Result

We could not reproduce the C_{dL} with C_{dL} fit method, therefore we now try another way to estimate C_{dL}. Assuming that N_{eff} that appears in the z resolution formula is the same as that in the $r\phi$ resolution for the same data, we can estimate the longitudinal diffusion

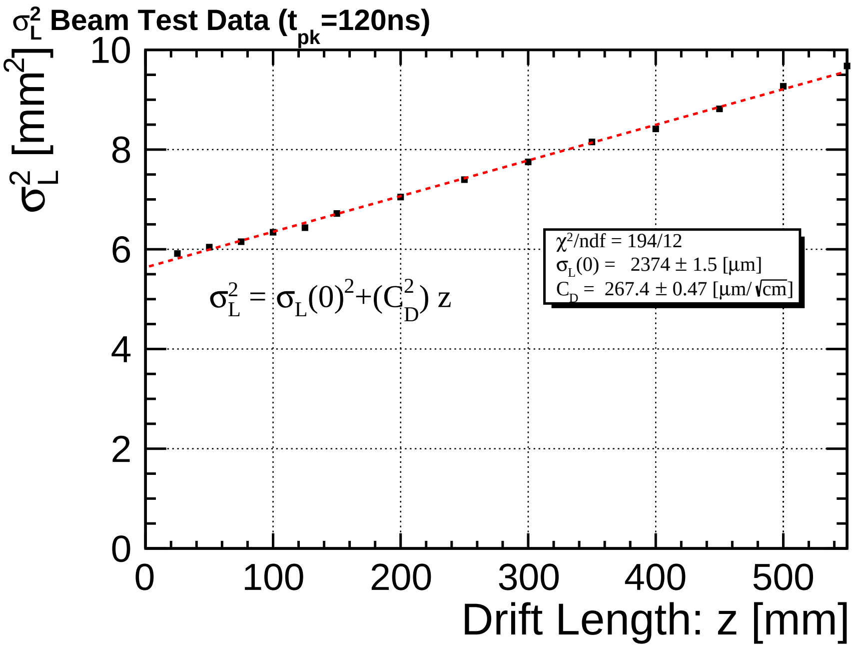

Figure 75: Estimation of the effect of diffusion by pulse convolution fit using beam test data. ($n = 3$ and $t_{pk} = 120$ ns.)

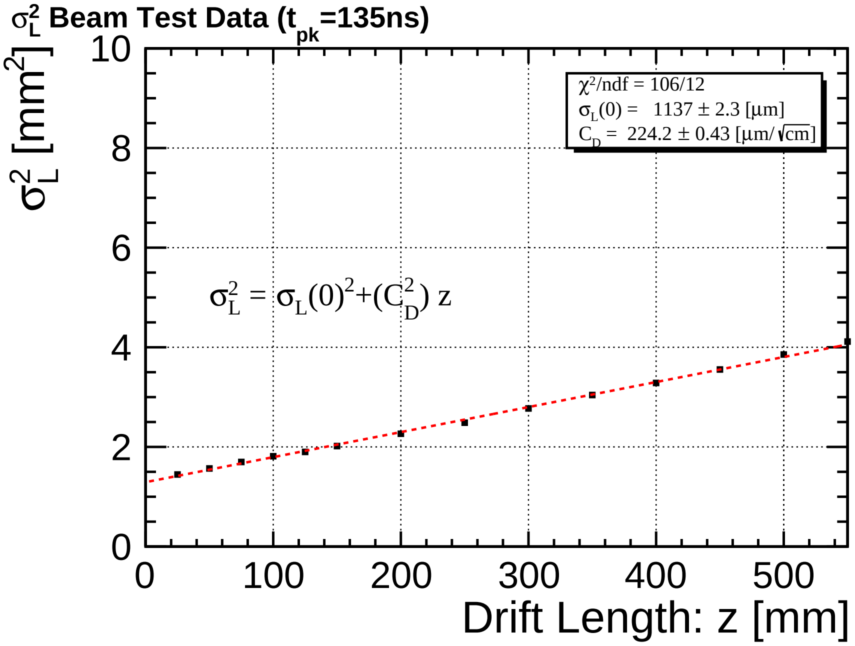

Figure 76: Estimation of the effect of diffusion by pulse convolution fit using beam test data with $t_{pk} = 135$ ns and n=3.

constant C_{dL} from the z resolution data, using the following equation:

$$\sigma_z = \sqrt{\sigma_L(0)^2 + (C_{dL}^2/N_{eff})\, z}. \tag{69}$$

The z resolution at 1 T is shown in Figure 71. N_{eff} was estimated from the $r\phi$ resolution and was found to be 24.5 ± 0.7 μm/$\sqrt{\text{cm}}$ and the estimated value of C_{dL} for this N_{eff} is 258.9 ± 5.7 μm/$\sqrt{\text{cm}}$. This result still differs from the Garfield++ simulation result. However, in general, the z resolution result is expected to depend on the choice of arrival time calculation method, we thus try to improve our time calculation method. We will discuss this point in the next section.

4.10.5 Time Calculation Method Comparison

The potential problem with the currently used inflection point method is that only the leading part of the pulse is used, therefore the information after the peak time bin is lost. In addition at present only the pad with the highest ADC count is used to calculate the arrival time. Normally, a hit point consists of 3 or 4 pads, so information would be lost here as well. In this section, we compare the inflection point method with the centre of gravity method, in terms of z resolution, varying the numbers of used pads and time bins.

Two Time Calculation Methods The C.O.G method uses the centre of gravity of the time bins as the charge-weighted mean of the time bin positions. In the case of z resolution, the pulse is asymmetric about the peak time bin, so when using C.O.G, the number of time bins used must be optimised. In this section, we call the z resolution using the C.O.G method for drift time calculation "C.O.G method result", and that using the inflection point method "inflection point method result".

Number of Used Time Bins In this section we investigate how the z resolution depends on the number of used bins before and after the peak time bin for the C.O.G method. We compare the z resolution result with 3, 5, 7, 9, 11, 13 time bins with the peak time bin in the centre. According to Figure 77, the C.O.G z resolution result using five time bins (peak time bin ± two bins) turns out to be the best (see the red points). It is also clear that the z resolution deteriorates when too many or too few time bins are used. This could be attributed to the fact that the accuracy of the C.O.G becomes worse when the number of time bins is too small, or when the noise effect dominates in the tail time bins. In the inflection point method, the time calculation does not depends on the number of time bins.

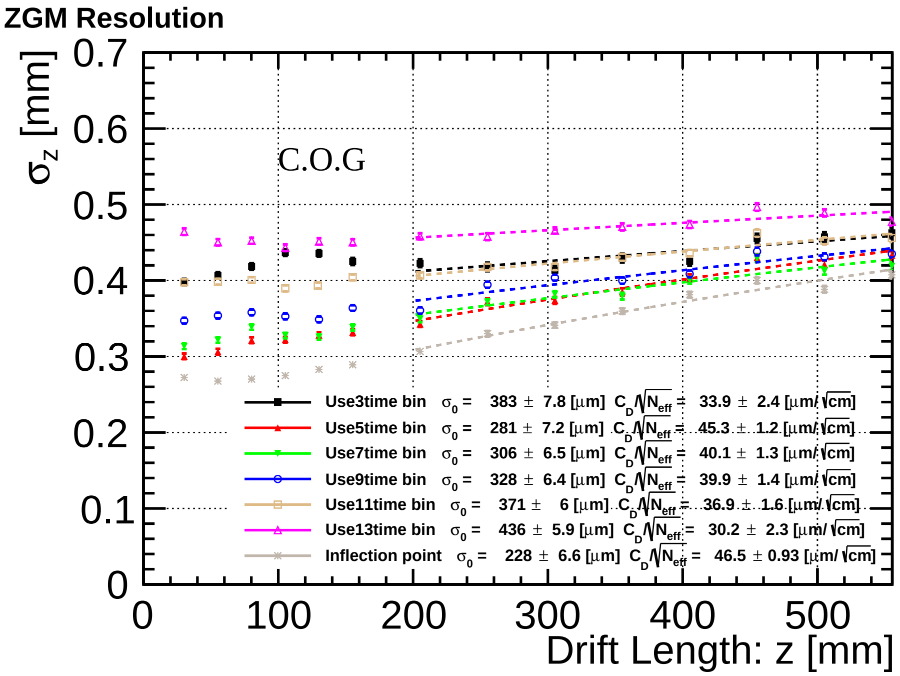

Figure 77: C.O.G method result with various number of time bins. (Beam test result.)

Number of Used Pads This time we vary the number of pads used to calculate the z coordinate. In this analysis, we use the five time bins for the C.O.G method, since we found above that this gives the best result. We combine the information from each pad by taking charge-weighted mean of the signal time estimate for each pad.

$$\frac{1}{\sum_i Q_i} \sum_i Q_i \times \mathrm{time}_i. \tag{70}$$

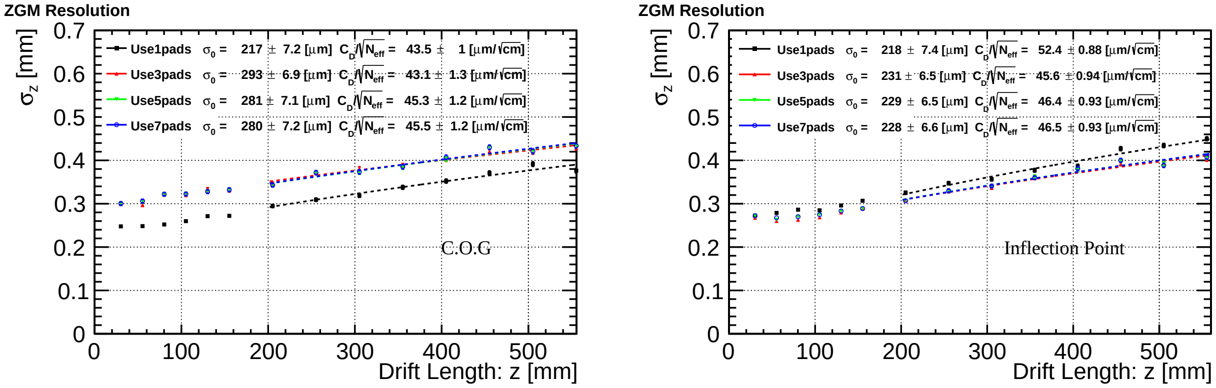

Figure 78: Comparison between C.O.G (Left) and Inflection point (Right) methods using different numbers of pads.

The results are shown in Figure 78. The inflection point result with three or more pads turned out to be better than that with only one pad (the current standard). Naively it is expected that the same thing happens also for the C.O.G method. We found, however, that the z resolution became worse when we used more than one. Understanding these results and comparing them with simulations is a subject for future work. One possible reason is possible pulse shape difference between different pads in a hit. In this study, we assume the side pads have the same pulse shape as the peak pad. Moreover, the side pads are more sensitive to electronic noise. To avoid these potential problems, we could have combined the time bins on hit pads before calculating the arrival time.

4.10.6 Re-estimated C_{dL} and z resolution

The results of the previous section showed that the inflection point method result using all pads of each hit gives the best z resolution. We hence use the z resolution result for this best method to extract C_{dL}. As shown in Figure 79, we obtain $C_{dL}/\sqrt{N_{eff}} = 46.3 \pm 0.9\ \mu\mathrm{m}/\sqrt{\mathrm{cm}}$. The resultant longitudinal diffusion C_{dL} is $229.2 \pm 5.6 \mu\mathrm{m}/\sqrt{\mathrm{cm}}$ using the same method as

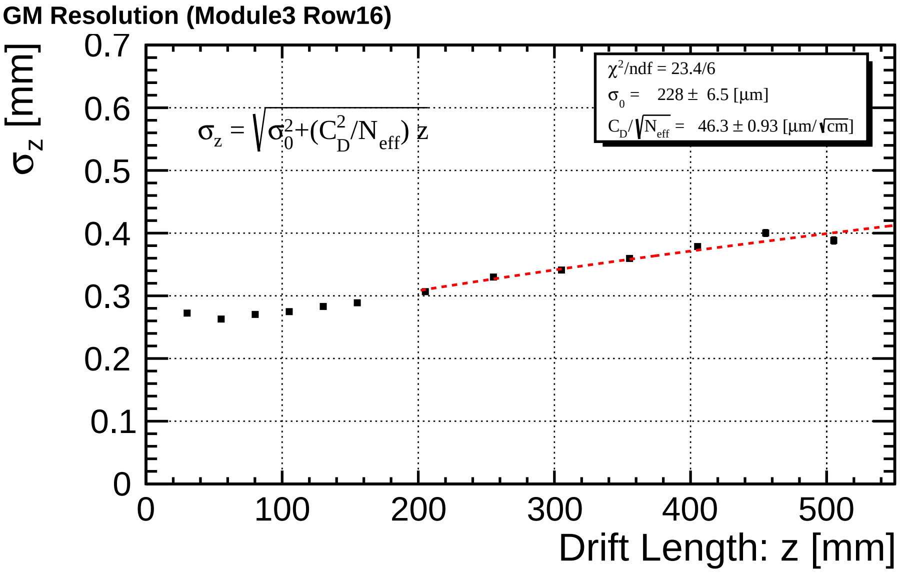

Figure 79: Inflection point method result using all pads of z resolution.

section 4.7.4., which is consistent with the expectation of 226.1 ± 3.4 from our Garfield++ simulation.

We then compared the z resolution again between 0 T and 1 T using all pads in each hit as shown in Figure 80. Comparing this result with the result using the peak pad only, the z resolution of 0 T became worse. This could be attributed to the method of combining pulse information from each pad as explained in the previous section. This method is susceptible to electronic noise in particular for tail pads in the hit in question. The noise effect might be reduced by calculating the signal arrival time after adding up the ADC values for each time bin over all the pads contributing the hit.

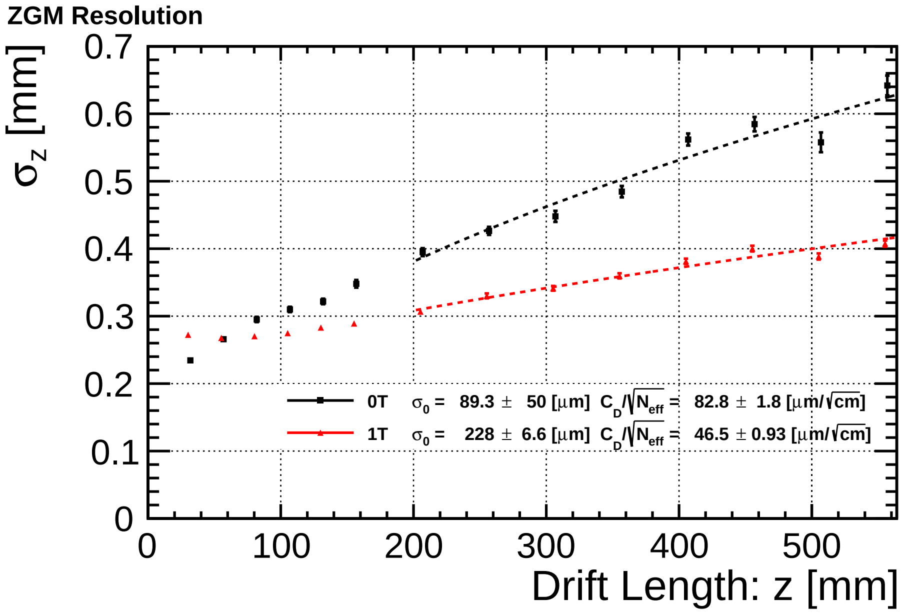

Figure 80: Comparison of z resolution between 0 T and 1 T, using all pads in each hit.

4.11 Software Simulation

There was a ILD-TPC simulator [46] available when we started this study. The simulator, however, could not reproduce the z resolution data at short drift distance. To clarify unknown factors that affect the z resolution at short distance, we developed a new ILD-TPC simulator. In this chapter, we will explain the basic idea for our simulator and compare its results with the beam test data.

4.11.1 Structure of the ILD-TPC Simulator

Our ILD-TPC simulator is written in C++ and contains the following four major modules: `Track`, `GEM`, `PASA`, and `Hit`. Figure 81 sketches the function of each module.

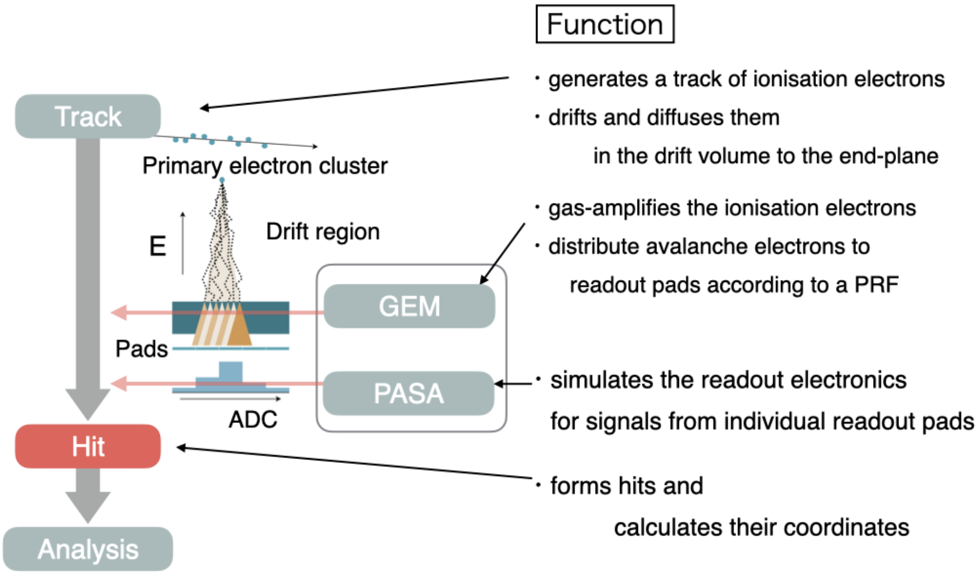

Figure 81: Sketch of the function of each module and their relation.

The `track` module generates a track of ionisation electrons. This module makes electrons drift and diffuse in the drift volume to the end-plane. The parameters for this module contain the average number of the primary ionisations per unit length, the incident position of the track, transverse and longitudinal diffusion constants, and so on. The primary electrons are randomly scattered by collisions with gas molecules until they thermalise, producing secondary electrons. A primary ionisation cluster with a finite spatial size is thus produced.

The size of the primary ionisation cluster is controlled by the range of its corresponding primary ionisation electron. The electrons in each ionisation cluster drift towards the end-plane, while experiencing transverse and longitudinal diffusion. The amount of diffusion in the drift region is controlled by the transverse and longitudinal diffusion constants, C_{dT} and C_{dL}, respectively. The diffusion constants and drift velocity are obtained from Garfield++ simulations.

The `GEM` module describes the gas amplification of the ionisation electrons and the distribution of avalanche electrons to relevant readout pads according to a pad response function. The gas amplification of each ionisation electron is done randomly according to a Polya distribution. Various potential effects of diffusion in the amplification region are not yet included.

The `PASA` module simulates the readout electronics for signals from individual readout pads. Currently each ionisation electron is assumed to create a delta-function-like impulse current to the readout electronics. The `PASA` module converts the delta function input to a unipolar-shaper signal function shape characterised by peaking time t_{pk}, shaper order n, and gain factor. The `Hit` module that plays the main role will be described in detail in the next sub-section.

4.11.2 `Hit` Module

The `Hit` module is responsible for the formation of hits and the calculation of their coordinates. It includes peak hunting, electronic noise, and digitisation effects.

Peak Hunting When we choose the C.O.G. method for signal arrival time estimate, we have to decide how many time bins about the peak time bin to use. The peak time bin might change owing to the electric noise on each time bin. We hence need to identify the peak time bin after adding electronic noise. The peak time bin is identified by scanning the ADC values from the first time bin until the ADC value starts decreasing.

ADC Saturation Effect We used a 10-bit ADC, so the maximum ADC count is 1023. Since the pedestal value in the beam test experiment was around 100 ADC counts, the maximum ADC value after pedestal subtraction is set to 923. This effect is implemented by simply truncating the ADC value at 923 when the ADC value exceeds this maximum value.

Electronic Noise Effect In this study, we used the pedestal data from the beam test to determine the noise level. The left panel of Figure 82 shows the ADC count for each time bin for a single pedestal event. The right panel shows the distribution of ADC counts for a single pad accumulated over all the time bins for 100 pedestal events. The resultant average standard deviation of the pedestal distribution is about 0.6 ADC counts as shown in Figure 83.

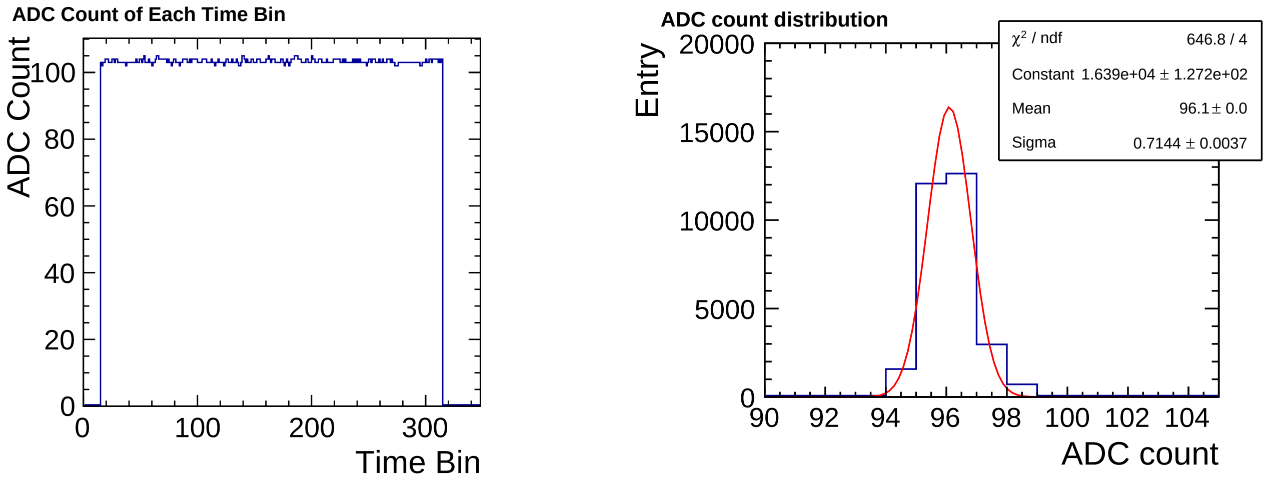

Figure 82: ADC count of each time bin from a readout pad in the central region of the end-plane readout module for a typical single event in a pedestal run (left), and the distribution of pedestal ADC counts for the same pad for the pedestal run (right).

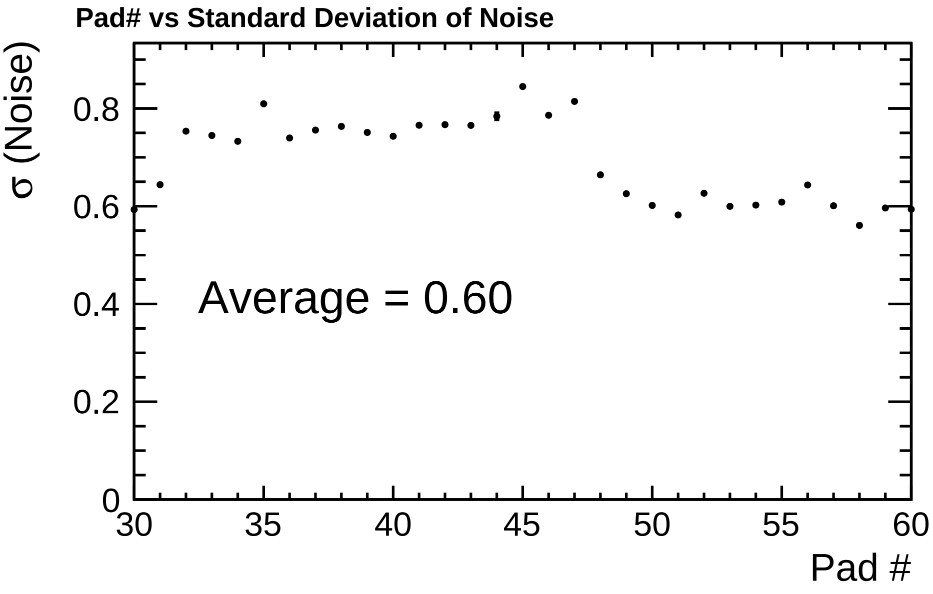

Figure 83: Standard deviation of each pad's pedestal distribution in ADC count.

4.11.3 Comparison with Beam Test Data

Using our ILD-TPC simulator, we compare the measured z resolution with simulation. We use a peaking time of 120 ns, and fixed C_{dL} at 226 $\mu\mathrm{m}/\sqrt{\mathrm{cm}}$. Three pads are used for time calculation. Figure 84 shows the result. The figure shows that the simulated slope is larger than that of the beam test data, and the measurement seems to have a larger constant term. This result implies the existence of some unknown effects which are not yet taken into account to our simulator or inappropriately implemented factors, and this should be studied in future.

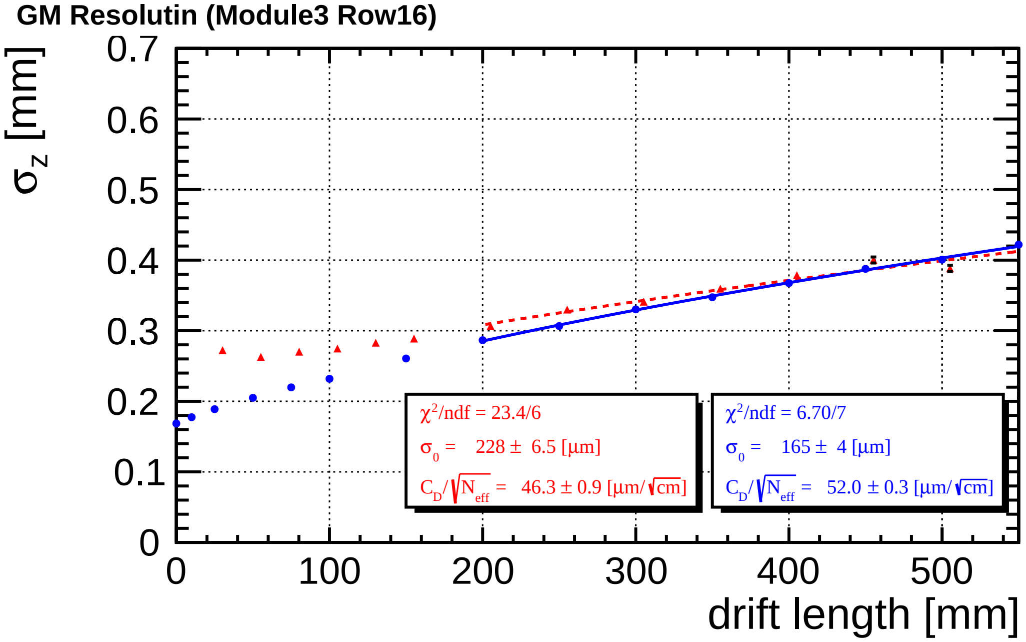

Figure 84: Comparison between simulated z resolution (blue line) and beam test z resolution (red line).

4.12 Summary of Part 2

It is important to achieve the required momentum resolution of the Higgs boson precise measurement. The momentum resolution depends on the ILD-TPC spatial resolution, and its achievement goal is to be better than 100 μm in the $r\phi$ direction and 0.4-1.4 mm in the z direction with magnetic field of 3.5 T over the full drift length.

We performed the world-first beam test of a ILD-TPC end-plane readout module with a gating device developed to prevent positive ion back-flow and evaluated its performance. The beam test was carried out at DESY, which has a large prototype of ILD-TPC. For the experiment, we used a 5 GeV electron test beam and acquired data with and without a magnetic field of 1 T. We took beam test data with and without the gating device.

For the $r\phi$ resolution, we found the following.

1. The results can be described by the analytic formula with its parameters adjusted to fit the data. The adjusted parameter values are consistent within errors with Garfield++ simulations except for the transverse diffusion constant C_{dT} measured with the gating device. The measured C_{dT} value was significantly different from expectation.

2. The difference between the data with and without the gating device was consistent with the electron transmission of the gating device.

3. The deviation and the time variation of the C_{dT} value could be attributed to some time-dependent space charge effect caused by beam intensity variation. The gates were always open during the beam test for the analysed data, which might have distorted the electric field in the drift volume due to positive ion back-flow.

4. The end-plane readout module with the gating device is expected to achieve the target $r\phi$ resolution of 100 μm at the full-drift length of 2.2 m in the 3.5 T magnetic field, if the geometry and high voltage setting of the module are properly adjusted to keep the σ_{PRF} value at 1 T.

We have also analysed the beam test data in an attempt to clarify the behaviour of the z resolution. The z resolution is clearly different between 0T and 1T, suggesting that the magnetic field affects the z resolution in some way. With regard to the z resolution, the following is shown.

1. The z resolution seems to be 796±12 μm at 1 T, suggesting that the required z resolution of 0.4-1.4 mm is achievable for the real-size ILD-TPC with the gating device.

2. There was, however, a clear difference between 1 T and 0 T data; the 1 T result was about 20% better.

3. The simulation could not reproduce the measured C_{dL} value, when estimated by assuming that the pulse shape was solely determined by shaper properties and the diffusion in the drift region, and that the shaper parameters had nominal values: $n = 3$ and $t_{pk} = 120$ ns.

4. When the t_{pk} value was adjusted to 135 ns the discrepancy went away, indicating that this method of C_{dL} estimation is rather sensitive to the input shaper parameters.

5. As an independent test we estimated C_{dL} from the drift length dependence of the z resolution and the N_{eff} estimate from that of the $r\phi$ resolution and obtained $C_{dL} = 258.9 \pm 5.7\mu\text{m}/\sqrt{\text{cm}}$.

6. This C_{dL} value obtained just above from the z resolution data is based on the analysis results using only one pad with the largest charge for the z coordinate calculation. We found that we could obtain a better z resolution if we used all the pads forming a hit for the time calculation.

7. The C_{dL} value from the z resolution analysis using all the pads is $229.2 \pm 5.6\mu\text{m}/\sqrt{\text{cm}}$, consistent with the Garfield++ simulation.

5 Summary & Conclusion

The precise measurements of the Higgs couplings play an essential role in discovering BSM. For the measurements of the $h\gamma\gamma$ and $h\gamma Z$ couplings, we performed the world-first full simulation study of the $e^+e^- \to h\gamma$ process at the ILC. The precision Higgs measurements require a precision charged particle tracking system. For the central ILD tracker, we constructed and tested a ILD-TPC end-plane readout module with a gating device.

Our full detector simulation using a realistic detailed model of the ILD showed that the observation of the $e^+e^- \to h\gamma$ process is much more difficult than originally expected unless there is some significant BSM effect. We hence estimated the upper limit on the $h\gamma$ production cross section by combining the results for the $h \to b\bar{b}$ and $h \to WW^*$ semi-leptonic channels, and found 95% C.L. upper limits: $\frac{\sigma^L_{h\gamma}}{\sigma^L_{SM}} < 5.0$, and $\frac{\sigma^R_{h\gamma}}{\sigma^R_{SM}} < 61.9$ for purely left- and right-handed polarisations, respectively. The implication of the upper limits was discussed first using the EFT framework together with the SM one-loop amplitudes. The 95% C.L. upper limits were translated into the corresponding limits on the EFT coefficients ζ_{AZ} and ζ_A. The resultant constraints on ζ_{AZ} and ζ_A turned out to be rather weak compared to those expected at HL-LHC.

We carried out the world-first beam test of a ILD-TPC end-plane readout module with a gating device. The result of the analysis of beam test data suggests that the target resolutions, better than 100μm in the $r\phi$ and 0.4-1.4 mm in the z directions with magnetic field of 3.5 T over the full drift length, can be achieved with a full-size ILD-TPC. We developed a new method to estimate C_{dL} by analysing the pulse shape. We also improved the time calculation method for z coordinate estimation. In the course of this study, we found some issues such as unexpected C_{dT} variation during the experiment that should be studied in future. In order to clarify the factors which affect the z resolution, the development of a simulator that accurately reproduces the behaviour of z resolution is in progress.

6 Appendix

A. Calculation of Cross Section of $e^+e^- \to h\gamma$ with Yukawa Coupling

We can express the momentum of $e^-(P_-)$, and the momentum of $e^+(P_+)$

$$\begin{aligned} P_+ &= k - r && \text{(A.1)} \\ P_- &= k + q. && \text{(A.2)} \end{aligned}$$

where k is the momentum of photon, r and q are momentum moving through the propagator for u- and t-channel electron exchange, respectively.

$$q = P_- - k \to q^2 = (P_- - k)^2 = p_-^2 + k^2 - 2p_-k. \tag{A.3}$$

Note that,

$$\begin{aligned} P_-^2 &= m_e^2, \quad k^2 = 0 && \text{(A.4)} \\ q^2 &= t && \text{(A.5)} \\ r &= k - P_+ \to r^2 = u = -2P_+k && \text{(A.6)} \end{aligned}$$

$$\mu = \langle h\gamma| \int\int \mathcal{L}_i^{Yukawa}(x_1)\mathcal{L}_i^{QED}(x_2)|e^+e^-\rangle \tag{A.7}$$

$$\begin{aligned} \mathcal{L}_i^{Yukawa} &= \frac{m_e}{v}\bar{\psi}\psi h. && \text{(A.8)} \\ \mathcal{L}_i^{QED} &= -e\left(\bar{\psi}\gamma^\mu\right)\psi A_\mu. && \text{(A.9)} \end{aligned}$$

Operator h in $\mathcal{L}_i^{Yukawa}$ generates a Higgs boson from vacuum. This can be expressed as $\langle h|h|0\rangle$. The momentum space wave function of the Higgs boson from this is equal to 1. Operator A_μ in $\mathcal{L}_i^{QED}$ generates a photon from vacuum.

$$\langle \gamma\,|A_\mu|\,0\rangle = \varepsilon_\mu^*(\lambda)e^{ikx}. \tag{A.10}$$

And ψ in $\mathcal{L}_i^{QED}$ or $\mathcal{L}_i^{Yukawa}$ put e^- out, and $\bar{\psi}$ put e^+ out

$$\begin{aligned} \left\langle 0|\psi|e^-\right\rangle &= ue^{-ip_-x} && \text{(A.11)} \\ \langle 0|\bar{\psi}|e^+\rangle &= ve^{-ip_+x} && \text{(A.12)} \end{aligned}$$

However,the exponential factors vanish when we integrate over x to produce a delta function describing the 4-momentum conservation.

$$e^{i\left(\sum P_f - \sum p_i\right)x} \tag{A.13}$$

$$\int e^{ikx}dx = 2\pi\delta(k). \tag{A.14}$$

So, the momentum-space electron and positron wave functions are u, v, respectively. Remaining part of the t-channel amplitude will be

$$\langle 0|T_p[\psi\overline{\psi}]|0\rangle = \frac{1}{\not{q} - m_e}, \tag{A.15}$$

where T_p is the time ordered product. Then, the amplitude is given by

$$\begin{aligned} T_1 &= \bar{v}(p_+, s_+)(\frac{m_e}{v})\frac{1}{q - m_e}\left(-e\gamma^\mu\right)u\left(p_-, s_-\right).\epsilon_\mu(\lambda) \\ &= \left(\frac{m_e}{v}\right)(-e)\left(\frac{1}{q^2 - m_e^2}\right)\bar{v}\left(p_+, s_+\right)\left(\not{q} + m_e\right)\gamma^\mu u(p_-, s_-)\epsilon_\mu(\lambda). \end{aligned} \tag{A.16}$$

Note that $\not{q} = q_\alpha\gamma^\alpha$, so

$$\begin{aligned} \frac{1}{\not{q} - m_e} &= \frac{1}{\not{q} - m_e}\cdot\frac{1}{\not{q} + m_e}\left(\not{q} + m_e\right) && \text{(A.17)} \\ \not{q}^2 = q^2 I &= \frac{1}{q^2 - m_e^2}\left(\not{q} + m_e\right)I. && \text{(A.18)} \end{aligned}$$

Similarly, the u-channel amplitude is given by,

$$T_2 = \left(\frac{m_e}{v}\right)(-e)\left(\frac{1}{r^2 - m_e^2}\right)\bar{v}\left(p_+, s_+\right)\gamma^\nu\left(\not{r} + m_e\right)u\left(p_-, s_-\right)\epsilon_\nu(\lambda). \tag{A.19}$$

Let $\frac{1}{q^2 - m_e^2}$ be D_t and $\frac{1}{r^2 - m_e^2}$ be D_u.

$$\begin{aligned} \left|T_1 + T_2\right|^2 &= \left(T_1 + T_2\right)^\dagger\left(T_1 + T_2\right) \\ &= T_1^\dagger T_1 + M_1^\dagger T_2 + T_2^\dagger T_1 + T_2^\dagger T_2. \end{aligned} \tag{A.20}$$

$$\begin{aligned} T_1^\dagger T_1 &= \left(\frac{m_e}{v}\right)^2 e^2[D_t^2 u^\dagger \gamma^{\mu\dagger}\, \not{q}^\dagger (v^\dagger \gamma^0)^\dagger \bar{v}\, \not{q}\gamma^\nu u \epsilon_\nu(\lambda)\epsilon_\mu^*(\lambda)] \\ &= \left(\frac{m_e}{v}\right)^2 e^2[D_t^2 u^\dagger \gamma^0\gamma^0\gamma^{\mu\dagger}\gamma^0\gamma^0\, \not{q}^\dagger \gamma^{0\dagger} v\bar{v}\, \not{q}\gamma^\nu u \epsilon_\nu(\lambda)\epsilon_\mu^*(\lambda)], \end{aligned} \tag{A.21}$$

where we have ignored the m_e^2 term because it is small.

$$T_1^\dagger T_1 = \left(\frac{m_e}{v}\right)^2 e^2[D_t^2 \bar{u}\gamma^\mu\, \not{q} v\bar{v}\, \not{q}\gamma^\nu u \epsilon_\nu(\lambda)\epsilon_\mu^*(\lambda)] \tag{A.22}$$

$$\begin{aligned} \sum_{s^+,s^-,\lambda} T_1^\dagger T_1 &= \left(\frac{m_e}{v}\right)^2 e^2 D_t^2 = \sum_{s^+ s^-} \bar{u}\gamma^\mu\, \not{q} v\bar{v}\, \not{q}\gamma^\nu u \sum_\lambda \epsilon_\nu(\lambda)\epsilon_\mu^*(\lambda) \\ &= \left(\frac{m_e}{2}\right)^2 e^2 D_t^2 Tr(\sum_{s-} u\bar{u}\gamma^\mu\, \not{q} \sum_{s+} v\bar{v}\, \not{q}\gamma^\nu) \sum_\lambda \epsilon_\nu\epsilon_\mu^*. \end{aligned} \tag{A.23}$$

$$\sum_{s-} u\bar{u} = (\not{P}_- + m_e) \tag{A.24}$$

$$\sum_{s+} v\bar{v} = (\not{P}_+ - m_e) \tag{A.25}$$

$$\sum_\lambda \epsilon_\nu\epsilon_\mu^* = -g_{\nu\mu}. \tag{A.26}$$

$$\begin{aligned} \sum_{s^+,s^-,\lambda} T_1^\dagger T_1 &= \left(\frac{m_e}{v}\right)^2 e^2 D_t^2 Tr\,(\not{P}_-\gamma^\mu\, \not{q}\not{P}_+\gamma^\nu)\,(-g_{\nu\mu}) \\ &= -\left(\frac{m_e}{v}\right)^2 e^2 D_t^2 Tr\,(\not{P}_-\gamma^\mu\, \not{q}\not{P}_+\gamma^\nu)\,(-g_{\nu\mu})\,. \end{aligned} \tag{A.27}$$

$$\begin{aligned} \gamma^\mu\gamma^\rho\gamma^\sigma\gamma^\delta\gamma_\mu &= (-\gamma^\rho\gamma^\mu + 2g^{\mu\rho})\,\gamma^\sigma\gamma^\delta\gamma_\mu \\ &= -\gamma^\rho\gamma^\mu\gamma^\sigma\gamma^\delta\gamma_\mu + 2\gamma^\sigma\gamma^\delta\gamma^\rho \\ &= -\gamma^\rho\,(-\gamma^\sigma\gamma^\mu + 2g^{\sigma\mu})\,\gamma^\delta\gamma_\mu + 2\gamma^\sigma\gamma^\delta\gamma^\rho \\ &= \gamma^\rho\gamma^\sigma\gamma^\mu\gamma^\delta\gamma_\mu - 2\gamma^\rho\gamma^\delta\gamma^\sigma + 2\gamma^\sigma\gamma^\delta\gamma^\rho \\ &= \gamma^\rho\gamma^\sigma\left(-\gamma^\delta\gamma^\mu + 2g^{\mu\delta}\right) - 2\gamma^\rho\gamma^\delta\gamma^\sigma + 2\gamma^\sigma\gamma^\delta\gamma^\rho \\ &= -\gamma^\rho\gamma^\sigma\gamma^\delta\gamma^\mu\gamma_\mu + 2\gamma^\rho\gamma^\sigma\gamma^\delta - 2\gamma^\rho\gamma^\delta\gamma^\sigma + 2\gamma^\sigma\gamma^\delta\gamma^\rho \\ &= -2\gamma^\rho\gamma^\sigma\gamma^\delta - 2\gamma^\rho\gamma^\delta\gamma^\sigma + 2\gamma^\sigma\gamma^\delta\gamma^\rho, \end{aligned} \tag{A.28}$$

where,

$$\begin{aligned} 2\gamma^\sigma\gamma^\delta\gamma^\rho &= 2\left(-\gamma^\delta\gamma^\sigma + 2g^{\delta\sigma}\right)\gamma^\rho \\ &= -2\gamma^\rho\left\{\gamma^\sigma,\gamma^\delta\right\} \\ &\quad \left\{\gamma^\sigma,\gamma^\delta\right\} = 2g^{\sigma\delta} \\ &= -2\gamma^\delta\gamma^\sigma\gamma^\rho \end{aligned} \tag{A.29}$$

Therefore,

$$\gamma^\mu\gamma^\rho\gamma^\sigma\gamma^\delta\gamma_\mu = -2\gamma^\delta\gamma^\sigma\gamma^\rho. \tag{A.30}$$

$$\begin{aligned} \sum_{s^+,s^-,\lambda} T_1^\dagger T_1 &= 2\left(\frac{m_p}{v}\right)^2 e^2 D_t^2 \,\mathrm{Tr}(\not{P}_- \not{q} \not{P}_+ \not{q}) \\ &= 2\left(\frac{m_p}{v}\right)^2 e^2 D_t^2 \cdot 4\left(2(P_-q)(P_+q) - (P_-P_+)\left(q\cdot q\right)\right) \end{aligned} \tag{A.31}$$

$P_-q = -(P_-k) = \frac{t}{2}$, $p_+q = \frac{s}{2} + \frac{u}{2}$, $P_-P_+ = \frac{S}{2}$, $q \cdot q = u$. Therefore,$4((t+s)\frac{u}{2} - \frac{s}{2}u = 2tu$

$$\sum_{s^+,s^-,\lambda} T_1^\dagger T_1 = 4\left(\frac{m_e}{2}\right)^2 e^2 D_t^2 tu \tag{A.32}$$

Similarly,

$$\begin{aligned} \sum_{s^+,s^-,\lambda} T_2^\dagger T_2 &= \left(\frac{m_e}{v}\right)^2 e^2 D_u^2 \sum_{s^2,s^-} \bar{u}\ \not{r}\gamma^\mu v\bar{v}\gamma_\nu\ \not{r}u \sum_\lambda \epsilon_\nu\epsilon_\mu^* \\ &= -\left(\frac{m_e}{v}\right)^2 e^2 D_u^2 \,\mathrm{Tr}(\not{P}_-\ \not{r}\gamma^\mu\ \not{P}_+\gamma_\mu\ \not{r}) \\ &= 2\left(\frac{m_e}{v}\right)^2 e^2 D_u^2 \,\mathrm{Tr}(\not{P}_-\ \not{r}\ \not{P}_+\ \not{r}) \\ &= \left(\frac{m_e}{v}\right)^2 e^2 D_u^2 \cdot 4\left(2(P_-r)(p_+r) - (P_-P_+)\left(r\cdot r\right)\right). \end{aligned} \tag{A.33}$$

$P_-r = -\frac{t}{2} - \frac{S}{2}$, $p_+r = (P_+k) = -\frac{u}{2}$, $P_-P_+ = \frac{S}{2}$, $r \cdot r = u$. Therefore $4((t+s)\frac{u}{2} - \frac{s}{2}u = 2tu$.

$$\sum_{s^+,s^-,\lambda} T_2^\dagger T_2 = 4\left(\frac{m_e}{2}\right)^2 e^2 D_u^2 tu \tag{A.34}$$

$$\begin{aligned}
\sum_{s^+,s^-,\lambda} T_1^\dagger T_2 &= \left(\frac{m_e}{v}\right)^2 e^2 D_t D_u \sum_{s^+,s^-} \bar{u}\gamma^\mu \not{q} v\bar{v}\gamma^\nu \not{r} u \sum_\lambda \epsilon_\mu(\lambda)\epsilon^*_\mu(\lambda) \\
&= \left(\frac{m_e}{v}\right)^2 e^2 D_t D_u Tr \left(\sum_{s^-} u\bar{u}\gamma^\mu \not{q} \sum_{s^+} v\bar{v}\gamma^\nu \not{r}\right) \sum_\lambda \epsilon_\nu \epsilon^*_\mu \\
&= \left(\frac{m_e}{v}\right)^2 e^2 D_t D_u Tr\left(\not{P}_-\gamma^\mu \not{q} \not{P}_+\gamma^\nu \not{r}\right)\left(g_{\nu\mu}\right) \\
&= -\left(\frac{m_e}{v}\right)^2 e^2 D_t D_u Tr\left(\not{P}_-\gamma^\mu \not{q} \not{P}_+\gamma_\mu \not{r}\right) \\
&= -4\left(\frac{m_e}{v}\right)^2 e^2 D_t D_u \left(q\cdot P_+\right) \mathrm{Tr}(\not{P}_- \not{r}). \qquad \text{(A.35)}
\end{aligned}$$

where, $\gamma^\mu \not{a} \not{b}\gamma_\mu = 4(a\cdot b)$.

$$\sum_{s^+,s^-,\lambda} T_1^\dagger T_2 = -16\left(\frac{m_e}{v}\right)^2 e^2 D_t D_u [(P_+P_-) - (P_+k)][(P_-k) - (P_-P_+)], \qquad \text{(A.36)}$$

where $(P_+P_-) - (P_+k) = \frac{s}{2} + \frac{u}{2}$, $(P_-k) - (P_-P_+) = -\frac{t}{2} - \frac{s}{2}$

$$\begin{aligned}
\sum_{s^+,s^-,\lambda} T_1^\dagger T_2 &= 16\left(\frac{m_e}{v}\right)^2 e^2 D_t D_u \left(\frac{s+u}{2}\right)\left(\frac{s+t}{2}\right) \\
&= 4\left(\frac{m_e}{v}\right)^2 e^2 D_t D_u \left(s+u\right)\left(s+t\right). \qquad \text{(A.37)}
\end{aligned}$$

$\sum_{s^+,s^-,\lambda} M_2^\dagger M_1$ is complex conjugate of $\sum_{s^+,s^-,\lambda} M_1^\dagger M_2$. Finally,

$$\begin{aligned}
\sum |T_1 + T_2|^2 &= 4\left(\frac{m_e}{v}\right)^2 e^2 \left[D_t^2 tu + 2D_t D_u (s+t)\left(s+u\right) + D_u^2 tu\right] \\
&= 4\left(\frac{m_e}{v}\right)^2 e^2 [\mathrm{tu}\left(D_t + D_u\right)^2 + 2s(s+t+u)D_t D_u]. \qquad \text{(A.38)}
\end{aligned}$$

since $(s+t+u) = m_h^2$,

$$\begin{aligned}
\sum |T_1+T_2|^2 &= 4\left(\frac{m_e}{v}\right)^2 e^2[\mathrm{tu}\,(D_t+D_u)^2 + 2sm_h^2 D_t D_u] \\
&= 4e^2\left(\frac{m_e}{v}\right)^2 D_t D_u\left[tu\left(t+u-2m_e^2\right)^2 D_t D_u + 2m_h^2 s\right] \\
&= 4e^2\left(\frac{m_e}{v}\right)^2 D_t D_u\left[tu\left(s-m_h^2\right)^2 D_t D_u + 2m_h^2 s\right] \\
&= 4e^2\left(\frac{m_e}{v}\right)^2 D_t D_u s^2\left[\left(1-\frac{m_h^2}{s}\right)^2 tu D_t D_u + 2\left(\frac{m_h^2}{s}\right)\right]. \qquad \text{(A.39)}
\end{aligned}$$

$$\begin{aligned}
|T_1+T_2|^2_{LR} &= |T_1+T_2|^2_{RL} \simeq 0 \qquad \text{(A.40)} \\
|T_1+T_2|^2_{LL} &= |T_1+T_2|^2_{RR} \simeq \frac{1}{2}\sum |T_1+T_2|^2 \\
&\simeq 2e^2\left(\frac{m_e}{v}\right)^2 D_t D_u s^2\left[\left(1-\frac{m_h^2}{s}\right)^2 tu D_t D_u + 2\left(\frac{m_h^2}{s}\right)\right] \qquad \text{(A.41)}
\end{aligned}$$

$$\begin{aligned}
d\sigma_{LL} &= d\sigma_{RR} = \frac{1}{2s\beta_e}\left(\frac{1}{2}\sum \mid M_1+M_2|^2\right) d\Phi_2 \\
&= \frac{1}{2s\beta_e}\frac{1}{2}\sum \mid M_1+M_2|^2 \frac{\bar{\beta}}{8\pi}\frac{d\Omega}{4\pi}. \qquad \text{(A.42)}
\end{aligned}$$

Because $d\Phi_2 = \frac{\bar{\beta}}{8\pi}\frac{d\Omega}{4\pi}$.

$$\frac{d\sigma_{LL}}{d\cos\theta} = \frac{d\sigma_{RR}}{d\cos\theta} = \frac{1}{2s\beta_e}2e^2\left(\frac{m_e}{v}\right)^2 D_t D_u s^2\left[\left(1-\frac{m_h^2}{s}\right)^2 tu D_t D_u + 2\left(\frac{m_h^2}{s}\right)\right]\frac{\bar{\beta}}{16\pi}. \qquad \text{(A.43)}$$

B. Expected Longitudinal Diffusion Constant

The longitudinal diffusion constant C_{dL} was simulated by Garfield++ at 0 T and 1 T, respectively. The temperature and pressure at the beginning of the data taking were used as corrections in the simulation. The input values and results are summarised in Figure B.1.

Table B.1: Input values and result of Garfield++ simulation.

	1 T	0 T
Temperature[K]	291.28	291.11
Pressure[hPa]	1010.79	1007.29
$C_{dL}[\mu\text{m}/\sqrt{\text{cm}}]$	226.1 ± 3.5	224.4 ± 6.0

The results show that the longitudinal diffusion constants C_{dL} agree within error for magnetic fields of 0 T and 1 T.

C. Problem in the Current Pulse Processing

In the course of our pulse shape study we found a problem that there the fitting error became very large in the beginning part the pulse (see Figure C.1). This is caused by ADC data having negative values after pedestal subtraction are truncated to zero during data acquisition with the ALTRO DAQ system. The negative ADC values are due to the induction signal generated by electrons moving from the GEM foil to the side anode pads. If the negative ADC values are truncated, only the positive tail of a Gaussian can be seen thereby causing the large errors. It is therefore desirable to avoid this truncation and store all information.

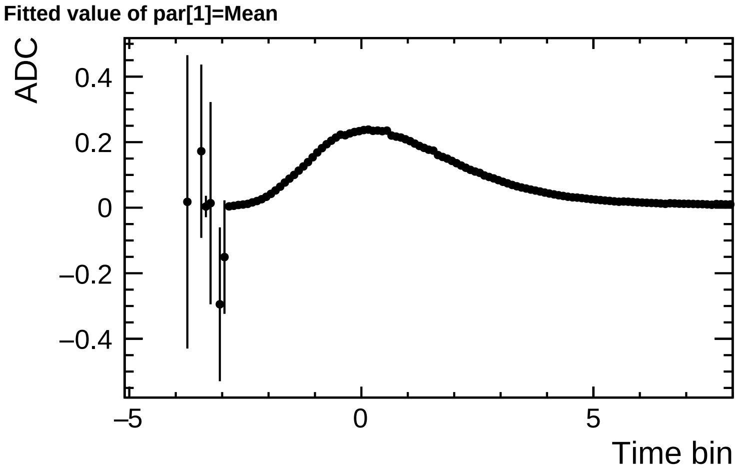

Figure C.1: Projection of pulse of beam test data.

D. Row Dependence of z residual

Figure D.1 shows the z residual for each row at 1 T. A similar trend is observed for each row at 0 T, suggesting some distortion of isochrones. This may be caused by the deformation of the GEM foil, its electrode gaps, and so on, though the reason has not yet been identified.

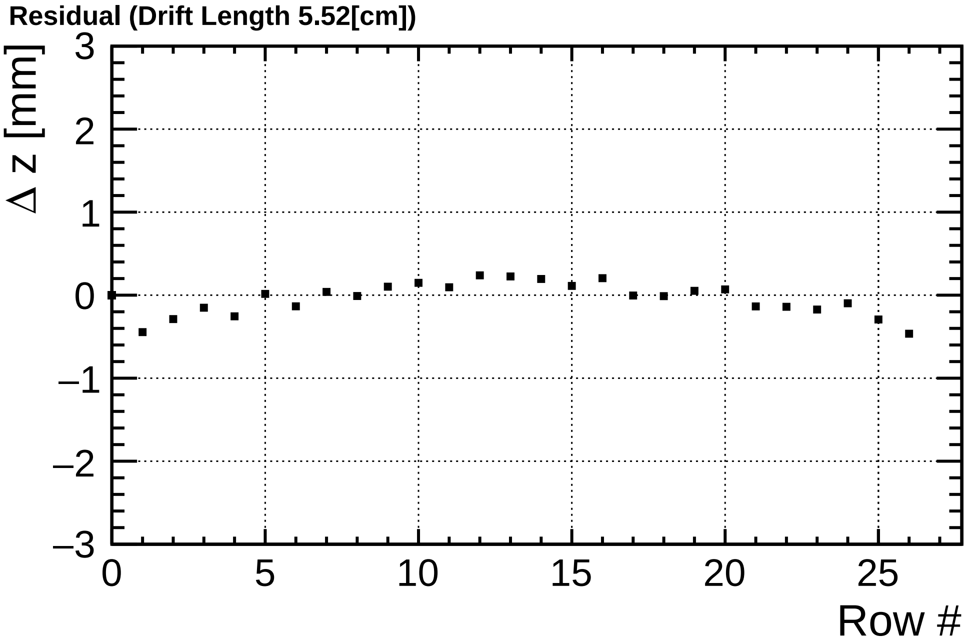

Figure D.1: z residual of nominal 1 T data.

E. Row Dependence of C_{dT}

Figure E.1 shows the C_{dT} for each row at 1 T. Apparently the estimated C_{dT} varies with the row number. The size of the variation is larger than that expected from possible electric field distortion due to the geometry imperfection. On the other hand, there seems to be a discontinuity from row 13 to row 14, where the pad pitch changes suddenly. This suggests that the apparent C_{dT} variation has something to do with our method (see section 1.9.3) to measure the $\sigma_{PR}(z)$. This has to be further studied in future.

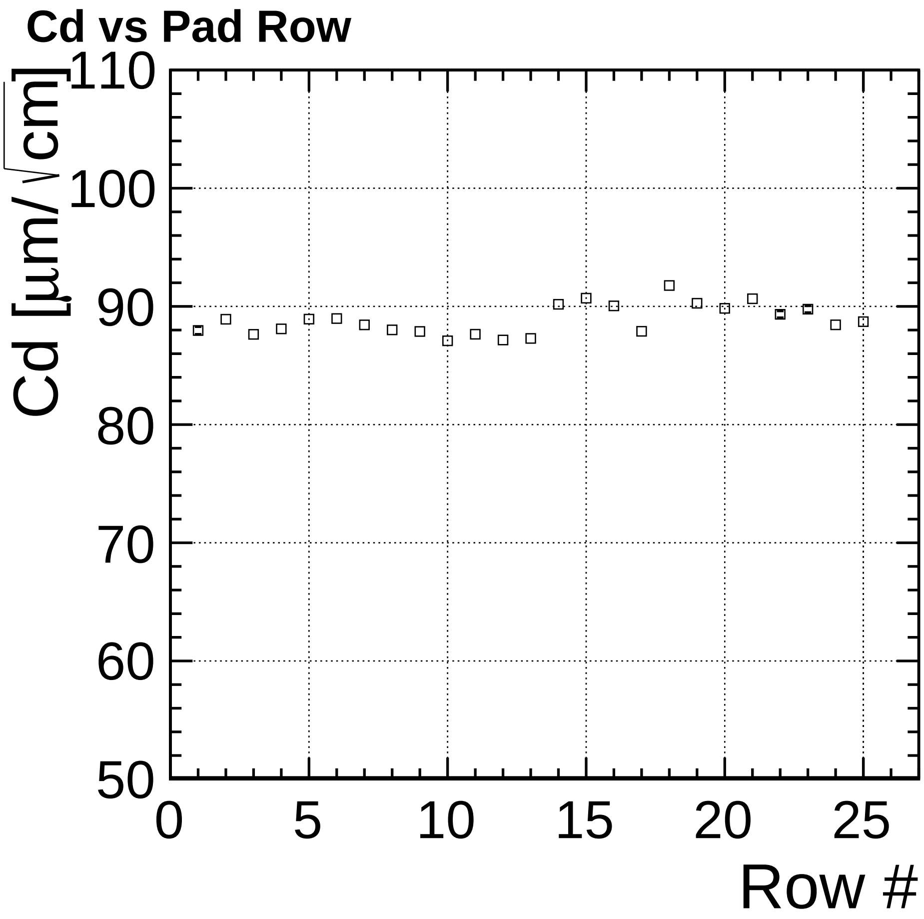

Figure E.1: z residual of nominal 1T data.

Acknowledgements

This work was carried out as part of the ILC R&D programme from 2012 to 2021, and I would like to express my deepest gratitude to all members of the ILC Physics Subgroup and all members of the LC-TPC group. I would like to thank the LCC Generator Working Group and the ILD Software Working Group for providing the simulation and reconstruction tools and producing the Monte-Carlos samples used in this work. This work is supported in part by the Japan Society for the Promotion of Science under the Grants-in-Aid for Science Research 16H0217.

In particular, I cannot thank enough Prof. FUJII Keisuke, my supervisor for four years, who patiently guided me for in total of six years. It is a fact that without his guidance, this research would not have been possible. I would also like to thank Prof. Daniel Jeans, my supervisor for later two years. Prof. KOBAYASHI Makoto guided my TPC research. Prof. Junping Tian helped me throughout the simulation study of the $e^+e^- \to h\gamma$ process. I would also like to thank the following physicists who were essential to this work: Prof. YOKOYA Hiroshi, Prof. Sunghoon Jung, Prof. Junghwan Lee who provided the SM 1-loop calculation for the $e^+e^- \to h\gamma$ process.

I am also grateful to members of the LCTPC group for their help with the beam tests in 2016, especially to the DESY members for their dedication and support. I am also thankful to Dr. OGAWA Tomohisa, Ms. SHOJI Aiko, Dr. Jacqueline Yan, Dr. YONAMINE Ryo, Dr. KAWADA Shin-ichi for guiding me since my master's degree.

I am also grateful to Mr. MIZUNO Takahiro, Mr. YUMINO Keita, and Ms. NAKAJIMA Jurina for the opportunity to study with them. I am also happy to have had a good student life with other KEK students. I would also like to thank the secretaries of the ILC group at KEK, Mrs. OHATA Hisako and Mrs. KUSAMA Hitomi, and the KEK SOKENDAI office staff for their kindness and support in my student life. I would also like to express my gratitude to the KEK mechanical centre, the KEK accelerator Group, and the detector group for their support in my research and study.

I would like to thank Mr. TAKAHASHI Shota and other members of the KEK Public Relations Office, Mrs. TAKAHASHI Rika, Mrs. KOBAYASHI Nobuko, Mrs. KIKUCHI Mako and other members of the ILC Promotion Office, for their cooperation for outreach activity. I also thank the people of Ichinoseki City, Iwate Prefecture, which is a candidate site for ILC construction.

I would also like to thank Tsukuba Place Lab and its staff members, especially Mr. HORISHITA Kyohei and Ms. KANEKO Haruka, Ms. EMOTO Juri from up Tsukuba, and other local people, for providing me with a place to work and refresh myself during my student life in Tsukuba.

I would also like to thank ISHIKAWA Hanami for providing beautiful illustrations for my paper.

Finally, I would like to thank my family, AOKI Yoshi-Shige, AOKI Yoko and AOKI

Megumi, who have supported me over the years.

References

[1] Shinya Kanemura, Kentarou Mawatari, and Kodai Sakurai. Single Higgs production in association with a photon at electron-positron colliders in extended Higgs models. *Phys. Rev. D*, 99:035023, Feb 2019. `https://link.aps.org/doi/10.1103/PhysRevD.99.035023`.

[2] S. Agostinelli et.al. Geant4—a simulation toolkit. *Nuclear Instruments and Methods in Physics Research Section A: Accelerators, Spectrometers, Detectors and Associated Equipment*, 506(3):250–303, 2003. `https://www.sciencedirect.com/science/article/pii/S0168900203013688`.

[3] R Yonamine, K Fujii, K Ikematsu, A Ishikawa, T Fusayasu, P Gros, Y Kato, S Kawada, M Kobayashi, T Matsuda, O Nitoh, R D Settles, A Sugiyama, T Takahashi, J Tian, and T Watanabe. Spatial resolutions of GEM TPC. A novel theoretical formula and its comparison to latest beam test data. *Journal of Instrumentation*, JINST(9):C03002, 2014. `https://iopscience.iop.org/article/10.1088/1748-0221/9/03/C03002`.

[4] TikZ by Carsten Burgard. `https://texample.net/tikz/examples/model-physics/`.

[5] Chatrchyan, V. Khachatryan, and A.M. Sirunyan et al. Observation of a new boson at a mass of 125 GeV with the CMS experiment at the LHC. *Physics Letters B*, 716(1):30–61, 2012. `https://www.sciencedirect.com/science/article/pii/S0370269312008581`.

[6] G. Aad, T. Abajyan, and B. Abbott et al. Observation of a new particle in the search for the Standard Model Higgs boson with the ATLAS detector at the LHC. *Physics Letters B*, 716(1):1–29, 2012. `https://www.sciencedirect.com/science/article/pii/S037026931200857X`.

[7] FUJII Keisuke. Private Communication.

[8] Howard Baer, Tim Barklow, Keisuke Fujii, Yuanning Gao, Andre Hoang, Shinya Kanemura, Jenny List, Heather E. Logan, Andrei Nomerotski, Maxim Perelstein, Michael E. Peskin, Roman Pöschl, Jürgen Reuter, Sabine Riemann, Aurore Savoy-Navarro, Geraldine Servant, Tim M. P. Tait, and Jaehoon Yu. The international linear collider technical design report - volume 2: Physics, 2013.

[9] The ILD Collaboration. International Large Detector: Interim Design Report, 2020. `https://arxiv.org/abs/2003.01116`.

[10] Tim Barklow, Keisuke Fujii, Sunghoon Jung, Michael E. Peskin, and Junping Tian. Model-independent determination of the triple Higgs coupling at e^+e^- colliders. *Physical Review D*, 97(5), Mar 2018. `http://dx.doi.org/10.1103/PhysRevD.97.053004`.

[11] AAA ILC PROJECT HP. http://ilcgallery.com/.

[12] Ties Behnke, James E. Brau, Philip N. Burrows, Juan Fuster, Michael Peskin, Marcel Stanitzki, Yasuhiro Sugimoto, Sakue Yamada, and Hitoshi Yamamoto. The International Linear Collider Technical Design Report - Volume 4: Detectors, 2013. https://arxiv.org/abs/1306.6329.

[13] James Brau, Yasuhiro Okada, Nicholas J Walker, Abdelhak Djouadi, Joseph Lykken, Klaus Monig, Mark Oreglia, Satoru Yamashita, Nan Phinney, Nobukazu Toge, Ties Behnke, Chris Damerell, John Jaros, and Akiya Miyamoto. *International Linear Collider reference design report: ILC Global Design Effort and World Wide Study*. CERN Yellow Reports: Monographs. CERN, Geneva, 2007. https://cds.cern.ch/record/1061261.

[14] Cao Qing-Hong, Wang Hao-Ran, and Zhang Ya. Probing HZγ and H$\gamma\gamma$ anomalous couplings in the process $e^+e^- \to H\gamma$. *Chinese Physics C*, 39(11):113102, 2015. https://iopscience.iop.org/article/10.1088/1674-1137/39/11/113102.

[15] Mehmet Demirci. Associated production of higgs boson with a photon at electron-positron colliders. *Phys. Rev. D*, 100:075006, Oct 2019. https://link.aps.org/doi/10.1103/PhysRevD.100.075006.

[16] Calculated by H. YOKOYA. Private Communication.

[17] Physsim home page. http://www-jlc.kek.jp/subg/offl/physsim/.

[18] Wolfgang Kilian, Thorsten Ohl, and Jürgen Reuter. WHIZARD—simulating multi-particle processes at LHC and ILC. *The European Physical Journal C*, 71(9):1–29, 2011. https://link.springer.com/article/10.1140/epjc/s10052-011-1742-y.

[19] P Mora De Freitas and Henri Videau. Detector simulation with MOKKA/GEANT4: Present and future. In *International Workshop on Linear Colliders (LCWS 2002), Jeju Island, Korea*, pages 26–30, 2002. https://s3.cern.ch/inspire-prod-files-a/adc863c5fc149c8bce03ef0a84f8cf48.

[20] F Gaede and J et al. Engels. Marlin-A Software Framework for ILC detector R&D. *EUDET-Report-2007-11*, 2007. https://www.eudet.org/e26/e27/e584/eudet-report-2007-11.pdf.

[21] MA Thomson. Particle flow calorimetry and the PandoraPFA algorithm. *Nuclear Instruments and Methods in Physics Research Section A: Accelerators, Spectrometers, Detectors and Associated Equipment*, 611(1):25–40, 2009. https://www.eudet.org/e26/e27/e584/eudet-report-2007-11.pdf.

[22] Taikan Suehara and Tomohiko Tanabe. LCFIPlus: A framework for jet analysis in linear collider studies. *Nuclear Instruments and Methods in Physics Research Section A: Accelerators, Spectrometers, Detectors and Associated Equipment*, 808:109–116, 2016.

[23] Philip Bambade, Tim Barklow, Ties Behnke, Mikael Berggren, James Brau, Philip Burrows, Dmitri Denisov, Angeles Faus-Golfe, Brian Foster, Keisuke Fujii, Juan Fuster, Frank Gaede, Paul Grannis, Christophe Grojean, Andrew Hutton, Benno List, Jenny List, Shinichiro Michizono, Akiya Miyamoto, Olivier Napoly, Michael Peskin, Roman Poeschl, Frank Simon, Jan Strube, Junping Tian, Maksym Titov, Marcel Vos, Andrew White, Graham Wilson, Akira Yamamoto, Hitoshi Yamamoto, and Kaoru Yokoya. The International Linear Collider: A Global Project, 2019. `https://arxiv.org/abs/1903.01629`.

[24] S. Catani, Yu.L. Dokshitzer, M. Olsson, G. Turnock, and B.R. Webber. New clustering algorithm for multijet cross sections in e^+e^- annihilation. *Physics Letters B*, 269(3):432–438, 1991.

[25] Andreas Hoecker, Peter Speckmayer, Joerg Stelzer, Jan Therhaag, Eckhard von Toerne, Helge Voss, M Backes, T Carli, O Cohen, A Christov, et al. TMVA-toolkit for multivariate data analysis. *arXiv preprint physics/0703039*, 2007. `https://arxiv.org/abs/physics/0703039`.

[26] Junping Tian. A new method for measuring the Higgs mass at the ILC. Technical report, ILD-PHYSPUB-2019-001, 2020. `https://confluence.desy.de/display/ILD/ILD+notes?preview=/42357928/153507787/ILD-PHYS-PUB-2019-001.pdf`.

[27] Junping Tian, Keisuke Fujii, and Hiroshi Yokoya. Diphoton resonances at the ILC. *Phys. Rev. D*, 94:095015, Nov 2016. `https://link.aps.org/doi/10.1103/PhysRevD.94.095015`.

[28] The ATLAS Collaboration. Measurement of the properties of Higgs boson production at $\sqrt{s} = 13$ TeV in the $H \to \gamma\gamma$ channel using 139 fb^{-1} of pp collision data with the ATLAS experiment. `https://cds.cern.ch/record/2725727/files/ATLAS-CONF-2020-026.pdf`, 2020.

[29] The CMS Collaboration. Search for the Higgs boson decay to $Z\gamma$ in proton-proton collisions at $\sqrt{s} = 13$ TeV. *CMS-PAS-HIG-19-014*, page 10, 2021. `https://cds.cern.ch/record/2784454`.

[30] The ATLAS Collaboration. Projections for measurements of Higgs boson cross sections, branching ratios, coupling parameters and mass with the ATLAS detector at the HL-LHC. *ATL-PHYS-PUB-2018-054*, page 36, 2018. `https://atlas.web.cern.ch/Atlas/GROUPS/PHYSICS/PUBNOTES/ATL-PHYS-PUB-2018-054/`.

[31] Physsim home page. `http://www-jlc.kek.jp/subg/offl/physsim/`.

[32] F. Sauli, L. Ropelewski, and P. Everaerts. Ion feedback suppression in time projection chambers. *Nuclear Inst. and Methods in Physics Research, A*, 560(2):269–277, 2006. `https://www.infona.pl/resource/bwmeta1.element.elsevier-1ca29b1c-f12c-3c92-84a8-e7e3f3bcb1b4`.

[33] R. L. Glückstern. Uncertainties in track momentum and direction, due to multiple scattering and measurement errors. *Nuclear Instruments and Methods*, 24:381–389, July 1963. `https://www.sciencedirect.com/science/article/pii/0029554X63903471`.

[34] M. Kobayashi, R. Yonamine, T. Tomioka, A. Aoza, H. Bito, K. Fujii, T. Higashi, K. Hiramatsu, K. Ikematsu, A. Ishikawa, Y. Kato, H. Kuroiwa, T. Matsuda, O. Nitoh, H. Ohta, K. Sakai, R.D. Settles, A. Sugiyama, H. Tsuji, T. Watanabe, H. Yamaoka, and T. Yazu. Cosmic ray tests of a GEM-based TPC prototype operated in Ar–CF4–isobutane gas mixtures. *Nuclear Instruments and Methods in Physics Research Section A: Accelerators, Spectrometers, Detectors and Associated Equipment*, 641(1):37–47, 2011. `https://www.sciencedirect.com/science/article/pii/S016890021100355X`.

[35] LCTPC home page. `https://www.lctpc.org/e8/e46/e47/`.

[36] S.F. Biagi. Monte carlo simulation of electron drift and diffusion in counting gases under the influence of electric and magnetic fields. *Nuclear Instruments and Methods in Physics Research Section A: Accelerators, Spectrometers, Detectors and Associated Equipment*, 421(1):234–240, 1999. `https://www.sciencedirect.com/science/article/pii/S016890029801233`.

[37] M. Kobayashi, T. Ogawa, A. Shoji, Y. Aoki, K. Ikematsu, P. Gros, T. Kawaguchi, D. Arai, M. Iwamura, K. Katsuki, A. Koto, M. Yoshikai, K. Fujii, T. Fusayasu, Y. Kato, S. Kawada, T. Matsuda, S. Narita, K. Negishi, H. Qi, R.D. Settles, A. Sugiyama, T. Takahashi, J. Tian, T. Watanabe, and R. Yonamine. Measurement of the electron transmission rate of the gating foil for the TPC of the ILC experiment. *Nuclear Instruments and Methods in Physics Research Section A: Accelerators, Spectrometers, Detectors and Associated Equipment*, 918:41–53, 2019. `https://www.sciencedirect.com/science/article/pii/S016890021831636X`.

[38] DESY II Description & Status. `https://particle-physics.desy.de/e252106/e252106/e252334`.

[39] DESY HP. `https://particle-physics.desy.de/test_beams_at_desy/e252106/e252211`.

[40] V. Hedberg, Björn Lundberg, and Anders Nils Erik Oskarsson. Development of the Readout System for a TPC at the Future Linear Collider. 2012. https://www.hep.lu.se/eudet/documents/LC-DET-2012-080.pdf.

[41] OGAWA Tomohisa. Private Communication.

[42] Jason Abernathy, Klaus Dehmelt, Ralf Diener, Jan Engels, Jim Hunt, Martin Killenberg, Thorsten Krautscheid, Astrid Munnich, Simone Zimmermann, Martin Ummenhofer, Adrian Vogel, and Peter Wienemann. MarlinTPC: A common software framework for TPC development. In *2008 IEEE Nuclear Science Symposium Conference Record*, pages 1704–1708, 2008. https://ieeexplore.ieee.org/abstract/document/4774731.

[43] KalTest: A ROOT-based Kalman Filter Package. https://www-jlc.kek.jp/subg/offl/kaltest/.

[44] Garfield++ homepage. https://garfieldpp.web.cern.ch/garfieldpp/.

[45] SHOJI Aiko. Private Communication.

[46] Astrid Münnich. Simulation studies for a high resolution time projection chamber at the International Linear Collider. *INSTRUMENTATION RELATED TO NUCLEAR SCIENCE AND TECHNOLOGY*, 38(1), 2007. https://inis.iaea.org/search/search.aspx?orig_q=RN:38099816.